COLLECTIVE CLUSTERIZATION IN GROUND AND EXCITED STATES OF NUCLEAR SYSTEMS AT LOW ENERGIES

A THESIS

submitted to the

FACULTY OF SCIENCE

THAPAR UNIVERSITY, PATIALA

for the degree of

DOCTOR OF PHILOSOPHY

by

GUDVEEN SAWHNEY

SCHOOL OF PHYSICS AND MATERIALS SCIENCE

THAPAR UNIVERSITY

PATIALA-147004, PUNJAB

INDIA

"The web of our life is of a Mingled Yarn, good and ill together. Our virtues would be proud if our faults whipped them not, and our crimes would despair if they were not cherished by our virtues"- William Shakespeare

All's well that ends well.

Dedicated to

My Beloved Parents

CANDIDATE'S DECLARATION

I hereby certify that the work which is being presented in this thesis entitled "**COLLECTIVE CLUSTERIZATION IN GROUND AND EXCITED STATES OF NUCLEAR SYSTEMS AT LOW ENERGIES**" in partial fulfillment of the requirements for the award of Degree of Doctor of Philosophy and submitted in the School of Physics annd Materials Science, Thapar University, Patiala, is an authentic record of the my own work carried out during a period from January 2010 to August 2012 under the supervision of **Dr. Manoj K. Sharma**, Associate Professor, Thapar University Patiala.

The matter presented in this thesis has not been submitted by me for the award of any other degree of this or any other university/institute.

Gudveen

(GUDVEEN SAWHNEY)

This is to certify that the above statement made by the candidate is correct to the best of our knowledge.

MSharma

Dr. Manoj K. Sharma

Signature of HOD

Signature of Dean R&SP

Signature of Examiner

Date: 03.11.2012

Acknowledgements

It is the almighty who bestowed me power, courage and will to meet the ups and downs of life. I courteously bow before him.

I have no words to express my deep sense of gratitude and obligation to my esteemed supervisor, Dr. Manoj K. Sharma, Associate Professor, School of Physics and Materials Science, Thapar University, Patiala for his illuminating guidance, keen interest, sympathetic attitude and persistent encouragement. It is matter of pride and pleasure to have worked under his generous and able supervision. I thank him for his patience and encouragement that carried me on through difficult times, and for his insights and suggestions that helped to shape my research skills. Thanks Sir, for believing in me and standing by me over the years. A special word of thanks to Madam Sharma for her motherly affection and care.

I gratefully appreciated the support of Dr. Raj K. Gupta, Professor of Physics (Retd.), Physics Department, Panjab University, Chandigarh who provided me the great opportunity to work with him. His sincere attitude and great knowledge in physics makes him an excellent teacher. I am thankful for his enthusiasm and willingness to share his knowledge. It is a fortunate for me being associated with him in research field.

I wish to express humble and sincere gratitude to Dr. Kulvir Singh, Head, School of Physics and Materials Science, Thapar University, Patiala, for providing me the necessary facilities in the department. I am very much thankful to him for his affectionate behavior throughout the period of my research. My sincere thanks also goes to all the staff of the School for their help and kind support. I am thankful to Prof. K. K. Raina, Deputy Director, for his encouragement and constant moral support to

accomplish this task. My advisory doctoral committee members Dr. Rajesh Kumar Gupta and Dr. Suneel Kumar deserve many thanks for their useful suggestions during my progress report presentations. Thanks also goes to Dr. P. K. Bajpai, Dean of Research and Sponsored Projects for providing the possible research facilities here at Thapar University Campus. Special thanks to Prof. O. P. Pandey for providing me useful and valuable tips for research and fellowship as a teaching associate well in time.

I deeply appreciate Dr. Birbikram Singh and Dr. Shefali Kanwar for their gentle guidance, perceptive suggestions, and inspiration which have provided good and smooth basis for my Ph.D. tenure. I am also thankful to Dr. Raj Kumar, Mrs. Manie Jain, Dr. Sanjeev Kumar, and Dr. Varinderjit Kaur for their encouraging help and constant support.

I am happy to acknowledge the help and co-operation given to me by my lab mates Manpreet, Deepika, Gurvinder, Kirandeep, Rajni, Mandeep and many other research scholars here at School of Physics and Materials Science. I am grateful to all my friends who supported and inspired me during the awful phases of my life and shared joy and happiness during the good times. Sincere thanks to all my friends especially Manveen, Supreet, Lavanya, Sandeep, Kanwal and others for their help, moral support and jovial company. Thanks for the friendship and memories.

Lastly, the most important, I feel an immense admiration and humble obligation for my family, my constant source of happiness. Words that I know are rather insufficient to convey my sincerest regard to my parents (Mr. Inderjit Singh and Mrs. Jagjit Kaur) whose moral encouragement, countless blessing, everlasting desire and untiring struggle brought me here upto. God is generous enough to bless me with

unforgettable persons like my sister Rashveen and brother Sarpreet for their endless love, best wishes and moral support to achieve this goal successfully. A special thanks goes to my nephew Arav, whose smiling face have always made me refreshing.

The financial assistance in the form of fellowships from Thapar University, Patiala and then from University Grants Commission (UGC), New Delhi, under the "Maulana Azad National Fellowship For Minority Students Scheme" is gratefully acknowledged.

Patiala

August, 2012.

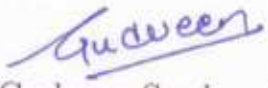

(Gudveen Sawhney)

List of Publications

I. International Journals:

1. Entrance channel independence in the decay of $^{215}Fr^{*}$ nucleus,
   Manoj K. Sharma, **Gudveen Sawhney**, Shefali Kanwar and Raj K. Gupta, Mod. Phys. Lett. A **25**, 2022 (2010).

2. Fusion excitation functions of $^{64}Ni+^{112-132}Sn$ reactions studied on the dynamical cluster-decay model,
   Manoj K. Sharma, Shefali Kanwar, **Gudveen Sawhney**, Raj K. Gupta and W. Greiner, J. Phys. G: Nucl. Part. Phys. **38**, 055104 (2011).

3. The decay of the compound nucleus $^{215}Fr^{*}$, formed in the $^{11}B+^{204}Pb$ and $^{18}O+^{197}Au$ reaction channels using the dynamical cluster-decay model,
   Manoj K. Sharma, **Gudveen Sawhney**, Raj K. Gupta and W. Greiner, J. Phys. G: Nucl. Part. Phys. **38**, 105101 (2011).

4. Role of higher-multipole deformations in exotic ^{14}C cluster radioactivity,
   Gudveen Sawhney, Manoj K. Sharma and Raj K. Gupta, Phys. Rev. C **83**, 064610 (2011).

5. Dynamical decay process of $^{219,220}Ra^*$ formed in $^{10,11}B$+^{209}Bi reactions,

   Gudveen Sawhney and Manoj K. Sharma, Eur. Phys. J. A **48**, 57 (2012).

6. Decay of the $^{213,217}Fr^*$ systems formed in ^{19}F+$^{194,198}Pt$ reactions at $E_{c.m.}$= 80 - 94 MeV,

   Manoj K. Sharma, Shefali Kanwar, **Gudveen Sawhney** and Raj K. Gupta, Phys. Rev. C **85**, 064602 (2012).

7. Decay of $^{241}Pu^*$ formed in ^{9}Be+^{232}Th around Coulomb barrier using static and dynamic deformations,

   Gudveen Sawhney, Raj Kumar and Manoj K. Sharma, Phys. Rev. C **86**, 034613 (2012).

8. Sticking versus non-sticking moment of inertia: Application to the ^{9}Be+^{232}Th reaction,

   Gudveen Sawhney, Raj Kumar and Manoj K. Sharma, AIP Conf. Proc., (2012) submitted.

II. In Conferences, Symposiums and Workshops: (a) International:

1. Decay of $^{213,217}Fr^*$ formed in ^{19}F + $^{194,198}Pt$ reactions using dynamical cluster-decay model, Manoj K. Sharma, Shefali Kanwar, **Gudveen Sawhney** and Raj K. Gupta, DAE-BRNS Symp. on Nucl. Phys., **54**, 370, Dec 8-12, 2009, BARC, Mumbai, India.

2. Decay of $^{219,220}Ra$ formed in boron induced reactions, **Gudveen Sawhney** and Manoj K. Sharma, IX Latin American Symposium on Nuclear Physics

and Applications, July 18-22, 2011, Quito, Ecuador.

3. Role of deformations in fusion-fission of $^{241}Pu^*$ nucleus, **Gudveen Sawhney**, Raj Kumar and Manoj K. Sharma, 11^{th} International Conference on Nucleus-Nucleus Collisions (NN2012), May 27-June 1, 2012, San Antonio, Texas.

4. Dynamical cluster-decay effects in $^{213,215,217}Fr^*$ compound systems, **Gudveen Sawhney**, Manoj K. Sharma and Raj K. Gupta, 10^{th} International Conference on Clustering Aspects of Nuclear Structure and Dynamics, September 24-28, 2012, Debrecen, Hungary.

(b) National:

1. Decay of $^{215}Fr^*$ compound nucleus formed in ^{11}B + ^{204}Pb and ^{18}O + ^{197}Au reaction, **Gudveen Sawhney**, Manoj K. Sharma and Raj K Gupta, INS National Seminar on "Nuclear Technology for Sustainable Development (NTSD-09)" **17**, 115, October 10-11, 2009, Thapar University, Patiala, India.

2. Role of higher multipole deformations and compact orientations in the decay of $^{217}Fr^*$ nucleus , **Gudveen Sawhney** and Manoj K. Sharma, DAE-BRNS Symp. on Nucl. Phys., **55**, 170, Dec 20-24, 2010, BITS, Pilani, Rajasthan, India.

3. Fusion-fission of $^{215}Fr^*$ nucleus using the Dynamical Cluster-decay Model, **Gudveen Sawhney**, Manoj K. Sharma and Raj K Gupta, DAE-BRNS Symp. on Nucl. Phys., **55**, 386, Dec 20-24, 2010, BITS, Pilani, Rajasthan, India.

4. Alpha decay branching ratios to the ground state rotational bands of daughter nuclei, **Gudveen Sawhney**, Gurvarinder and Manoj K. Sharma, 14^{th} Punjab

Science Congress, Feb 7-9, 2011, Pg- 125, SLIET, Longowal, India.

5. ^{14}C cluster radioactivity using Preformed Cluster Model, **Gudveen Sawhney** and Manoj K. Sharma, National Symposium on Radiation Physics and Nanomaterials (NSRPN-11), Feb 4-5, 2011, Punjabi University, Patiala, India.

6. Decay of ^{196}Pt nuclear system formed in radioactive ^{132}Sn induced reaction, Manoj K. Sharma and **Gudveen Sawhney**, National Symposium on Radiation Physics and Nanomaterials (NSRPN-11), Feb 4-5, 2011, Punjabi University, Patiala, India.

7. Decay of $^{241}Pu^*$ formed in the collision of loosely bound ^{9}Be with radioactive target ^{232}Th, **Gudveen Sawhney**, Raj Kumar and Manoj K. Sharma, 2^{nd} National Conference on Advanced Materials and Radiation Physics (AMRP-2011), November 4-5, 2011, Pg-79, SLIET, Longowal, India.

8. Fusion-fission of $^{219,220}Ra^*$ using the Dynamical Cluster-decay Model, **Gudveen Sawhney** and Manoj K. Sharma, DAE-BRNS Symp. on Nucl. Phys., **56**, 524, Dec 26-30, 2011, Andhra University, Visakhapatnam, India.

9. Halo structure of light nuclei at the neuron drip line, **Gudveen Sawhney**, Silky Singla and Manoj K. Sharma, DAE-BRNS Symp. on Nucl. Phys., **56**, 526, Dec 26-30, 2011, Andhra University, Visakhapatnam, India.

10. Decay of $^{241}Pu^*$ formed in $^{9}Be + ^{232}Th$ reaction around the Coulomb barrier, **Gudveen Sawhney** and Manoj K. Sharma, DAE-BRNS Symp. on Nucl. Phys., **56**, 600, Dec 26-30, 2011, Andhra University, Visakhapatnam, India.

11. Decay possibilities of $^{241}Pu^{*}$ nuclear system formed via collision of ^{9}Be with ^{232}Th target, **Gudveen Sawhney** and Manoj K. Sharma, 23^{rd} Annual General Meeting, Materials Research Society of India (MRSI), Feb 13-15, 2012 Pg-124, Thapar University, Patiala, India.

12. Effect of static and dynamic deformations in the decay of $^{241}Pu^{*}$ nucleus, **Gudveen Sawhney**, Raj Kumar and Manoj K. Sharma, DAE-BRNS Symp. on Nucl. Phys., Accepted, Dec 3-7, 2012, University of Delhi, New Delhi, India.

13. Collective clusterization in ground and excited states of nuclear systems at low energies, **Gudveen Sawhney**, DAE-BRNS Symp. on Nucl. Phys., Accepted, Dec 3-7, 2012, University of Delhi, New Delhi, India.

Contents

List of Figures

List of Tables

Abstract

The aim of the present work is to carry out a comprehensive theoretical study of the decay paths of nuclear systems formed in heavy ion reactions alongwith the decay of ground state trans-lead nuclei exhibiting the phenomenon of cluster radioactivity. The reaction dynamics of hot and rotating, heavy compound systems is studied within the framework of Dynamical Cluster-decay Model (DCM) which is based on collective clusterization approach. The deformation and orientation effects of the reaction partners and decay products are explicitly included along with temperature and angular momentum contribution in this model. The ground state cluster decay of radioactive nuclei have been undertaken within the Preformed Cluster-decay Model (PCM), again having deformation and orientation effects of daughter and cluster nuclei included in it. The thesis is organized into the following seven chapters.

Chapter 1 gives a brief account of available experimental and theoretical attempts made to understand the reaction dynamics of hot and rotating nuclei, and the phenomenon of cluster radioactivity. An extensive study of formation and decay of compound nucleus (CN) and noncompound nucleus (nCN) processes is described. Beside this, the role of deformations and orientations of nuclei, entrance channel ef-

fects, barrier modification, and fission fragment anisotropies in the fusion-fission process have been discussed.

Chapter 2 gives relevant details of the Preformed Cluster-decay Model (PCM) and the Dynamical Cluster-decay Model (DCM). PCM is applied to study the spontaneous cluster radioactivity process and DCM is applied to investigate the decay of hot and rotating compound nucleus (CN) formed in heavy ion reactions. It is important to note here that DCM is an extension of PCM which finds its basis in Quantum mechanical fragmentation theory (QMFT). Within this formulism, the fragmentation potential is calculated as sum of temperature dependent binding energies, Coulomb interaction, proximity potential and rotational energy. The deformation and orientation effects are duly incorporated in PCM as well as in DCM. The DCM treats the CN decay of light particles LPs, intermediate mass fragments IMFs, heavy mass fragments HMFs and the asymmetric or near-symmetric fission AF, and symmetric fission SF on equal footings, in contrast to statistical models which follow different formalisms for different processes.

In **Chapter 3**, the entrance channel effects in the decay of ^{215}Fr* nucleus, formed in ^{11}B+^{204}Pb and ^{18}O+^{197}Au reactions, is studied by using the dynamical cluster-decay model (DCM). The observed decay is mainly via fusion-fission, with data collected for both the fission excitation functions and fission fragment anisotropies. In agreement with experimental data and conclusions based on statistical code PACE2, for fission excitation functions, DCM calculations also show no contribution of the quasi-fission component in fission cross-sections for both the reaction channels, mea-

sured at incident center-of-mass energy spread on either side of the Coulomb barrier. Also, the fission fragment anisotropies, calculated on DCM for the first time, are found consistent with experimental data for both the reaction channels, confirming the entrance channel independence in the decay of ^{215}Fr*.

In addition to this, the decay paths of other Fr-isotopes namely, ^{213}Fr* (with neutron number $N = 126$) and ^{217}Fr* (with $N = 130$), formed in ^{19}F + ^{194,198}Pt reactions, are studied as collective clusterization process, for emissions of both the light particles (LPs) and fission fragments, within the DCM. The role of magic $N = 126$ shell of the compound nucleus (CN) or the presence of a noncompound nucleus (nCN) component, like the quasi-fission (qf), in fission cross-sections are investigated. A small hump or shoulder is seen in fragment preformation yields for the deformed case (β_2 or β_2-β_4) in both the systems due to a deformed closed shell around $Z_2 = 36$ and spherical magic shell around $Z_1 = 50$, which for ^{213}Fr* ($N = 126$) decay is somewhat more pronounced as compared to ^{217}Fr* ($N = 130$).

In **Chapter 4**, the excitation functions for both the evaporation residue and fission have been calculated for ^{10}B + ^{209}Bi and ^{11}B + ^{209}Bi reactions forming compound systems ^{219,220}Ra*, using the dynamical cluster-decay model (DCM) with effects of deformations and orientations of nuclei included in it. In addition to this, the excitation functions for complete fusion (CF) are obtained by summing the fission cross-sections, neutron evaporation and charged particle evaporation residue cross-sections produced through the αxn and pxn ($x = 2, 3, 4$) emission channels for the ^{219}Ra system at various incident centre-of-mass energies. Experimentally the CF cross-sections are suppressed and the observed suppression is attributed to the

low binding energy of ^{10,11}B which breaks up into charged fragments. The reported complete fusion (CF) and incomplete fusion (ICF) excitation functions for the ^{219}Ra system are found to be nicely fitted by the calculations performed in the framework of DCM, without invoking significant contribution from quasi-fission. Although DCM has been applied for a number of compound nucleus decay studies in recent past, the same is tested here in reference to ICF and subsequent decay processes along with the CF process.

In **Chapter 5**, the decay of hot and rotating compound nucleus ^{241}Pu* formed in the reaction ^{9}Be + ^{232}Th around the Coulomb barrier ($\approx$ 42.16 MeV), at energies ranging from 37 - 48 MeV, is studied using the dynamical cluster-decay model (DCM) with effects of static and dynamic deformations included. With the inclusion of dynamical deformations both the preformation probability P_0 and the tunneling probability P, and hence the cross-sections, change considerably. The only parameter of the model, namely the neck length parameter, varies smoothly with excitation energy or temperature of the system both at above-and below-barrier energies, whose value depends strongly on the limiting angular momentum, which in turn depends on the use of sticking and non-sticking moment of inertia. The relative effect of static and dynamic deformations on neck length parameter ΔR is also studied, which indicate the reaction time scale for both static and dynamic choices of deformation. Beside this the exclusive role of angular momentum and "barrier modification" effects at sub-barrier energies are also addressed.

In **Chapter 6**, we have studied nine cases of spontaneous emission of ^{14}C clusters

in the ground-state decays of the same number of parent nuclei from the trans-lead region, specifically from ^{221}Fr to ^{226}Th, using the Preformed Cluster Model (PCM) of Gupta and collaborators, with choices of spherical, quadrupole deformation (β_2) alone, and higher multipole deformations (β_2, β_3, β_4) with cold "compact" orientations θ^c of decay products. The calculated ^{14}C cluster decay half-life times are found to be in nice agreement with experimental data only for the case of higher-multipole deformations (β_2-β_4) and θ^c orientations of cold elongated configurations. In other words, compared to an earlier study of clusters heavier than ^{14}C, where the inclusion of β_2 alone, with "optimum" orientations, was found to be enough to give the best comparison with data, here for ^{14}C cluster decay the inclusion of higher-multipole deformations (up to hexadecapole), together with θ^c orientations, is found essential on the basis of PCM. Interestingly, whereas both the penetration probability and assault frequency work simply as scaling factors, the preformation probability is strongly influenced by the order of multipole deformations, and orientations of nuclei. The possible role of Q value and angular-momentum effects are also considered in reference to ^{14}C cluster radioactivity.

Finally, in **chapter 7**, conclusions are summarized and an outlook of our work is presented.

Chapter 1

Introduction

The beginning of the 21st century is an ideal time for scientific developments as large amount of experimental and theoretical facilities have been made available in recent times. The various ideas, measurements, theories and observations are merged into what appears to be a unified picture of the nature around us, universe we live in and even our own existence. Although light nuclei were created within a few minutes after the Big Bang, heavier nuclei were produced, and are still being made in laboratories and from nucleosynthesis in stars. In order to understand the fundamentals related to origin of the physical world in which we live, it is necessary for us to understand the properties of nuclei. Nuclei are composed of protons and neutrons, and depending upon stability they come in a variety of combinations of protons and neutrons. The atomic nucleus was discovered almost a hundred years ago by Geiger and Marsden (1909) when they irradiated gold and silver foils by alpha-particles from a radioactive source and observed many back scattered alpha-particles which led Rutherford (1911) to postulate that the atomic nucleus is a very small and dense matter located in the centre of an atom. This discovery paved the

way, for Bohrs model of hydrogen atom (1913) and further on to the development of quantum mechanics and related aspects. These developments as a whole have led to the emergence of nuclear physics which deals with the properties of atomic nuclei, the interactions between them and their constituents. The first application of quantum mechanics to nuclear physics came into picture when Gamow in 1928 discovered quantum mechanical tunneling as a phenomenon associated with the concept of α-decay, which could be used further to understand the nuclear reaction dynamics and related aspects of nuclear physics.

The basic nuclear properties are of utmost importance to understand the interactions which bind the protons and neutrons together in nucleus which further allow us to derive directly or indirectly, information on the nuclear structure, as well as on the strong nuclear forces. The light projectiles, such as electrons, protons, neutrons and α-particles were used for the study of nuclear properties in the beginning. Later on, with the advent of modern accelerators, which are capable of imparting high energies to heavier projectiles, it has been possible to study the new branch of nuclear physics, called "Heavy Ion Physics". The recent progress in heavy ion reactions can be attributed to the development of ion-separation facilities and accelerator technologies currently available in different laboratories of the world, which can accelerate a variety of heavy ions to energies from a few MeV to several TeV range.

The study of heavy ion collisions played an instrumental role in providing the ion-ion interaction potential which is one of the most important ingredient in the investigation of structure, stability or decay of nuclei, elastic or inelastic scattering, the estimation of cross-sections for the synthesis of heavy elements, phenomena of

multiple fragmentation, and nuclear flow etc. This information is important for the understanding of various exotic issues like the evolution of universe, working of stars, the abundance of elements etc., along with nuclear phenomena. The basic features of heavy ion reactions can be understood in terms of an interaction potential between the centers of the mass of two colliding nuclei consisting of long range of Coulomb repulsion and a short range of nuclear attraction. Although the Coulomb interaction plays an important role but is not enough to describe the formation of a stable system, as a result the existence of the nucleus is an indication of the presence of strong interaction nuclear force which binds protons and neutrons together. The strong interaction has a very short range, of about 2 fm. This puts a severe obstacle to its experimental investigation, when compared to the other fundamental forces. Alternatively, the properties of nuclei are better described by employing models. The downside of this approach is that different models are necessary to account for the various features of nuclei. These features include nuclear size, shape, binding energy, and decay properties of nuclei etc. Beside this, the precise shell structure within the nucleus and their associated excitation spectra are of immense importance for overall understanding of a nuclear system.

The nuclear shell-model given by Mayor and Jensen in 1949 describes beautifully the magic numbers along with the explanation of many nuclear properties such as spin, magnetic moment, and nuclear spectra. While the shell-model treats each nucleon as an independent particle, and explained reaction data very nicely, collective models achieved great success in describing other aspects of nuclear structure. These aspects include many properties of nuclei, such as large electric quadrupole moments, deviations from the spherical shape, and rotational and vibrational spec-

tra, which cannot be explained by nuclear shell-model. Various other nuclear models have been proposed, enriching our knowledge of nuclei and paved the way in the development of nuclear physics.

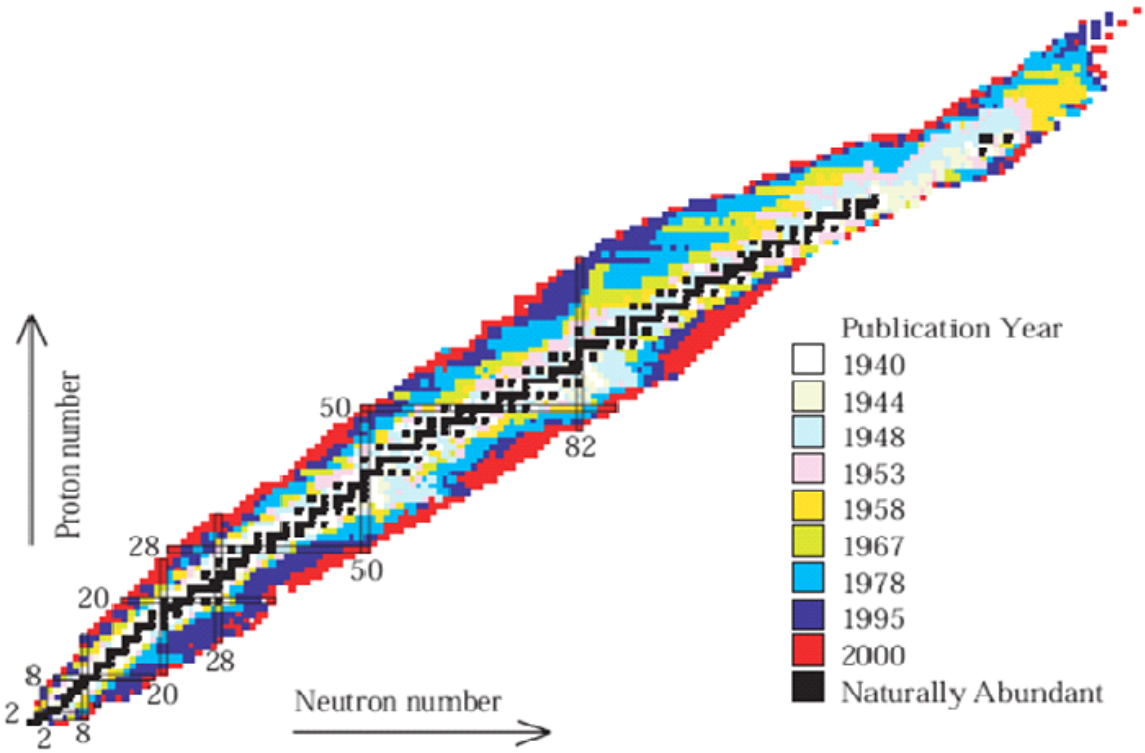

Figure 1.1 Historic nuclear chart with color indications of year of discovery.

The study of nuclear physics gives an unique opportunity to look for the nature of interactions that plays a vital role not only in the nuclear physics, but also in other branches of physics, such as astrophysics and cosmology. There are many potential applications of nuclear physics, in medicine (magnetic resonance imaging, MRI), radiocarbon dating (archaeology), materials engineering (ion implantation), to name a few. The historical development of nuclear chart is depicted in Fig. 1.1 where the development from about 800 isotopes in the 1940s to about 3000 isotopes today is visualized. It is relevant to mention here that knowledge on nuclear physics

extracted in the 1950s, 60s and 70s was mostly based on about 300 stable nuclei (compared to about 6000 nuclei), due to the limited ability to produce unstable nuclei. About one third of all known isotopes has been discovered in the last 20 years and the basis for extending nuclear phenomenon to unstable nuclei has been greatly improved. Many of these are still unknown and efforts are on to synthesize some of them in the near future using the radioactive ion beam facilities.

The tough challenges in nuclear perspective can be met only by developing and establishing clear understanding of nuclear properties and related aspects. The availability of experimental techniques coupled with advanced theoretical developments have enabled us to study the nuclear behavior in new perspective. The nuclear reaction dynamics is usually classified into three groups on the basis of energy of incident projectile as low energy (E $\leq$ 15 MeV/nucleon), intermediate energy (15 $<$ E $<$ 500 MeV/nucleon) and high energy (E $\geq$ 500 MeV/nucleon). The present work is confined to low energy nuclear reactions, where we intend to explore the decay process of a variety of nuclei via a collective clusterization process. In a collective clusterization approach, the concept of relative pre-formation probability P_0 is used, which means that the preformation factor depends not only on the decay products but also on all other possible fragmentations of a decaying nucleus. Thus, in addition to the penetrability P through a barrier, there is a relative preformation factor P_0 associated with each decay product. Here, in this work, all possible decay paths, i.e., the evaporation residue ER consisting of multiple light particles (LPs: n, p, α) and γ rays, complex intermediate mass fragments IMFs (with masses 5$\leq$A$\leq$20 and charges 2$\leq$Z$\leq$10), and the asymmetric or near-symmetric fission nSF, and symmetric fission fragments SF, are all treated on equal footings as dynamical

collective mass motions of preformed fragments or clusters through the barrier.

A comprehensive study of various types of emission from the ground state of parent nuclei as well as excited state of compound nucleus (CN) formed in low energy reaction is highly desirable, as it gives information about the nuclear structure, besides the underlying nuclear forces. At low energies, an average nuclear force field acts between the decay fragments which in turns ensure possibility of more than one decay path. This average nuclear force field is largely influenced by entrance channel, angular momentum and the temperature considerations together with the contribution of deformation and orientation effects. In the following, spontaneous (ground-state) decay in reference to cluster radioactivity is discussed in Sec. 1.1 and the decay of excited state nuclei formed in heavy ion reactions is elaborated in Sec. 1.2.

1.1 Ground state cluster radioactivity

The discovery of radioactivity by H. Becquerel in 1896 and subsequently studied by Pierre and Marie Curie, E. Rutherford, and many others, have played leading roles in the understanding of nuclear phenomena and related properties. Near a century after its discovery, the prediction of cluster radioactivity was reported experimentally by Rose and Jones [1] in 1984 by the observation of spontaneous emission of ^{14}C from ^{223}Ra nucleus. Since then, a number of investigations have been reported by different experimental groups around the world, confirming the first experiment and adding some heavier decay modes like ^{20}O from ^{228}Th, ^{24,26}Ne from ^{232}U and ^{234}U, ^{23}F from ^{231}Pa, ^{28,30}Mg from ^{238}Pu and ^{32,34}Si from ^{238}Pu and ^{241}Am (for a review

see Refs. [2, 3]).

On the theoretical side, the first successful description of cluster decay was made by Săndulescu *et al.* [4] four years before its experimental discovery. The phenomenon of cluster radioactivity is different from that of fission. In fission, a nucleus deforms continuously while passing over the Coulomb barrier and breaks into two comparable fragments as it reaches the saddle point configuration, whereas in cluster-radioactivity, the unstable parent nucleus decays into a cluster, which is heavier than alpha particle but smaller than the lightest of fission fragments, and the daughter nucleus. Note that in fission two fragments (light and heavy) are measured simultaneously, in contrast to the exotic cluster-decay process where only light fragment half-lives are measured.

Cluster decay is a quantum tunneling process, in which the cluster has to penetrate the potential barrier in order to come out from the parent nucleus. Several theoretical approaches have been advanced extensively to describe this process. Differing in details, two kinds of models are used generally: (i) the Unified Fission Models (UFM), such as the Analytic Super-Asymmetric Fission Model (ASAFM) of Săndulescu, Poenaru, and Greiner [4], where cluster formation probability is calculated as an internal barrier penetration, and (ii) Preformed Cluster Models (PCM), of Gupta and collaborators [5, 6], in which the cluster preformation is calculated by solving the Schrödinger equation for the dynamic flow of charges and masses.

Both these models are based on Gamow's theory of barrier penetration. Whereas Gamow theory for α-decay uses the square well potential, the UFM and PCM, advanced for the processes of cluster radioactivity as well as α-decay, use the more realistic nuclear interaction potentials. Thus, an appropriate knowledge of the po-

tential barrier is extremely important and essential for overall understanding of this phenomenon, which in turn plays a vital role in calculating the half-lives of the emitted clusters. Besides these two model approaches (the UFM and PCM), semiempirical formulas have also been proposed by different authors [7, 8] for calculating the half-life times of exotic cluster decays.

There are twenty known nuclides from ^{221}Fr to ^{242}Cm emitting light nuclei/clusters ranging from ^{14}C to ^{34}Si, and the search for other possible cluster decays is still on. It is a cold process (zero excitation energy) since the energy released as Q-value is completely consumed by the kinetic energy alone of the two fragments (the cluster and daughter nuclei). The half-lives associated with this process are very long, and vary in a wide range from 10^{11} to 10^{26} sec. Branching ratios to the dominant α-decay in these nuclei are very small and are comprised between 10^{-9} to 10^{-16}. A small value of half-life for a parent nucleus indicates the presence of spherical or deformed shell closure in the daughter nucleus whereas high value on the other hand implies the same for the parent nucleus against the decay.

Interestingly all the decaying parent nuclei belong to translead region while the daughter nuclei are almost closed shell spherical nuclei (^{208}Pb or its neighboring nuclei). This fact allows us to better characterize cluster radioactivity and indicates strong influence of shell effects in selecting possible cluster emissions. It is relevant to mention here that deformations and orientations of nuclei, in addition to shell effects, play very significant role in cluster decays of radioactive nuclei [9, 10]. The influence of cluster deformation effects have been considered in the past [11] using the double folded Michigan-3 Yukawa (M3Y) potential for emitted quadrupole deformed cluster, treating the daughter as spherical. Later on, higher multipole deformations

were also accounted with in the M3Y potential [12].

In the present work, the Preformed Cluster-decay Model (PCM) [5, 6] is used for the first time to study the role of higher-multipole deformations (up to hexadecapole) with cold compact orientations of nuclei, in exotic ^{14}C cluster radioactivity [13]. PCM is based on well known Quantum mechanical fragmentation theory (QMFT) [14,15]. Here the process of binary decay is treated in two steps: First step is the quantum mechanical preformation probability of the cluster in the mother nucleus and the second step is the penetration of the cluster through the interaction barrier. It is important to note that, in terms of the barrier picture, a cluster-decay process is in fact a fission process with structure effects of the CN also included via the preformation of the fragments, but without any phase space arguments (i.e. with no level density calculations). Till now, we were talking about ground state decays and in particular the concept of cluster radioactivity. In the following, a brief account about the dynamical features of decay product of low energy nuclear reactions formed in heavy ion collisions is described.

1.2 Low energy heavy ion reactions

Nuclear reactions induced by heavy ions provide an opportunity to explore the nucleus-nucleus potential and thus have become the principal tool in nuclear physics research. In low energy heavy ion collisions, when two stable nuclei are brought together at energies above the Coulomb barrier, one of the main processes can be fusion, in which all the angular momentum of the initial system is retained. In order to bring the two nuclei sufficiently close to each other, i.e., to overcome their mutual

electrostatic Coulomb repulsion and subsequently to bring them into the range of attractive nuclear force, sufficient kinetic energy is required in the entrance channel (equivalently, the incident center-of-mass energy) to form the excited compound nucleus. Thus the simplest picture of fusion is that of quantum tunneling through a one dimensional barrier formed by the long range Coulomb potential, the centrifugal potential and the short range nuclear potential.

The idea of compound nucleus formation was first suggested by Niels Bohr in 1936. A theory was proposed to explain nuclear reaction as a two-stage process comprising the formation of a relatively long-lived compound nucleus and its subsequent decay. This compound-nucleus model has been very successful in explaining the nuclear reactions induced by relatively low energy bombarding particles. The bombarding particle looses all of its energy to the target nucleus and becomes an integral part of a new, highly excited, rotating, unstable nucleus, called the compound nucleus (CN). Once formed, the excitation energy of the CN is transferred not only to the relative motion of the fragments, but also to their intrinsic degrees of freedom and angular momentum. The CN, in general, looses its excitation energy either by loosing a couple of neutrons and go to ground state, or it decays by emitting multiple light particles (LPs) such as n, p, α and γ-rays and undergoes fission (called, fusion-fission) or alternatively the fusion-cluster decay. For heavy nuclear systems $A_{CN} \approx 200$, the fission mode dominate, however there is a competition between fission and fusion evaporation residue decay modes in case of the light compound systems. Interestingly a significant contribution of ER is measured in a few heavy systems as well [16].

If, for some reason, the energy is redistributed among several nucleons only,

without involving rest of the nucleus, the reaction occurs without formation of a compound nucleus and this process is called noncompound nucleus (nCN). The measurement of fission fragments and evaporation residues in general provide a comprehensive picture of the processes subsequent to collision between projectile and target nucleus. However depending on beam energy and entrance channel mass asymmetry, a sizeable amount of nCN components like Deep-Inelastic Collision (DIC), Quasi-Fission (QF), Incomplete Fusion (ICF) etc., start competing in addition to fully equilibrated compound nucleus states.

In DIC, the projectile and the target nuclei stick together for a sufficiently long time, dissipating considerable amount of energy, while the surfaces of the colliding nuclei overlap for a brief period corresponding to a partial rotation of the intermediate dinuclear complex. The DIC product masses are close to the projectile and target mass. The time-scale of deep inelastic collisions is long enough for the exchange of significant number of nucleons between the target and projectile but shorter than the compound nucleus life-time. Generally, for systems having large Coulomb repulsion in the entrance channel (symmetric target projectile combinations), DIC has been reported to be the dominant nCN channel [17, 18].

The term quasi-fission (QF) refers to a process where incoming nuclei in a reaction do not loose their identity and as a result, non-equilibrated CN decay into projectile and target like fragments. It has been observed that when two interacting nuclei touch each other by their lateral surfaces (near-side collisions) a high formation probability of a spherical CN is expected, whereas, a high QF probability is expected in the elongated configuration when nuclei touch each other by their poles (near-tip collisions) [19, 20]. In terms of reaction time scales, QF lies between DIC,

where the mass asymmetry of the entrance channel is mostly preserved, and CN process, where all memory of the entrance channel is lost.

Another mechanism that contributes nCN process is the incomplete fusion (ICF) which involves the break-up of projectile nucleus near the surface of the target nucleus into two fragments, one of which escapes with relatively unchanged velocity, while the other fuses with the target to form an excited intermediate system, which subsequently de-excites, in the usual way, by particle evaporation [21, 22]. The complete fusion (CF) occurs, when entire projectile fuses with the target nucleus to form a fully equilibrated compound nucleus. The linear momentum is completely transferred to the target nucleus in case of CF, while partial transfer of projectile momentum takes place for the case of ICF reactions. It is well established that ICF is the dominant nCN channel for systems with higher entrance channel mass asymmetry [23, 24]. There is exchange of nucleons between the colliding reaction partners in DIC, whereas ICF reactions involve the transfer of nucleons from lighter to heavier reaction partner.

Thus the entrance channel properties of the reacting system, in particular mass-asymmetry appears to play a major role in the nuclear reaction dynamics of nCN fission. Earlier various models predicted the onset of nCN process when the product Z_1Z_2 of the atomic numbers of target and projectile exceeds around 1600. However, recent investigations evoked considerable contribution from nCN fission around the Z_1Z_2 value of $\sim$1000 [25].

Another interesting aspect in the study of fusion-fission reactions is the fission fragment angular distribution which has attracted a great deal of attention in recent years. The interest in this field has been renewed with the observation that

anisotropies in these fragment angular distributions show anomalous features when they are compared to the standard point statistical model (SSPM) calculations, and is observed particularly in reactions of heavy ions on deformed, actinide nuclei at near and sub- barrier energies. The explanation of this anomaly is attributed to the admixture of non-equilibrated fission events such as QF, ICF or DIC etc along with the normal compound nuclear fission events [26]. Since nCN process also contributes in providing worthy information regarding nuclear structure just like CN process, so it is equally important to investigate nCN process for its possible implications in nuclear dynamics and related phenomena.

In order to understand the above mentioned decay processes, PCM for ground state decays is further developed to the study of decay of hot and rotating compound systems formed in heavy ion reactions and the model is known as the dynamical cluster-decay model (DCM) [27]- [32]. The main advantage of using this model, in context of nuclear dynamics, is that decay of excited compound nuclei is studied as a collective clusterization process for emissions of ER, IMFs as well as the nSF and SF, in contrast to the statistical models which follow different formalisms for different processes.

Multiple light particles (n, p, α) and γ rays, which are associated with the evaporation residue (ER) production, is understood as the fusion-evaporation process from the equilibrated CN in the statistical Hauser-Feshbach (HF) analysis [33], described in the evaporation codes such as LILITA and CASCADE. The HF formalism has been extended to include complex IMFs in light compound nuclei (A<80), for example in the BUSCO code [34] or in the extended HF method based on the scission-point picture [35], and the saddle-point "transition-state" model (TSM) [36]. An

alternative process for IMF production in the medium mass nuclei (A>100) is the binary decay of the compound nucleus in the statistical fission model of Moretto [37]. Thus, the two processes of ER and IMF emissions are considered separately using two different models (the HF analysis and Fission Models). Another advantage of DCM over other statistical models is that preformation probability enables us to make significant remarks about the nuclear structure of CN and its decaying fragments.

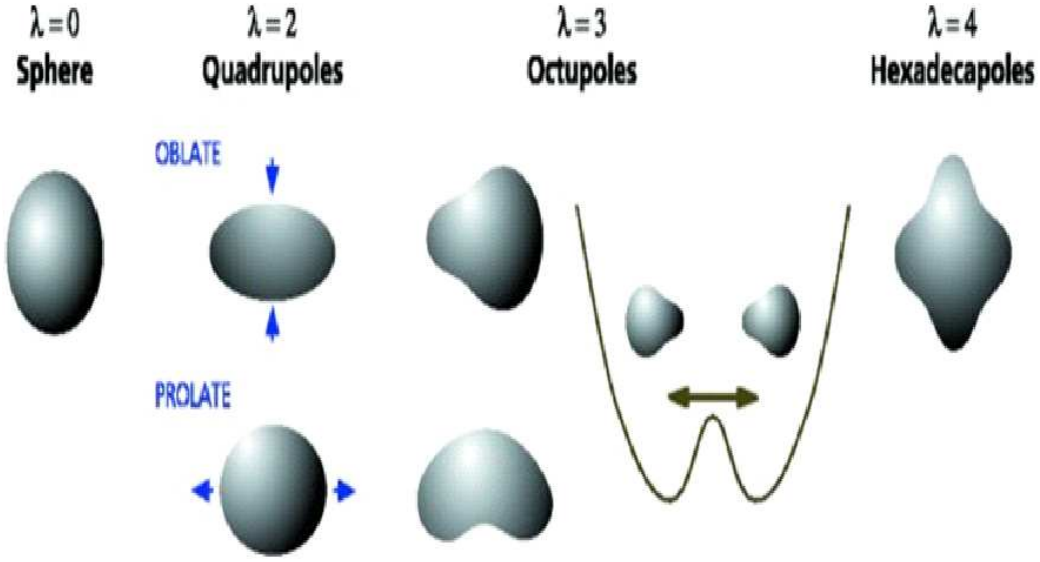

Figure 1.2 Schematic diagram for various multipole deformations in nuclei. For quadrupole deformations, there are two choices i.e. nuclear matter rotates on short axis (oblate) and on long axis (prolate).

Nuclei may also have extreme shapes, the higher multipole deformations, $\beta_\lambda(\lambda$=2,3,4) or extreme neutron-to-proton ratios. In general, elongated (prolate) and flattened (oblate) are most commonly observed deformed nuclear shapes. The different oscillations of the nuclear surface are shown in Fig. 1.2. The lowest multipole $\lambda = 2$ describe the quadrupole oscillation of the nuclear surface and it corresponds to quadrupole deformation and spheroidal shape. The next multipoles

λ =3, 4 represent the octupole, hexadecapole, oscillations of nuclear surface. Octupole deformation describes the reflection-asymmetry in the nuclear shape, giving the nucleus pear like shape. The contribution of these higher multipole deformations along with choice of appropriate orientations lead to enormous exotic shapes which in turn are immensely useful to understand various aspects of nuclear structure and dynamics at extreme conditions thereby providing important information for future experiments.

Deformed nuclei can be oriented either in the same plane (co-planar) or in different planes (non-coplanar). It has been observed that inclusion of deformations and orientations leads to the reduction of the barrier height and the increase of interaction radii for the collisions of co-planar, deformed nuclei [28,38,39]. This distribution of the barrier height results in a substantial enhancement of fusion cross-sections, thus making the fusion more probable at low energies. In addition to the co-planar collisions of deformed nuclei, efforts are now being made theoretically to understand the possibilities of including the non-coplanar collisions of the deformed nuclei.

Nuclear reactions, where deformed nuclei are engaged, are widely applied to the synthesis of superheavy elements in many laboratories around the world . The reactions of subbarrier fusion of strongly deformed F, Ne, and Mg isotopes play a very important role in the burning of stars and govern their evolution. Beside this, the proper choice of orientation of target and projectile contribute immensely and therefore need to be handled with care. In other words, wherever a deformed configuration is considered, the orientational behavior of nuclear systems cannot be ignored. It is relevant to mention here that the distance between mass centers of the massive reactants rely on the orientation of the deformed nuclei, which in turn

affects the fusion of heavy ions considerably. Interestingly the relative orientations of the approaching heavy ions affect the long-range Coulomb interaction [40, 41] as well as the short-range nuclear potential [39, 42].

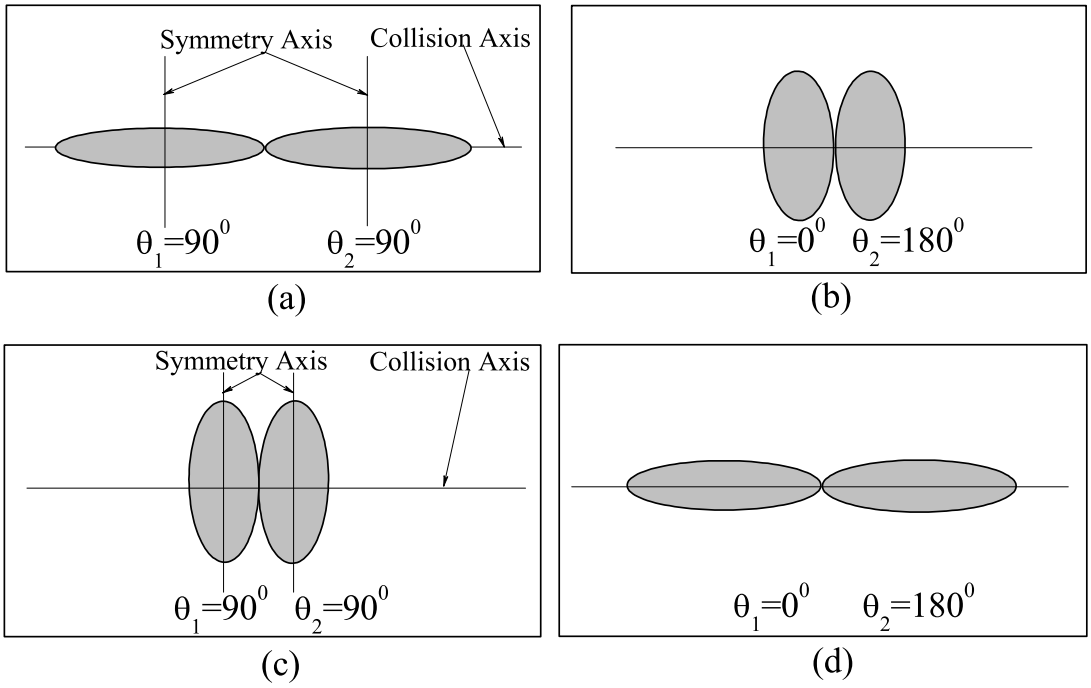

Figure 1.3 Schematic diagrams for deformed nuclei [(a),(b) oblate and (c),(d) prolate only] with corresponding optimum orientations along collision axis for "cold, elongated"[(a), (d)] or "hot, compact"[(b), (c)] configurations, from Table 1 [28].

A study based on the Quantum Mechanical Fragmentation Theory (QMFT) has suggested the optimum orientations for fusion of deformed nuclei based on the quadrupole deformations alone and also investigated the role of the sign of hexadecupole deformation in fusion reactions [28]. The optimum orientations are given for "cold, non-compact" and "hot, compact" fusion configurations corresponding to largest interaction radius (or lowest barrier) and smallest interaction radius (or highest barrier) respectively. A schematic diagram is illustrated in Fig. 1.3 (taken from [28]), only for prolate-prolate and oblate-oblate deformed colliding nuclei along

collision axis for both the "cold, elongated" and "hot, compact" configurations.

The orientations θ_i^{opt} are optimized (uniquely fixed) on the basis of the signs (+, -, or zero) of quadrupole deformations β_{2i} alone, not affected by the signs (+/-) of their hexadecapole deformations for both "hot" and "cold" fusion reactions [28]. For general treatment one may use compact orientations θ_i^c, which refer to collisions taking place at the minimum (smallest) interaction radius, and are termed as "cold" or "hot" depending on if the barrier is the lowest or highest [28], [29]. Such compact configurations [29] must be used for deformations higher than β_{2i}, particularly for, say, large, positive hexadecapole deformations β_{4i}, i.e., $\beta_{4i} >> 0$ for prolate deformed nuclei. It is to be noted that role of higher multipole deformations is also studied recently on PCM [13] and observed that inclusion of compact orientations θ_i^c with deformations up to β_{4i} is essential to study ^{14}C cluster/fragments in the radioactive decay of various parent nuclei.

As discussed above, deformation and orientation effects of nuclei are extremely important and hence need to be incorporated explicitly in order to account for proper nuclear dynamics. Beside the temperature and angular momentum effects in the above mentioned dynamical cluster-decay model (DCM), the deformations and orientation effects of the reaction partners and decaying products are also taken care of. In the present work, the decay of heavy mass nuclear systems ^{213,215,217}Fr*, ^{219,220}Ra* and ^{241}Pu* respectively, formed in different entrance channels, have been studied using DCM over a wide range of incident energies, comprising of both below- and above-barrier energies. Such a theoretical study of different nuclear systems is utilized to get better understanding of reaction mechanisms alongwith associated nuclear structure effects. The role of entrance channel effects, fission fragment

anisotropies, static and dynamic deformations, angular momentum, barrier modification effects, structure/sub-structure of fission fragments, shell effects, etc., have been investigated extensively. Application of DCM is also made to study ICF and subsequent decay processes along with the CF process and the results for the same are nicely compared with the available experimental data.

1.3 Organization of thesis

The thesis is organized in the following way:

Chapter 2 gives details of the Dynamical Cluster-decay Model (DCM) [27]- [32] for the decay of hot and rotating compound nucleus, and its ground-state version, the Preformed Cluster-decay Model (PCM), for spontaneous decay of radioactive nuclei [5, 6]. Both these models, based on the Quantum Mechanical Fragmentation Theory (QMFT) [14, 15] for binary fragmentation, uses a collective mass transfer process. Here the two contributing factors, the pre-formation probability P_0 of the decaying fragments and their penetrability P across the nuclear interaction barrier describe the decay of nuclei in ground and excited states. The deformation and orientation effects are duly incorporated in PCM as well as in DCM, together with the use of "optimum" or "compact" orientations, for incoming nuclei as well as for decaying fragments. The "cold" orientations are used for the case of ground state cluster radioactivity, in contrast to the case of excited nuclei where we use the "hot" orientations. The details of proximity potential, Coulomb interaction potential, rotational energy and binding energies are also described. It is relevant

to mention here that DCM is reformulation of PCM by making all its terms as temperature-dependent and using the temperature-dependent binding energies.

In **Chapter 3**, Application of DCM is made for first time to study the decay of an odd-mass nuclear systems ^{213,215,217}Fr*. The CN ^{215}Fr* is formed via two different asymmetric reaction channels ^{11}B+^{204}Pb and ^{18}O+^{197}Au [43]. Calculations of fission anisotropy and reaction channels chosen with respect to Bussinaro-Gallone critical asymmetry point of view, are explored for the first time for ^{215}Fr* system within the framework of DCM. The role of sticking versus non-sticking moment-of-inertia is discussed [44], which allows us to conclude that sticking limit is best suited to fusion excitation functions whereas non- sticking limit seems to support the fission anisotropy. The calculated results are compared nicely with the available experiment data [43] for both the reactions and confirm the entrance-channel independence of the decay of compound nucleus ^{215}Fr*. Further the role of magic shells and the qf contribution is also investigated [45] in fission cross-section, of ^{213,217}Fr* nuclei formed in ^{19}F+^{194,198}Pt reactions [16]. The deformation and orientation effects of nuclei are found to play a significant role for all the three ^{213,215,217}Fr* systems.

Chapter 4 deals with the decay of ^{219,220}Ra* formed in ^{10,11}B + ^{209}Bi reactions at different centre-of-mass energies, using DCM. Interestingly the calculated [46] complete fusion (CF) excitation functions for ^{219,220}Ra* compound systems and incomplete fusion (ICF) excitation functions for ^{219}Ra* system show good agreement with the reported experimental data [47] within one parameter fit of the model, without invoking significant contribution from qf. The main contribution to complete fusion cross-section comes from the fission cross-section at higher energies and evaporation residues contributes more at lower incident energies. The evaporation

residue cross-sections consist of significant contribution from the neutron evaporation cross-sections along with smaller contribution from other charged particle evaporation residues produced through the αxn and pxn ($x = 2, 3, 4$) emission channels in ^{219}Ra system. It is relevant to mention here that DCM is applied for the first time in reference to subsequent decay processes in this work. The exclusive role of deformations and angular momentum is discussed in reference to the dynamics of reaction under study. The "barrier modification" ΔV_B is more prominent at lower incident energies and angular momentum values, and the dependence of ΔV_B on $E_{c.m.}$ and or ℓ-values is almost independent of projectile mass.

In **Chapter 5**, the role of static and dynamic deformations is investigated [48] in the decay of hot and rotating compound nucleus ^{241}Pu*, formed in the reaction ^{9}Be + ^{232}Th at both below- and above- barrier energies [49] on the basis of DCM. The dynamic deformations are used for the first time in DCM. It is observed that the inclusion of dynamic deformations of the decaying fragments changes the potential energy surface (PES) quite significantly and as a result the relative preformation probabilities P_0 for all the fragments gets changed accordingly. Similarly the barrier characteristics are also modified with the inclusion of temperature dependent deformations of outgoing fragments, thereby affecting their tunneling path through the barrier. The interesting feature of this study is that although the PES in the fissioning region are different for static and dynamical choice of deformation, the distribution yield remains asymmetric for both static as well as dynamic deformed considerations up to hexadecapole in the decay of ^{241}Pu*. Also, the fission fragment anisotropies calculated using DCM, are found to be significantly larger than the statistical saddle point model predictions at sub-barrier energies, thereby indicating

contribution from noncompound nucleus fission in accordance with [49].

In **Chapter 6**, the role of higher-multipole deformations (up to hexadecapole) and orientations of nuclei, are duly incorporated in PCM [13] to address the rare nuclear phenomenon known as cluster radioactivity. We observe that the inclusion of higher multipole deformations (β_2-β_4), together with cold "compact" orientations of nuclei, is essential for investigating the decay of ^{14}C cluster emitted from various parent nuclei from the trans-lead region. The calculated decay half-lives and branching ratios of ^{14}C clusters with respect to α-decay are found in nice agreement with measured values [2]. However for other observed clusters namely, ^{18,20}0, ^{22,24,26}Ne, ^{28,30}Mg, ^{34}Si, etc., the inclusion of quadrupole deformation (β_2) alone, with "optimum" orientations was found good enough to fit experimental half-life times in earlier work [9, 10]. The interesting feature of this study is that preformation factor P_0 is shown to get modified significantly with the inclusion of deformation and orientation effects whereas penetrability and assualt frequency plays a silent role. Also, the decay half-lives are shown to be strongly dependent on the Q-value of the decay process. Further, the potential energy surface for the fragmentation process in the ground state decay of parent nucleus, remain insensitive to the inclusion of angular-momentum effects.

Finally **Chapter 7** concludes the over all work of the thesis. Brief notes regarding the significance of the work and scope for extension of this work in future is discussed.

Bibliography

[1] H. J. Rose and G. A. Jones, Nature **307**, 245 (1984).

[2] R. K. Gupta and W. Greiner, Int. J. Mod. Phys. E **3**, 335 (1994).

[3] R. Bonetti and A. Guglielmetti, Rom. Rep. Phys. **59**, 301 (2007).

[4] A. Săndulescu, D. N. Poenaru, and W. Greiner, Sov. J. Part. Nucl. **11**, 528 (1980).

[5] S. S. Malik and R. K. Gupta, Phys. Rev. C **39**, 1992 (1989).

[6] S. Kumar and R. K. Gupta, Phys. Rev. C **55**, 218 (1997).

[7] M. Balasubramaniam, S. Kumarasamy, N. Arunachalam, and R. K. Gupta, Phys. Rev. C **70**, 017301 (2004).

[8] Z. Ren, C. Xu, and Z. Wang, Phys. Rev. C **70**, 034304 (2004).

[9] S. K. Arun, R. K. Gupta, B. B. Singh, S. Kanwar, and M. K. Sharma, Phys. Rev. C **79**, 064616 (2009).

[10] S. K. Arun, R. K. Gupta, S. Kanwar, B. B. Singh, and M. K. Sharma, Phys. Rev. C **80**, 034317 (2009).

[11] A. Săndulescu, R. K. Gupta, F. Carstoiu, M. Horoi and W. Greiner, Int. J. Mod. Phys. E **1**, 1379 (1992); R. K. Gupta, M. Horoi, A. Sandulescu, M. Greiner and W. Scheid, J. Phys. G: Nucl. Part. Phys. C **19**, 2063 (1993).

[12] S. Misicu, and D. Protopopescu, Acta Physcia Polonica B **30**, 127 (1999).

[13] G. Sawhney, M. K. Sharma, and R. K. Gupta, Phys. Rev. C **83**, 064610 (2011).

[14] J. Maruhn and W. Greiner, Phys. Rev. Lett. **32**, 548 (1974).

[15] R. K. Gupta, W. Scheid and W. Greiner, Phys. Rev. Lett. **35**, 353 (1975).

[16] K. Mahata, S. Kailas, A. Shrivastava, A. Chatterjee, P. Singh, S. Santra, and B. S. Tomar, Phys. Rev. C **65**, 034613 (2002).

[17] J. G. Keller, B. B. Back, B. G. Glagola, D. Henderson, S. B. Kaufman, S. J. Sanders, R. H. Siemssen, F. Videbaek, B. D. Wilkins, and A. Worsham, Phys. Rev. C **36**, 1364 (1987).

[18] J. Toke, R. Bock, D. X. Dai, A. Gobbi, S. Gralla, K. D. Hildenbrand, J. Kuzminski, W. J. F. Muller, A. Olmi, H. Stelzer, B. B. Back, and S. Bjornholm, Nucl. Phys. A **440**, 327 (1985).

[19] D. J. Hinde, M. Dasgupta, J. R. Leigh, J. C. Mein, C. R.Morton, J. O. Newton, and H. Timmers, Phys. Rev. C **53**, 1290 (1996).

[20] J. C. Mein, D. J. Hinde, M. Dasgupta, J. R. Leigh, J. O. Newton, and H. Timmers, Phys. Rev. C **55**, R995 (1997).

[21] H. C. Britt and A. R. Quinton, Phys. Rev. **124**, 877 (1961).

[22] T. Inamura, A. C. Kahler, D. R. Zolnowski, U. Garg, T. T. Sugihara, and M. Wakai, Phys. Rev. C **32**, 1539 (1985).

[23] K. Siwek-Wilczynska, E. H. du Marchie van Voorthuysen, J. van Popta, R. H. Siemssen, and J. Wilczynski, Phys. Rev. Lett **42**, 1599 (1979).

[24] H. Morgenstern, W. Bohne, W. Galster, K. Grabisch, and A. Kyanowski, Phys. Rev. Lett. **52**, 1104 (1984).

[25] R. Rafiei, R. G. Thomas, D. J. Hinde, M. Dasgupta, C. R. Morton, L. R. Gasques, M. L. Brown, and M. D. Rodriguez, Phys. Rev. C **77**, 024606 (2008).

[26] V. S. Ramamurthy and S. S. Kapoor, Phys. Rev. Lett **54**, 178 (1985).

[27] M. Balasubramaniam, R. Kumar, R. K. Gupta, C. Beck and W. Scheid, J. Phys. G: Nucl. Part. Phys. **29**, 2703 (2003); R. K. Gupta, R. Kumar, N. K. Dhiman, M. Balasubramaniam, W. Scheid, and C. Beck, Phys. Rev. C **68**, 014610 (2003).

[28] R. K. Gupta, M. Balasubramaniam, R. Kumar, N. Singh, M. Manhas, and W. Greiner, J. Phys. G: Nucl. Part. Phys. C **31**, 631 (2005).

[29] R. K. Gupta, M. Manhas, and W. Greiner, Phys. Rev. C **73**, 054307 (2006).

[30] B. B. Singh, M. K. Sharma and R. K. Gupta, Phys. Rev. C **77**, 054613 (2008).

[31] M. K. Sharma, S. Kanwar, G. Sawhney, R. K. Gupta, and W. Greiner, J. Phys. G: Nucl. Part. Phys. **38**, 055104 (2011); D. Jain, R. Kumar, M. K. Sharma, and R. K. Gupta, Phys. Rev. C **85**, 024615 (2012).

[32] M. Kaur, R. Kumar, and M. K. Sharma, Phys. Rev. C **85**, 014609 (2012); M. Kaur and M. K. Sharma *ibid.* **85**, 054605 (2012).

[33] S. J. Sanders, A. Szanto de Toledo, and C. Beck, Phys. Rep. **311**, 487 (1999).

[34] J. Gomez del Campo, R. L. Auble, J. R. Beene, M. L. Halbert, H. J. Kim, A. D'Onofrio, and J. L. Charvet, Phys. Rev. C **43**, 2689 (1991).

[35] T. Matsuse, C. Beck, R. Nouicer, and D. Mahboub, Phys. Rev. C **55**, 1380 (1997).

[36] S. J. Sanders, Phys. Rev. C **44**, 2676 (1991); S. J. Sanders, D. G. Kovar, B. B. Back, C. Beck, D. J. Henderson, R. V. F. Janssens, T. F. Wang, and B. D. Wilkins, Phys. Rev. C **40**, 2091 (1989).

[37] L. G. Moretto, Nucl. Phys. A **247**, 211 (1975).

[38] A. Iwamoto, P. Möller, J. R. Nix, and H. Sagawa, Nucl. Phys. A **596**, 329 (1996).

[39] N. Malhotra and R. K. Gupta, Phys. Rev. C **31**, 1179 (1985).

[40] C. Y. Wong, Phys. Lett. **26B**, 120 (1968).

[41] L. Wilets, E. Guth, and J. S. Tenn, Phys. Rev. **156**, 1349 (1967); H. Holm, W Scheid, and W. Greiner, Phys. Lett. **24**, 404 (1970); A. S. Jensen and C. W. Wong, Phys. Rev. C **1**, 1321 (1970); P. W. Riesenfeldt and T. D. Thomas, *ibid.* **2**, 711 (1970).

[42] M. Seiwert, W. Greiner, V. Oberacker, and M. J. Rhoades-Brown, Phys. Rev. C **29**, 477 (1984).

[43] S. Appannababu, S. Mukherjee, N. L. Singh, P. K. Rath, G. K. Kumar, R. G. Thomas, S. Santra, B. K. Nayak, A. Saxena, R. K. Choudhury, K. S. Golda, A. Jhingan, R. Kumar, P. Sugathan, and H. Singh, Phys. Rev. C **80**, 024603 (2009).

[44] M. K. Sharma, G. Sawhney, R. K Gupta, and W. Greiner, J. Phys. G: Nucl. Part. Phys. **38**, 105101 (2011); M. K. Sharma, G. Sawhney, S. Kanwar, and R. K Gupta, Mod. Phys. Lett. A **25**, 2022 (2010).

[45] M. K. Sharma, S. Kanwar, G. Sawhney, and R. K. Gupta, Phys. Rev. C **85**, 064602 (2012).

[46] G. Sawhney and M. K. Sharma, Eur. Phys. J. A **48**, 57 (2012).

[47] L. R. Gasques, D. J. Hinde, M. Dasgupta, A. Mukherjee, and R. G. Thomas, Phys. Rev. C **79**, 034605 (2009).

[48] G. Sawhney, R. Kumar, and M. K. Sharma, Phys. Rev. C (under review).

[49] S. Appannababu, R. G. Thomas, L. S. Danu, P. K. Rath, Y. K. Gupta, B. V. John, B. K. Nayak, D. C. Biswas, A. Saxena, S. Mukherjee, and R. K. Choudhury, Phys. Rev. C **83**, 067601 (2011).

Chapter 2

Methodology

2.1 Introduction

The main aim of this work is to study various types of emission processes from the ground state of parent nuclei as well as from the excited state of compound nucleus (CN) formed in low energy nuclear reactions. The ground state cluster decay of radioactive nuclei have been studied within the preformed cluster decay model (PCM) [1]- [6]. For the decay of excited compound systems, the dynamical cluster-decay model (DCM) [7]- [22] is used, which is reformulation of PCM for the ground state decay. The advantage of using the DCM is that it gives the relative probability of all channels, through which an excited compound nucleus can decay. It is relevant to mention that deformations and orientation effects of the reaction partners and decay products are explicitly included along with temperature and angular momentum contribution in this model.

The DCM has been used to investigate the decay paths of a large number of nuclear systems in light mass (^{48}Cr*, ^{56}Ni*), intermediate mass (^{116,118,122}Ba*, ^{164}Yb*,

^{176,182,188,196}Pt*, ^{202}Pb*), heavy (^{246}Bk*, ^{213,215,217}Fr*, ^{204}Po*,^{219,220}Ra*, ^{241}Pu*) and super-heavy (^{286}112*, ^{286}114*, ^{297}117*) regions, during last few years over a wide range of incident center-of-mass (c.m.) energies. Details of PCM and DCM are given in Sec. 2.3 and 2.4, respectively, both of which originate from the Quantum Mechanical Fragmentation Theory, (QMFT) [23]- [36] (Sec. 2.2) which, is based on collective co-ordinate picture. It is the only theory, given prior to experiments, that brings out clearly the applicability of the quantum concept of probability and role of shell effects not only for fusion reactants but also for the other two related processes of fission and cluster radioactivity. In QMFT the potential is calculated using macro-microscopic method of Strutinsky [37]. This average two body potential successfully explains the cold and hot fusion reaction dynamics. This theory is based on the fact that the fragments are pre-born prior to the decay of the compound nucleus. The quantum mechanical preformation probability P_0 of the decaying fragments or clusters formed in the mother nucleus can be calculated by solving a stationary Schrödinger equation in mass fragmentation coordinate. This inclusion of preformation probability enables us to make significant remarks about the nuclear structure of CN system and its decaying fragments. Once the clusters are formed, their penetration probability P across the interaction barrier can be calculated by using the WKB approximation.

The calculations of preformation probability P_0 and penetration probability P are presented in Sec. 2.2.9 and 2.2.10. The details of assault frequency ν_0, with which the preformed cluster tries to tunnel the barrier in the ground state decay, is given in Sec. 2.2.11. The concept of "barrier lowering" and fission fragment anisotropy are discussed in Sec. 2.4.1 and 2.4.2, respectively.

2.2 Quantum Mechanical Fragmentation Theory

The QMFT [23]- [36] is a unified description of two body channels in both fusion and fission processes. Here the quantities essential for the description of the nuclear dynamics are the potential energy surfaces and the mass parameters defining the kinetic energy of the system. The static properties of nuclear system are determined by the potential energy alone. In QMFT, the quantum mechanical concept of probability is utilized to investigate the role of shell effects in the fusion, fission and cluster radioactivity. The theory is worked out in terms of the following collective variables:

(i) relative separation coordinate R between the two nuclei or, in general, two fragments (or, equivalently, the length parameter $\lambda = L/2R_0$, with L as the length of the nucleus and R_0 as the radius of an equivalent spherical nucleus).

(ii) The deformations co-ordinates $\beta_{\lambda i}$ (λ=2,3.4... and i=1,2) of the colliding nuclei.

(iii) The orientation degrees of freedom $\theta_i (i = 1, 2)$ of the deformed nuclei (see Fig. 2.1).

(iv) Azimuthal angle ϕ between the principal planes of the two colliding nuclei.

(v) Neck parameter ε, defined by the ratio $\varepsilon = E_0/E'$ for the interaction region ($R < R_1 + R_2$, R_i (i=1, 2) is the radius of the two nuclei). Here E_0 is the actual height of the barrier and E' is the fixed barrier of the two center oscillator. $\epsilon = 0$ represents a broad neck formation, whereas $\epsilon = 1$ gives that the neck is fully squeezed in, corresponding to the asymptotic region ($R > R_1 + R_2$).

(vi) Mass and charge fragmentation co-ordinates [23, 24, 35].

For two body channels, the mass and charge fragmentation for separated nu-

clei/fragments are defined by the mass and charge-asymmetry coordinates as

$$\eta = \frac{A_1 - A_2}{A}; \qquad \eta_Z = \frac{Z_1 - Z_2}{Z} \tag{2.1}$$

Similarly, the neutron asymmetry coordinate [24]

$$\eta_N = \frac{N_1 - N_2}{N}, \tag{2.2}$$

can also be used, but it is sufficient to treat only two of them as dynamical coordinates since they are related as

$$\eta = \frac{Z}{A}\eta_Z + \frac{N}{A}\eta_N \tag{2.3}$$

Here $A = A_1 + A_2$, $Z = Z_1 + Z_2$ and $N = N_1 + N_2$. A_i, Z_i and N_i $(i = 1, 2)$ are respectively the mass number, the charge number and the neutron number of two fragments. A, Z and N are respectively the mass number, charge number and neutron number of the compound system. The limiting values of η are $0 \leq |\eta| \leq 1$ and thus allows a unified description of a few-nucleon, multi-nucleon (a cluster) transfer, a large-mass transfer, the complete fusion ($|\eta| = 1$) of nuclei and the symmetric ($\eta = 0$), asymmetric and super-asymmetric fission of a compound nucleus. The η_Z coordinate gives the associated charge distribution effects. In terms of these collective coordinates and their velocities, the collective Hamiltonian can be written as (taking β to stand for $\beta_{\lambda 1}$ and $\beta_{\lambda 2}$; λ=2,3,4....).

$$H = K(\mathbf{R}, \beta, \varepsilon, \eta, \eta_Z; \dot{\mathbf{R}}, \dot{\beta}, \dot{\varepsilon}, \dot{\eta}, \dot{\eta}_Z) + V(\mathbf{R}, \beta, \varepsilon, \eta, \eta_Z). \tag{2.4}$$

For the compound nucleus formation, the neck parameter $\epsilon = 0$ is assumed, since once the neck formation starts between the two colliding nuclei, then fission phenomenon can never be stopped, i.e. excited compound nucleus will proceed towards the disintegration process.

For the potential $V(\eta, \eta_Z, R)$, minimized in the η_Z co-ordinate, Schrödinger wave equation in terms of mass parameters η and relative separation R co-ordinates can be written as:

$$H(\eta, R)\psi(\eta, R) = E(\eta, R)\psi(\eta, R) \tag{2.5}$$

with the Hamiltonian,

$$H(\eta, R) = K(\eta) + K(R) + K(\eta, R) + V(\eta) + V(R) + V(\eta, R) \tag{2.6}$$

Here, K refers to the kinetic energy and V to the collective potential energy. The mass parameters B_{ij}, defining the kinetic energy term K in the above Eqs. (2.4) and (2.6) are either the consistently calculated cranking masses using the Asymmetric Two-Center Shell Model ($ATCSM$) or the classical hydrodynamical masses, which are shown to have good agreement with microscopic cranking calculations. The coupling term of the kinetic energy $K(\eta, R)$, proportional to $\frac{\partial^2}{\partial\eta\partial R}$, is neglected here, since the coupled cranking masses are very small [23, 24], ($\mathrm{B}_{R\eta} \ll (B_{RR}B_{\eta\eta})^{1/2}$ and $\mathrm{B}_{R\eta_Z} \ll (B_{RR}B_{\eta_Z\eta_Z})^{1/2}$). Same is true for the coupling term of potential energy $V(\eta, R)$.

Therefore, in a decoupled approximation [36], the Schrödinger equation (2.5) can

be solved for which the Hamiltonian takes the form:

$$H = -\frac{\hbar^2}{2\sqrt{B_{\eta\eta}}}\frac{\partial}{\partial\eta}\frac{1}{\sqrt{B_{\eta\eta}}}\frac{\partial}{\partial\eta} - \frac{\hbar^2}{2\sqrt{B_{RR}}}\frac{\partial}{\partial R}\frac{1}{\sqrt{B_{RR}}}\frac{\partial}{\partial R} + V(\eta) + V(R). \tag{2.7}$$

For decoupled Hamiltonian (2.7), Schrödinger wave equation (2.5) can be separated for the two co-ordinates η and R as follows,

$$\left[-\frac{\hbar^2}{2\sqrt{B_{\eta\eta}}}\frac{\partial}{\partial\eta}\frac{1}{\sqrt{B_{\eta\eta}}}\frac{\partial}{\partial\eta} + V(\eta)\right]\psi^{\nu}(\eta) = E^{\nu}_{\eta}\psi^{\nu}(\eta) \tag{2.8}$$

and

$$\left[-\frac{\hbar^2}{2\sqrt{B_{RR}}}\frac{\partial}{\partial R}\frac{1}{\sqrt{B_{RR}}}\frac{\partial}{\partial R} + V(R)\right]\psi^{\nu}(R) = E^{\nu}_{R}\psi^{\nu}(R) \tag{2.9}$$

with

$$\psi(\eta, R) = \psi(\eta)\psi(R) \tag{2.10}$$

and

$$E = E_{\eta} + E_{R} \tag{2.11}$$

The states $\psi^{\nu}(\eta)$ are the vibrational states in the potential $V(\eta)$ and are labelled by the quantum numbers $\nu = 0, 1, 2$, etc. In the following subsections, we first discuss the various terms of Schrödinger wave equations (2.8) and (2.9) and then give the solution of Eq. (2.8) for the determination of preformation probability $P_0 \propto |\psi^0(\eta)|^2$.

2.2.1 The Scattering Potential $V(R)$

For a fixed η i.e for a given target projectile (A_1, A_2) combination, the scattering potential $V(R)$ in Eq. (2.9) is defined as the sum of the temperature-, deformations-

and orientations-dependent Coulomb, proximity and angular momentum-dependent potentials, i.e.

$$\begin{aligned} V(R,\ell,T) &= V_c(R,Z_i,\beta_{\lambda i},\theta_i,\phi,T)+V_p(R,A_i,\beta_{\lambda i},\theta_i,\phi,T) \\ &+ V_\ell(R,A_i,\beta_{\lambda i},\theta_i,\phi,T) \end{aligned} \tag{2.12}$$

For co-planar nuclei (Fig. 2.1) ϕ=0^0, and for spherical-plus-deformed nuclear collisions, only one orientation angle θ is enough, referring to the rotationally-symmetric deformed nucleus.

2.2.2 The Fragmentation potential $V(\eta)$

The temperature dependent collective potential energy or the fragmentation potential $V(\eta,R,T)$, appearing in Eq. (2.8), is calculated as,

$$\begin{aligned} V(\eta,R,\ell,T) &= -\sum_{i=1}^{2} B_i(A_i,Z_i,\beta_{\lambda i},T)+V_c(R,Z_i,\beta_{\lambda i},\theta_i,\phi,T) \\ &+ V_p(R,A_i,\beta_{\lambda i},\theta_i,\phi,T)+V_\ell(R,A_i,\beta_{\lambda i},\theta_i,\phi,T) \end{aligned} \tag{2.13}$$

The fragmentation potential $V(\eta)$, is calculated at a fixed distance $R = R_1+R_2+\Delta R$ for consideration of deformed and oriented reaction product, with

$$R_i(\alpha_i,T) = R_{0i}(T)[1+\sum_{\lambda}\beta_{\lambda i}Y_\lambda^{(0)}(\alpha_i)], \tag{2.14}$$

and

$$R_{0i}(T) = [1.28A_i^{1/3}-0.76+0.8A_i^{-1/3}]\times(1+0.0007T^2). \tag{2.15}$$

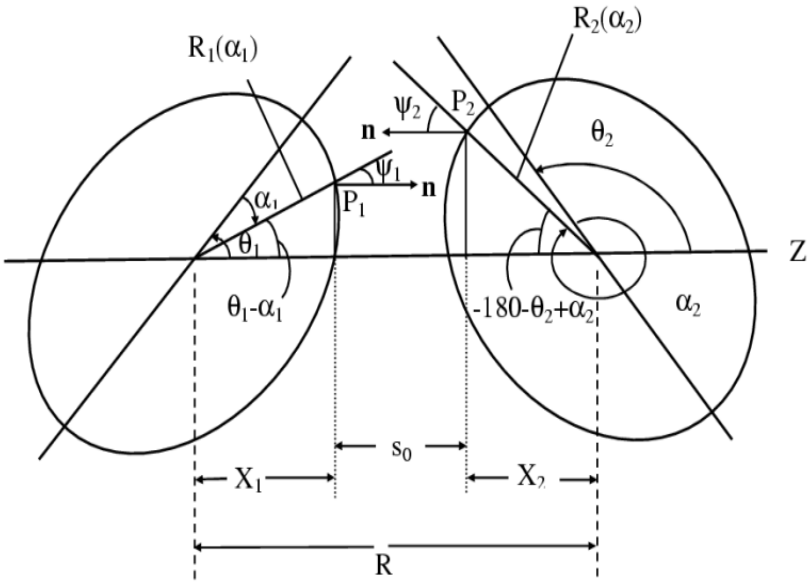

Figure 2.1 Schematic configurations of two axially symmetric deformed, oriented nuclei, lying in the same plane and for various θ_1 and θ_2 values in the range 0^0 to 180^0 [38]. The θ's are measured in anti-clockwise from the colliding axis and the angle α's in clockwise from the symmetry axis.

Here λ=2,3,4... and α_i is an angle that the radius vector R_i of the colliding nuclei makes with the symmetry axis (see Fig. 2.1), measured clockwise.

B_i (i=1,2) appearing in Eq. (2.13), are the binding energies of the two nuclei, available from the experimental data of Audi-Wapstra [39]. Wherever the experimental B's are not available, the theoretical binding energies of Möller *et al.* [40] are used. Note that within the Strutinsky renormalization procedure [37], the binding energies contain both the macroscopic (liquid drop part) and the microscopic (shell correction) part, which allows us to define the binding energy B of a nucleus at temperature T as the sum of liquid drop energy $V_{LDM}(T)$ and shell correction $\delta U(T)$ i.e

$$B(T) = V_{LDM}(T) + \delta U exp\bigg(- \frac{T^2}{{T_0}^2}\bigg). \tag{2.16}$$

The calculations of fragmentation potential involve all the possible decay channels and the number of all such possible decay channels becomes more and more with the increasing mass of the mother nucleus. The nuclear temperature T (in MeV) is related to the excitation energy E^*_{CN} of the compound nucleus, through a semi-empirical statistical relation as:

$$E^*_{CN} = E_{c.m.} + Q_{in} = \frac{1}{a}AT^2 - T \qquad (MeV). \tag{2.17}$$

where a = 9-11 depending on the mass of the compound nucleus. Q_{in} is the entrance channel Q-value given by $Q_{in} = B_1 + B_2 - B_{CN}$ where B's are the binding energies.

2.2.3 Liquid drop energies and their temperature dependence

The T dependent liquid drop part of the binding energy $V_{LDM}(T)$ is taken from Davidson *et al.* [41], based on the semi-empirical mass formula of Seeger [42], as

$$\begin{aligned} V_{LDM}(A,Z,T) &= \alpha(T)A + \beta(T)A^{\frac{2}{3}} + \left(\gamma(T) - \frac{\eta(T)}{A^{\frac{1}{3}}}\right)\left(\frac{I^2 + 2 \mid I \mid}{A}\right) \\ &\quad + \frac{Z^2}{R_0(T)A^{\frac{1}{3}}}\left(1 - \frac{0.7636}{Z^{\frac{2}{3}}} - \frac{2.29}{[R_0(T)A^{\frac{1}{3}}]^2}\right) + \delta(T)\frac{f(Z,A)}{A^{\frac{3}{4}}}, \end{aligned} \tag{2.18}$$

where

$$I = a_a(Z - N), \quad a_a = 1.0,$$

and, respectively, for even-even, even-odd, and odd-odd nuclei,

$$f(Z, A) = (-1, 0, 1).$$

For $T = 0$, Seeger [42] obtained the constants, by fitting all even-even nuclei and 488 odd-A nuclei available at that time, as

$$\alpha(0) = -16.11\text{MeV}, \quad \beta(0) = 20.21\text{MeV},$$

$$\gamma(0) = 20.65\text{MeV}, \quad \eta(0) = 48.00\text{MeV},$$

with the pairing energy term from Ref. [43],

$$\delta(0) = 33.0\text{MeV}.$$

For the large amount of data available now on ground-state binding energies, these constants of $V_{LDM}(T = 0)$ needed re-fitting, which was done [7, 8, 12] to get the experimental binding energies with shell corrections determined from Myers and Swiatecki [44]. This was first done in [7,8] for the 1995 Audi Wapstra Tables [45] of binding energies, and more recently in [12] for the 2003 Tables [39].

The same procedure is applied to neutron- and proton-clusters of $x(\geq 1)$ nucleons, by defining [46,47] the binding energy of a cluster with x-neutrons as x times the binding energy of one-neutron (equivalently, the mass excess Δm_n=8.0713 MeV),

$$B(A_2 = xn) = x\Delta m_n, \tag{2.19}$$

and the same for proton-clusters, as

$$B(A_2 = xp) = x\Delta m_p - a_c A_2^{5/3} \tag{2.20}$$

with Δm_p=7.2880 MeV, the one-proton mass excess or equivalently the binding energy of one-proton. The additional term due to a_c (=0.7053 MeV [44]) is the disruptive Coulomb energy ($= -a_c(Z_2^2/A_2^{1/3})$) between the x-protons (here $xp = Z_2 = A_2$).

2.2.4 Shell corrections and their temperature dependence

The shell corrections according to the "empirical" formula of Myers and Swiatecki [44], for spherical shapes, are

$$\delta U = C\left[\frac{F(N)+F(Z)}{(A/2)^{\frac{2}{3}}} - cA^{\frac{1}{3}}\right] \tag{2.21}$$

where

$$F(X) = \frac{3}{5}\left(\frac{M_i^{\frac{5}{3}} - M_{i-1}^{\frac{5}{3}}}{M_i - M_{i-1}}\right)(X - M_{i-1}) - \frac{3}{5}\left(X^{\frac{5}{3}} - M_{i-1}^{\frac{5}{3}}\right) \tag{2.22}$$

with $X = N$ or Z, $M_{i-1} < X < M_i$ and M_i as the magic numbers 2, 8, 14 (or 20), 28, 50, 82, 126 and 184 for both neutrons and protons. The constants $C = 5.8\ MeV$ and $c = 0.26$. The temperature dependence of shell corrections δU is obtained as given in Eq. (2.16), decreasing exponentially with T_0=1.5 MeV.

At higher excitation energies, the shell corrections vanish completely and only the liquid drop part of energy is present. The shell corrections play an important role in determining or empirical fitting of nuclear masses, because the nuclear masses

calculated by using the smooth liquid drop formula show large deviations with respect to the experimental masses. It means that in the experimental masses there exist deep minima at specific neutron and/or proton numbers indicating the presence of shell structure, the so-called magic numbers in nuclei. This characteristic behavior cannot be reproduced by the liquid drop part alone, which means that the introduction of microscopic shell correction in the mass formula is essential. Thus, shell corrections accounts for the removal of deviation from the liquid drop calculations (uniform distribution of nucleons), and are defined, within Strutinsky [37] method as

$$\delta U = U - \tilde{U} \tag{2.23}$$

where, $U = \sum_\nu E_\nu 2n_\nu$ is the sum over all occupied single particle states and

$$\tilde{U} = 2 \int_{-\infty}^{\tilde{\lambda}} E\tilde{g}(E)dE. \tag{2.24}$$

is the average energy for uniform distribution. In general, the microscopic shell correction, along with the liquid drop part, give a proper description of the binding energy of the nucleus. This method, however, does not give a proper description of light mass nuclei. The difficulty is the inadequacy of shell model for very light nuclei. For this reason, the macro-microscopic calculations of Möller *et al.* [40] are tabulated for $Z \geq 8$ only. Alternatively, one can use the empirical shell correction method of Myers-Swiatecki [44] which again is not satisfactory for light nuclei ($Z \leq 16$). Gupta and collaborators have modified this empirical method and obtained a better description of the shell corrections for the light as well as heavy mass region, i.e, $1 \leq Z \leq 118$ [8].

2.2.5 The Proximity Potential for deformed, oriented, coplanar nuclei

When two surfaces approach each other within a small distance of less than $\sim 2fm$, comparable with the surface thickness of interacting nuclei, or when a nucleus is at the verge of dividing into two fragments, then the two surfaces actually face each other across a small gap or crevice. In both cases, the surface energy term alone could not give rise to the strong attraction that is observed when the two surfaces are brought in close proximity. Such additional attractive forces are called proximity forces and the additional potential due to these forces is called the proximity potential. Blocki *et al.* [48] have reanalyzed and extended a theorem, originally due to Deryagin [49], according to which the force between two gently curved surfaces in close proximity is proportional to the interaction potential per unit area between the two flat surfaces. The original expression of Blocki based on the pocket formula was for spherical nuclei, and is given by

$$\begin{aligned} V_P(s_0) &= f(sh., geo.)\Phi(s_0) \\ &= 4\pi\bar{R}\gamma b\Phi(s_0). \end{aligned} \tag{2.25}$$

$\Phi(s_0)$ is the universal function, independent of the shapes of nuclei or the geometry of nuclear system, but depends on the minimum separation distance s_0, as

$$\Phi(s_0) = \begin{cases} -\frac{1}{2}(s_0 - 2.54)^2 - 0.0852(s_0 - 2.54)^3 \\ -3.437exp(-\frac{s_0}{0.75}) \end{cases} \tag{2.26}$$

respectively, for $s_0 \leq 1.2511$ and $s_0 \geq 1.2511$. Here, s_0 is defined in units of b, i.e.

s_0 is s_0/b. This function is defined for negative (the overlap region), zero (touching configuration) and positive values of s_0. For a fixed R, the minimum distance s_0 is defined as

$$s_0 = R - R_1 - R_2 \tag{2.27}$$

where R_i is defined in Eq. (2.14). b is the diffuseness of the nuclear surface given by

$$b = \left[\pi/2\sqrt{3}\ln 9\right]_{t_{10-90}} \tag{2.28}$$

where t_{10-90} is the thickness of the surface in which the density profile changes from 90% to 10%. The value of b$\sim$1 fm. The γ is the specific nuclear surface tension given by

$$\gamma = 0.9517\left[1 - 1.7826\left(\frac{N-Z}{A}\right)^2\right] MeV fm^{-2} \tag{2.29}$$

$\overline{R}$ is the mean curvature radius of the reaction partners, characterizing the gap, which for spherical nuclei is given by

$$\overline{R} = \frac{R_1 R_2}{R_1 + R_2} \tag{2.30}$$

The proximity potential [50] for hot deformed nuclei is given as

$$V_p(A_i, \beta_{\lambda i}, \theta_i, T) = 4\pi\bar{R}(T)\gamma b(T)\Phi(s_0(T)). \tag{2.31}$$

and surface thickness parameter,

$$b(T) = 0.99(1 + 0.009T^2) \tag{2.32}$$

Fig. 2.1 shows a schematic configuration of two axially symmetric deformed, oriented nuclei, lying in the same plane ($\phi = 0^0$), for various θ_1 and θ_2 values in the range 0^0 to 180^0. θ_i is the angle of orientation, defined as an angle between the symmetry axis and the axis of collision, with it's rotation measured in anti-clockwise direction from the axis of collision. α_i is an angle between the symmetric axis and the radius vector $R_i(\alpha_i)$ of the colliding nuclei, measured in clockwise direction from the symmetry axis of the nucleus.

For the axially symmetric shapes, the nuclear radius parameter (to all higher multipole orders λ=2,3,4,....) is given by Eqs. (2.14) and (2.15). In terms of the radii of curvature R_{i1} and R_{i2} in the principal planes of curvature of each of the two nuclei (i=1,2) at the points of closest approach (defining s_0 in Fig. 2.1), the mean curvature radius $\bar{R}$ for deformed, oriented nuclei is given by

$$\begin{aligned} \frac{1}{\bar{R}^2} &= \frac{1}{R_{11}R_{12}} + \frac{1}{R_{21}R_{22}} + \left[\frac{1}{R_{11}R_{21}} + \frac{1}{R_{12}R_{22}}\right] sin^2\phi \\ &+ \left[\frac{1}{R_{11}R_{22}} + \frac{1}{R_{21}R_{12}}\right] cos^2\phi. \end{aligned} \tag{2.33}$$

Here, ϕ is the azimuthal angle between the principal planes of curvature of two nuclei (for co-planar nuclei ϕ=0^0). The four principal radii of curvature are

$$\begin{aligned} R_{i1}(\alpha_i) &= \frac{\left[R_i^2(\alpha_i) + R_i'^2(\alpha_i)\right]^{3/2}}{R_i^2(\alpha_i) + 2R_i'^2(\alpha_i) - R_i(\alpha_i)R_i''(\alpha_i)} \\ R_{i2}(\alpha_i) &= \frac{R_i(\alpha_i)sin\alpha_i}{cos(\pi/2 - \alpha_i - \delta_i)}. \end{aligned} \tag{2.34}$$

where, $R_i'(\alpha_i)$ and $R_i''(\alpha_i)$ are the first and second order derivatives of $R_i(\alpha_i)$ with respect to α_i, respectively. For the derivation of the radius of curvature R_{i1}, see [51].

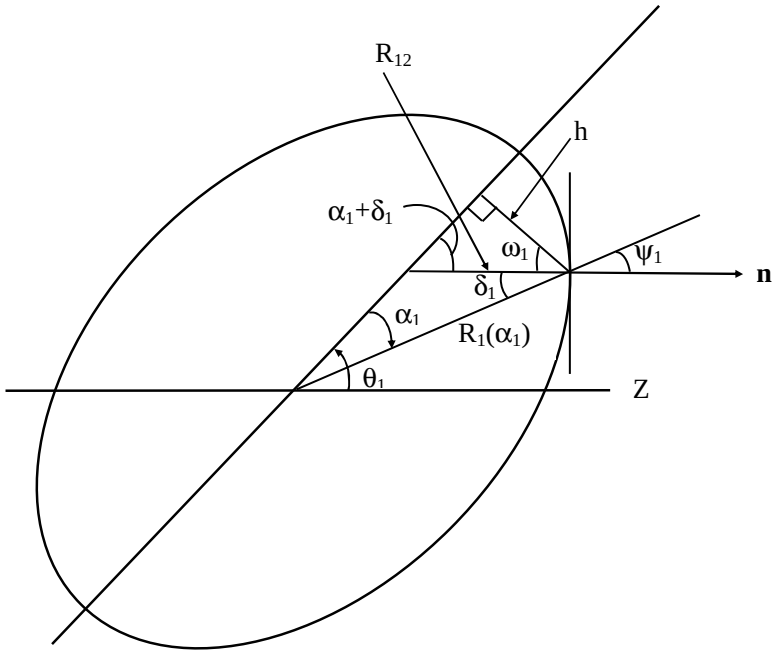

Figure 2.2 An axially symmetric (quadrupole) deformed and oriented nucleus, showing the nuclear radius parameter $R_1(\alpha_1)$ and the geometry associated with the principal radius of curvature $R_{12}(\alpha_1)$.

It follows from Fig. 2.2, and Ref. [52], that $R_{i2} = h/cos\omega_i$, with $h = R_i(\alpha_i)sin\alpha_i$ and $\omega_i = \pi/2 - \alpha_i - \delta_i$. Also, for **n** to be a normal vector

$$tan\delta_i = -\frac{R_i'(\alpha_i)}{R_i(\alpha_i)}. \tag{2.35}$$

Note that $R_{i1}(\alpha_i) = R_{i2}(\alpha_i)$, respectively, for $\alpha_1 = 0^0$ or 180^0 and $\alpha_2 = 180^0$ or 360^0. For deformed, oriented nuclei configuration, the minimum distance s_0 (see Fig. 2.1) in Eq. (2.26) is

$$s_0 = R - X_1 - X_2 \tag{2.36}$$

with the projections X_i along the Z-axis given as

$$\begin{aligned} X_1 &= R_1(\alpha_1)cos(\theta_1 - \alpha_1) \\ X_2 &= R_2(\alpha_2)cos(180 + \theta_2 - \alpha_2) \end{aligned} \tag{2.37}$$

and the minimization conditions on s_0,

$$\frac{\partial s_0}{\partial \alpha_1} = \frac{\partial s_0}{\partial \alpha_2} = 0, \tag{2.38}$$

resulting in

$$\begin{aligned} \tan(\theta_1 - \alpha_1) &= -\frac{R_1'(\alpha_1)}{R_1(\alpha_1)} \\ \tan(180 + \theta_2 - \alpha_2) &= -\frac{R_2'(\alpha_2)}{R_2(\alpha_2)}. \end{aligned} \tag{2.39}$$

Comparing Eqs. (2.35) and (2.39), we get

$$\begin{aligned} \delta_1 &= \theta_1 - \alpha_1 \\ \delta_2 &= 180 + \theta_2 - \alpha_2, \end{aligned} \tag{2.40}$$

to be used in Eq. (2.34). Thus, for the given θ_1 and θ_2, X_1 and X_2 are obtained for the angles α_1 and α_2 satisfying the minimization conditions Eq. (2.39). Note that the conditions Eq. (2.39) refer to perpendiculars (normal vectors) at the points P_1 and P_2. In other words, if the distance s_0 were to be shortest, the perpendicular conditions Eq. (2.39) must be used which would apparently give Eq. (2.37) for X_i.

Eq. (2.31) is valid for zero (touching configuration) and positive values of s_0, but is also used for negative s_0. As the two nuclei overlap ($s_0 < 0$), a crevice is formed and, in an adiabatic approximation, the system adjusts its shape parameters such that the two colliding nuclei form a single indented body in the form of a single hyperboloid of one sheet with a hyperboloidal crevice, as shown in Fig. 2.3(a). For such a necked system, shown in Fig. 2.3(b), following Blocki *et al.* [48], the proximity

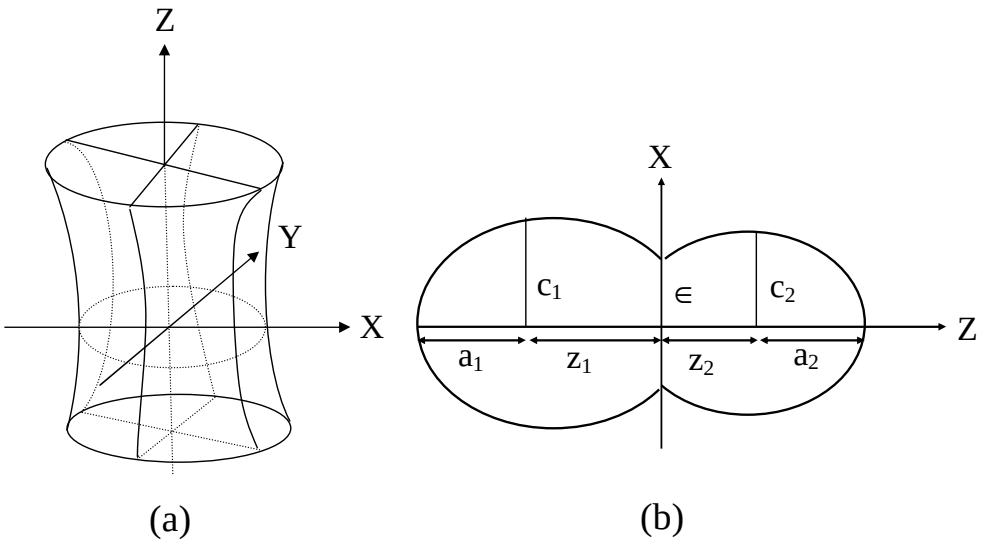

Figure 2.3 (a) Schematic representation of a hyperboloid of revolution in one sheet. (b) Sample nuclear shape formed in two center shell model [38].

potential is obtained by Gupta and collaborators [2, 53] as

$$V_P(s_0) = \pi\gamma b^2 \Phi_1(s_0 = 0) \frac{(c_1^2 + c_2^2 - 2\epsilon^2)}{(z_1^2 + z_2^2)} \tag{2.41}$$

where $\Phi_1(s_0 = 0)$=-2.0306 is the first moment of the universal function Φ at $s_0 = 0$, and c_i, z_i and ϵ are the shape parameters in Fig. 2.3(b). Apparently, for two equal nuclei, $z_1 = z_2$ and $c_1 = c_2$.

2.2.6 The Coulomb potential

Coulomb potential describes the force of repulsion between two interacting nuclei due to their charges. It acts along the line joining the two nuclei. For deformed and oriented interacting nuclei, different authors [50, 54–56] have given different expressions. The Coulomb potential for two interacting hot, deformed and oriented

nuclei is given as [50]:

$$V_c(Z_i,\beta_{\lambda i},\theta_i,T) = \frac{Z_1Z_2e^2}{R(T)} + 3Z_1Z_2e^2\sum_{\lambda,i=1,2}\frac{R_i^{\lambda}(\alpha_i,T)}{(2\lambda+1)R(T)^{\lambda+1}}Y_{\lambda}^{(0)}(\theta_i) \Big[\beta_{\lambda i} + \frac{4}{7}\beta_{\lambda i}^2 Y_{\lambda}^{(0)}(\theta_i)\Big], \quad (2.42)$$

with R_i from Eq. (2.14). $Y_{\lambda}^{(0)}(\theta_i)$ are the spherical harmonics function.

2.2.7 Rotational Energy due to angular momentum

The rotational motion gives an additional energy due to the angular momentum ℓ, defined as

$$V_{\ell}(R,A_i,\beta_{\lambda i},\theta_i,T) = \frac{\hbar^2\ell(\ell+1)}{2I(T)} \quad (2.43)$$

where I is the moment of inertia. $\mu = \frac{A_1A_2}{A_1+A_2}m$ is the the reduced mass with m as the nucleon mass. $I(T)$=I_{NS}=μR^2, is the non-sticking limit of moment of inertia. In the complete sticking limit, the moment of inertia I is given as,

$$I_s(T) = \mu R^2 + \frac{2}{5}A_1mR_1^2(\alpha_1,T) + \frac{2}{5}A_2mR_2^2(\alpha_2,T). \quad (2.44)$$

with R_i from Eq. (2.14). For the relative separation of interest here, we use the sticking limit. It is relevant to mention here that value of angular momentum extracted experimentally, is based on the moment of inertia in non-sticking limit (i.e. $I_{NS} = \mu R^2$) [57]. It means that fragment emission is punctual. In our recent study [16] we find that non-sticking limit is more appropriate for the anisotropy calculations whereas the sticking limit is more appropriate for obtaining the fission cross-sections which consequently results in to large limiting value of angular momentum.

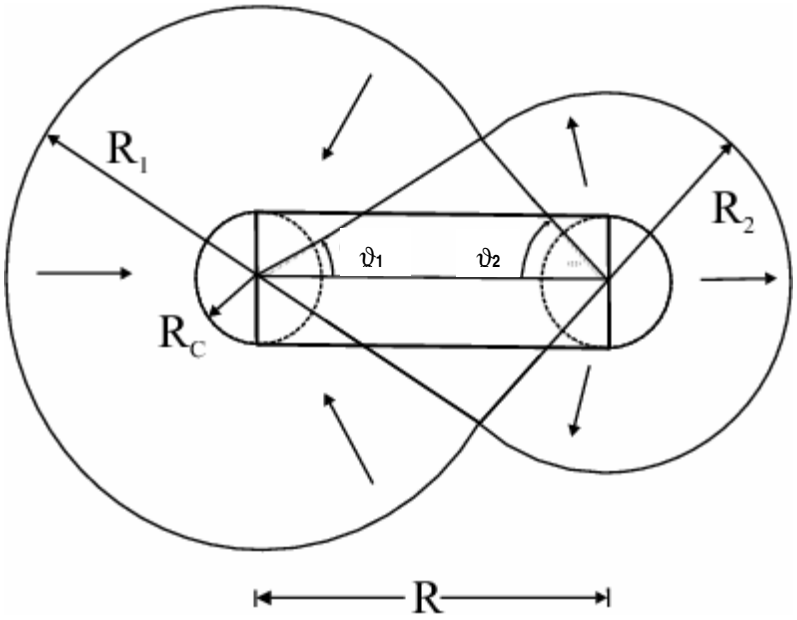

Figure 2.4 The geometry of the classical hydrodynamical model of Kröger and Scheid for calculating the mass parameter $B_{\eta\eta}$.

2.2.8 Classical Hydrodynamical Mass Parameters

The kinetic energy part of the Hamiltonian in Eq. (2.8) enters through the mass parameters. We use here the classical mass parameters of Kröger and Scheid [58]. The model of Kröger and Scheid is based on the hydrodynamical flow, as shown in Fig. 2.4. This model gives a simple analytical expression, whose predictions are shown to compare nicely with the microscopic cranking model calculations. For the $B_{\eta\eta}$ mass we get,

$$B_{\eta\eta} = \frac{AmR^2}{4}\left[\frac{v_t(1+\gamma)}{v_c(1+\delta^2)} - 1\right] \tag{2.45}$$

with

$$\gamma = \frac{R_c}{2R}\left[\frac{1}{1+\cos\vartheta_1}\left(1-\frac{R_c}{R_1}\right) + \frac{1}{1+\cos\vartheta_2}\left(1-\frac{R_c}{R_2}\right)\right] \tag{2.46}$$

$$\delta = \frac{1}{2R}\left[(1-\cos\vartheta_1)(R_1-R_c) + (1-\cos\vartheta_2)(R_2-R_c)\right] \tag{2.47}$$

$$v_c = \pi R_c^2 R \tag{2.48}$$

ϑ_1 and ϑ_2 and geometry of the model are shown in Fig. 2.4. For $\vartheta_1 = \vartheta_2 = 0$, $\delta = 0$ which corresponds to two touching spheres. $R_c(\neq 0)$ is the radius of a cylinder of length R, having a homogeneous flow in it; whose existence is assumed for the mass transfer between the two spherical fragments. We have generalized this expression for deformed nuclei by using the radii R_1 and R_2 for hot deformed nuclei, given by Eq. (2.14).

2.2.9 Solution of the stationary Schrödinger equation and the fragment's preformation probability P_0

Once the Hamiltonian of Eq. (2.7) is established, the Schrödinger equation in mass fragmentation co-ordinate η can be solved. On solving Eq. (2.8) numerically, $|\psi^{\nu}(\eta)|^2$ gives the probability P_0 of finding the mass fragmentation η at a fixed R on the decay path.

$$P_0(A_2) \propto |\psi^{\nu}(A_2)|^2 \tag{2.49}$$

For fission studies like the spontaneous fission and fission through the barrier, the motion in R at the saddle point is adiabatically slow as compared to the η motion. Therefore, the potential is minimized in the neck ε and deformation coordinates β_1 and β_2 at each R and η values. Starting from the nuclear ground state in spontaneous fission or cluster decay, and to have complete adiabatically, only the lowest vibrational state $\nu = 0$ is occupied. Then, the mass (or charge) distribution yield, proportional to the probability $|\psi^{(0)}(\eta)|^2$ (or $|\psi^{(0)}(\eta_Z)|^2$) of finding a certain mass

(or charge) fragmentation η (or η_Z) at a position R on the decay path, when scaled to, say, mass A_2 of one of the fragments ($d\eta = \frac{2}{A}$) is given by:

$$P_0 = |\psi_R^{(0)}(A_2)|^2 \frac{2}{A}\sqrt{B_{\eta\eta}(A_2)}). \tag{2.50}$$

However, if the system is excited or we allow interaction between various degrees of freedom, higher values of ν would also contribute. These enter via the excitation of higher vibrational states, and through the temperature dependent potential V and masses B_{ij}.

The effect of adding temperature on potential V and masses B_{ij} is to reduce the shell effects in them, resulting finally in the liquid drop potential V_{LDM} and smoothed (averaged) masses $\bar{B}_{ij}$ for the systems to be very hot. Apparently, cold fission means taking both the potential V and masses B_{ij} with full shell effects included in them and hot fission means using the V_{LDM} and smoothed (averaged) masses $\bar{B}_{ij}$. The possible consequence of such excitations are included here by assuming a Boltzmann like occupation of excited states

$$|\psi(\eta)|^2 = \sum_{\nu=0}^{\infty} |\psi^{\nu}(\eta)|^2 \exp\left(-\frac{E_\eta^\nu}{T}\right) \tag{2.51}$$

Note that we are dealing here with a directly measurable quantity, the mass (or charge) asymmetry, which works dynamically as mass (or charge) transfer coordinate. Thus, the calculated yields $P_0(A_i)$ (or $P_0(Z_i)$) are directly comparable with experiments. The nuclear shape, once minimized in the neck ε and deformation coordinates β_1 and β_2 at a given R ($\approx R_{saddle}$), remains fixed for both the mass and charge distributions of fission fragments.

For the competing, noncompound, quasi-fission (qf) decay channel, the incoming nuclei keep their identity, and hence the preformation factor P_0=1 for η_i in case of qf.

2.2.10 Penetration Probability P

For R-motion, instead of solving the Schrödinger Eq. (2.9), we use the WKB approximation to calculate the penetration probability P. For each η-value, the potential $V(R)$ for $R \geq R_t$ is calculated by using Eq. (2.12) and for $R < R_t$ it is parameterized simply as a polynomial of degree two in R, so that

$$V(R) = \begin{cases} a_1 R + a_2 R^2 & for \quad R_0 \leq R \leq R_t \\ V_c + V_p + V_\ell & for \quad R \geq R_t \end{cases} \tag{2.52}$$

A typical scattering potential, for ^{226}Ra $\rightarrow ^{212}$Pb+^{14}C is shown in Fig. 2.5, calculated by using Eq. (2.12) for the case of ℓ=0. The path of the penetration and the related quantities are also shown. The deformation parameters $\beta_{\lambda i}$ are taken from the tables of Möller *et al.* [40] with "compact" orientations θ_i^c for "cold elongated" configurations. A compact configuration is one occurring with the minimum interaction radius, and is "cold" or "hot" depending on if the barrier is the lowest or highest [50, 59].

The constants a_i $(i = 1, 2)$ occurring in the polynomial, are determined by using the following boundary conditions.

1. At $R = R_0$, $V(R) = Q$

2. At $R = R_t$, $V(R) = V(R_t)$

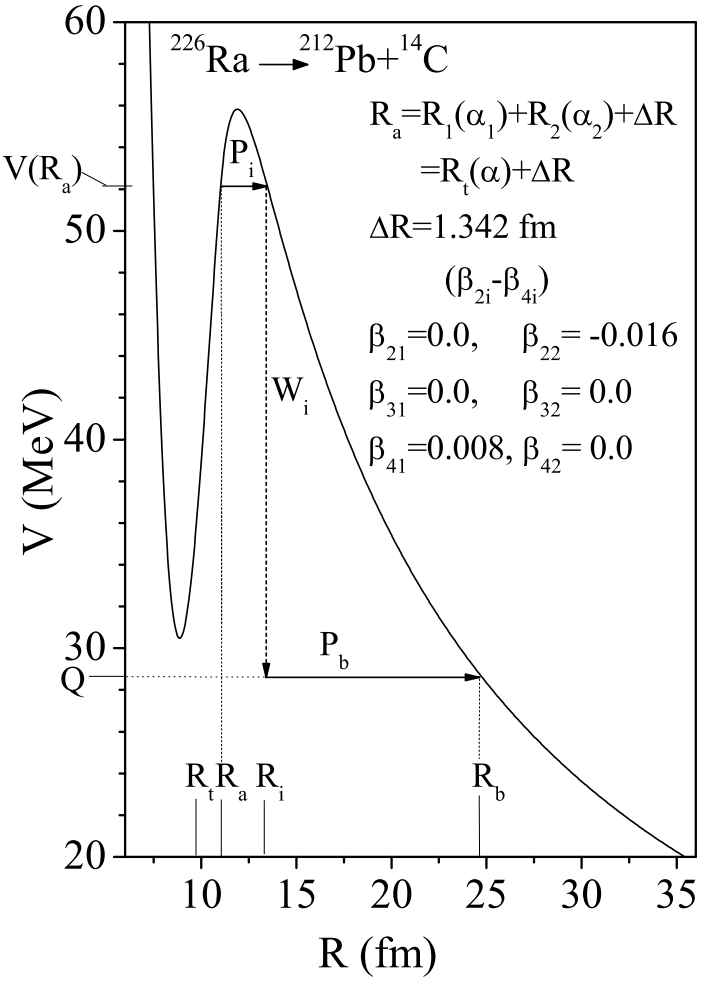

Figure 2.5 The scattering potential for ^{14}C cluster decay of parent nucleus ^{226}Ra, with multipole deformations included up to hexadecapole, and orientation angles θ_i^c of "compact" cold configurations [5].

The first (inner) turning point R_a is chosen at $R_a = R_t + \Delta R$, and the outer turning point is taken at R_b to give the Q-value of the reaction, i.e., $V(R_b) = Q$. This means that the transmission probability P consists of three contributions

1. The penetrability P_i from R_a to R_i,

2. the (inner) de-excitation probability W_i at R_i and

3. the penetrability P_b from R_i to R_b

giving the penetration probability as

$$P = P_i W_i P_b. \tag{2.53}$$

The shifting of first turning point from R_t to R_0 gives the penetrability calculations similar to Shi and Swiatecki [60] for spherical nuclei, which is known not to fit the experimental data without the adjustment of assault frequency.

Following the excitation model of M. Greiner and W. Scheid [61], the de-excitation probability W_i is given as

$$W_i = \exp(-bE_i) \tag{2.54}$$

This means that the de-excitation process is restricted to only a single transition. If the parameter b were allowed to depend on R_i, it should then become a process of multiple de-excitation and proceed as step-like process. For a heavy cluster decay into the excited states of the daughter nucleus, the $b = 0$ is assumed [61], which means

$$W_i = 1, \tag{2.55}$$

so that,

$$P = P_i P_b, \tag{2.56}$$

where P_i and P_b are calculated by using WKB approximation, as

$$P_i = \exp\left[-\frac{2}{\hbar}\int_{R_a}^{R_i}\{2\mu[V(R) - V(R_i)]\}^{1/2}dR\right] \tag{2.57}$$

and

$$P_b = \exp\left[-\frac{2}{\hbar}\int_{R_i}^{R_b}\{2\mu[V(R)-Q]\}^{1/2}dR\right]. \tag{2.58}$$

Here R_a and R_b are, respectively, the first and second turning points. This means that the tunneling begins at $R = R_a$ and terminates at $R = R_b$, with $V(R_b) = Q$-value for ground state decay. The integrals of the Eqs. (2.57) and (2.58) are solved analytically by parameterizing the above calculated potential $V(R)$, as follows:

$$V(R) = \begin{cases} a_1R + a_2R^2, & R_0 \le R \le R_t, \\ V(R_t) + m(R - R_t), & R_t \le R \le R_m, \\ V_B - \frac{1}{2}k(R - R_B)^2, & R_m \le R \le R_h, \\ V(R_h) - c_1\frac{R-R_h}{R}, & R_h \le R \le R_i, \\ V(R_i) - c_2\frac{R-R_i}{R}, & R_i \le R \le R_b, \end{cases} \tag{2.59}$$

For a polynomial of degree higher than two, analytical solutions of WKB integrals could not be obtained. The above equation is true for any inner turning point and hence R_t could be chosen empirically at any point on the polynomial part, as was shown by [2]. Eq. (2.59) means that, the first part of the potential from R_0 to R_t (or R_{emp}) is a polynomial of degree two in R, the second part from R_t to R_m is a straight line of slope 'm', the top part between R_m and R_h being an inverted harmonic oscillator and the rest from R_h to R_i and R_i to R_b are the Coulomb potentials of the type $1/R$. Finally, V_B and R_B give the height and position of the barrier. The analytical solution for the integrals are obtained as

$$\int_{R_b}^{R_t} V(R)dR = \int_{R_m}^{R_t} V(R)dR + \int_{R_h}^{R_m} V(R)dR + \int_{R_i}^{R_h} V(R)dR + \int_{R_b}^{R_i} V(R)dR \tag{2.60}$$

For different components of Eq.(2.56), we have

$$\begin{aligned} P_i &= exp\big[-\frac{2}{\hbar}\sqrt{2\mu}\{\frac{\sqrt{a_2}}{2}[t_1(t_1^2-L^2)^{\frac{1}{2}}-t_2(t_2^2-L^2)^{\frac{1}{2}} \\ &\quad -L^2(cosh^{-1}(\frac{t_1}{L})-cosh^{-1}(\frac{t_2}{L})] \\ &\quad +\frac{2}{3}(\frac{R_m-R_t}{V(R_m)-V(R_t)})[(V(R_m)-V(R_i))^{\frac{3}{2}}-(V(R_t)-V(R_i))^{\frac{3}{2}}] \\ &\quad -\frac{1}{\sqrt{2k}}[V_B-V(R_i)][\Theta_2-\frac{1}{2}sin2\Theta_2-\Theta_1+\frac{1}{2}sin2\Theta_1] \\ &\quad +\sqrt{C_1R_hR_i}[\Theta_3-\frac{1}{2}sin2\Theta_3]\}\big] \end{aligned} \tag{2.61}$$

with

$$a_1=\frac{R_0(Q-V(R_t))}{R_t(R_t-R_0)}, a_2=-\frac{a_1}{R_0}, t_1=R_t-\frac{1}{2}R_0, t_2=R_{emp}-\frac{1}{2}R_0$$

$$L^2=\frac{1}{4}R_0^2+R_t(R_t-R_0)\left[\frac{Q-V(R_i)}{Q-V(R_t)}\right]$$

$$\Theta_1=\cos^{-1}\frac{R_m-R_B}{\sqrt{\alpha}_2}, \Theta_2=\cos^{-1}\frac{R_h-R_B}{\sqrt{\alpha}_2}, \Theta_3=\tan^{-1}\left(\frac{R_i-R_h}{R_h}\right)^{1/2}$$

$$\alpha_2=\frac{2}{k}[V_B-V(R_i)]$$

$$k=\frac{2\{[(V_B-V(R_m)]^{1/2}+[V_B-V(R_h)]^{1/2}\}^2}{(R_m-R_h)^2}, C_1=R_i\frac{(V(R_h)-V(R_i))}{R_i-R_h}$$

and

$$P_b=\exp\left[-\frac{2}{h}\sqrt{2\mu}\sqrt{C_2R_iR_b}\left\{\Theta_4-\frac{1}{2}\sin 2\Theta_4\right\}\right] \tag{2.62}$$

with

$$\Theta_4=tan^{-1}\left[\frac{R_b-R_i}{R_i}\right]^{1/2},$$

$$C_2 = \frac{R_b[V(R_i) - V(R_b)]}{R_b - R_i}.$$

Substituting these values in Eqs. (2.61) and (2.62) we get P_i and P_b. Further substituting P_i and P_b in Eq. (2.56) we get the probability of penetration or the tunneling probability, P.

2.2.11 Assault Frequency ν_0

For the cluster decay studies (the following section), another quantity of interest is the assault frequency ν_0, defined as,

$$\nu_0 = \frac{v}{R_0} = \frac{(2E_2/\mu)^{1/2}}{R_0}, \tag{2.63}$$

where R_0 is the radius of parent nucleus and $E_2 = \frac{1}{2}\mu v^2$ is the kinetic energy of the emitted cluster. Since both the emitted cluster and the daughter nucleus are produced in the ground state, the entire positive Q-value is the total kinetic energy ($Q = E_1 + E_2$) available for the decay process, which is shared between two fragments, such that for the emitted cluster,

$$E_2 = \frac{A_1}{A}Q \tag{2.64}$$

and, $E_1 = Q - E_2$ is the recoil energy of the daughter nucleus.

In the following section, we use Eqs. (2.50), (2.56) and (2.63) for P_0, P and ν_0 for calculating the decay constant and the corresponding half-life for the emitted fragments treated as clusters.

2.3 The Preformed Cluster-decay Model for ground state decay of nuclei

Many theoretical models were advanced [1, 60, 62–65] to understand the process of exotic cluster decay in terms of nuclear α-decay or nuclear fission. These models fall into two main categories. i) Unified fission models (UFM), and ii) Preformed cluster models (PCM). In UFM, the cluster decay is dealt simply as a barrier penetration problem, whereas in PCM, it is considered to happen in two steps as mentioned in Sec. 2.1. The Preformed Cluster-decay Model [1]- [6] has been developed by adopting mainly the Gamow's theory of α-decay. Here, instead of a square well potential, a more realistic nuclear potential, the nuclear proximity potential, is used and also a preformation probability P_0 is associated with each of the emitted cluster. In Gamow's theory of α-decay, the preformation probability for α-decay is assumed to be unity, since only α-cluster is considered to be emitted. In PCM, preformation probability is different for different clusters and it decreases with the increasing size of the cluster. It is relevant to mention here that in PCM the preformation probabilities for all the possible clusters can be obtained, whereas in other model like Blendowske *et al.* [63, 66], the preformation probabilities are calculated for the cluster mass of up to $A = 28$ only. The decay constant in the PCM is defined as,

$$\lambda = \nu_0 P P_0. \tag{2.65}$$

The corresponding half-life is given by:

$$T_{\frac{1}{2}} = \frac{ln2}{\lambda}. \tag{2.66}$$

Here ν_0 is the impinging frequency with which the cluster hits the barrier, P is the penetration probability that gives the probability of penetration of the barrier formed by the outgoing deformed and oriented fragment and P_0 is preformation probability of the cluster giving the probability of the formation of the cluster within the mother nucleus, which is also shown to carry the effects of deformations and orientations of outgoing fragments. For a pure Coulomb potential and $P_0 = 1$, the above Eq. (2.65) will give the Gamow factor 'λ_G'. Thus, the clusters in PCM are considered to be preformed with probability P_0, at a relative separation measured in terms of co-ordinate R before the penetration of the potential barrier.

2.4 The Dynamical Cluster-decay Model (DCM) for hot and rotating compound nucleus

The dynamical cluster decay model (DCM) [7]- [22] for the decay of a hot and rotating nucleus (i.e. angular momentum $\ell \neq 0$ and temperature $T \neq 0$) is a reformulation of the preformed cluster-decay model (PCM) [1]- [6] for ground-state (ℓ=0, T=0) decay of a nucleus in cluster radioactivity (CR) and related phenomena. Thus, like PCM, the DCM is also based on the dynamical (or quantum mechanical) fragmentation theory of cold phenomenon in heavy ion reactions and fission dynamics. Besides the temperature and angular momentum effects in the decay of excited compound nucleus, the deformation and orientation effects of the decay products are also taken care in DCM. The co-ordinates η and R of fragmentation theory in DCM, characterize, respectively,

(i) the nucleon-division (or -exchange) between outgoing fragments, and

(ii) the transfer of kinetic energy of incident channel ($E_{c.m.}$) to internal excitation (total excitation or total kinetic energy, TXE or TKE) of the outgoing channel, since the fixed $R = R_a$, at which the process is calculated, depends on temperature T as well as on η, i.e. $R(T, \eta)$. This energy transfer process follows the relation

$$E^*_{CN} + Q_{out}(T) = TKE(T) + TXE(T). \tag{2.67}$$

The CN excitation energy E^*_{CN} is related to temperature T (in MeV) via Eq.(2.17).

Using the decoupled approximation to R- and η-motions, the DCM defines the decay cross-section, in terms of partial waves, as [7]- [22]

$$\sigma = \sum_{\ell=0}^{\ell_{max}} \sigma_\ell = \frac{\pi}{k^2} \sum_{\ell=0}^{\ell_{max}} (2\ell + 1) P_0 P; \qquad k = \sqrt{\frac{2\mu E_{c.m.}}{\hbar^2}} \tag{2.68}$$

where, P_0, the preformation probability, refers to η-motion and P, the penetrability, to R-motion, discussed in Sec. 2.2.9 and Sec. 2.2.10 respectively. Apparently, for ℓ=0 (s-wave) $\sigma_0 = \frac{\pi}{k^2} P_0 P$, which is an equivalent of decay constant $\lambda = \nu_0 P_0 P$ (or decay half-life $T_{1/2} = ln2/\lambda$) with ν_0 as the barrier assault frequency. In other words, σ_0 and λ differ through a constant only. Thus, like in PCM, here the complex fragments (both light and heavy fragments) are treated as the dynamical collective mass motion of *preformed clusters or fragments* through the barrier. The structure information of the CN enters the model via the preformation probabilities P_0 (also known as the spectroscopic factors) of the fragments given by the solution of stationary Schrödinger equation in η (see Eq. 2.8), at a fixed R=R_a, the first turning point of the penetration path shown in Fig. 2.6 for different ℓ-values.

For the decay of a hot CN, we use the postulate for the first turning point

$$R_a(T) = R_t + \Delta R(\eta, T) \tag{2.69}$$

where

$$R_t = R_1(\alpha_1, T) + R_2(\alpha_1, T) \tag{2.70}$$

$\Delta R(T)$ is the neck-length parameter that assimilates the neck formation effects. This method of introducing a neck length parameter is similar to that used in both the scission-point [67] and saddle-point [68,69] statistical fission models. The R_i are radius vectors given by Eqs.(2.14) and (2.15).

The corresponding potential $V(R_a)$ acts like an effective Q-value, Q_{eff}, for the decay of the hot CN at temperature T, to two exit-channel fragments observed in *ground state* (T=0), defined by

$$\begin{aligned} Q_{eff}(T) &= B(T) - [B_L(T=0) + B_H(T=0)] \\ &= TKE(T) = V(R_a(T)) \end{aligned} \tag{2.71}$$

with B's as the respective binding energies.

The above defined decay of a hot CN into two cold (T=0) fragments, via Eq. (2.71), could apparently be achieved only by emitting some light particle (s) (LPs), like n, p, α, or γ-rays of energy

$$\begin{aligned} E_x &= B(T) - B(0) = Q_{eff}(T) - Q_{out}(T=0) \\ &= TKE(T) - TKE(T=0) \end{aligned} \tag{2.72}$$

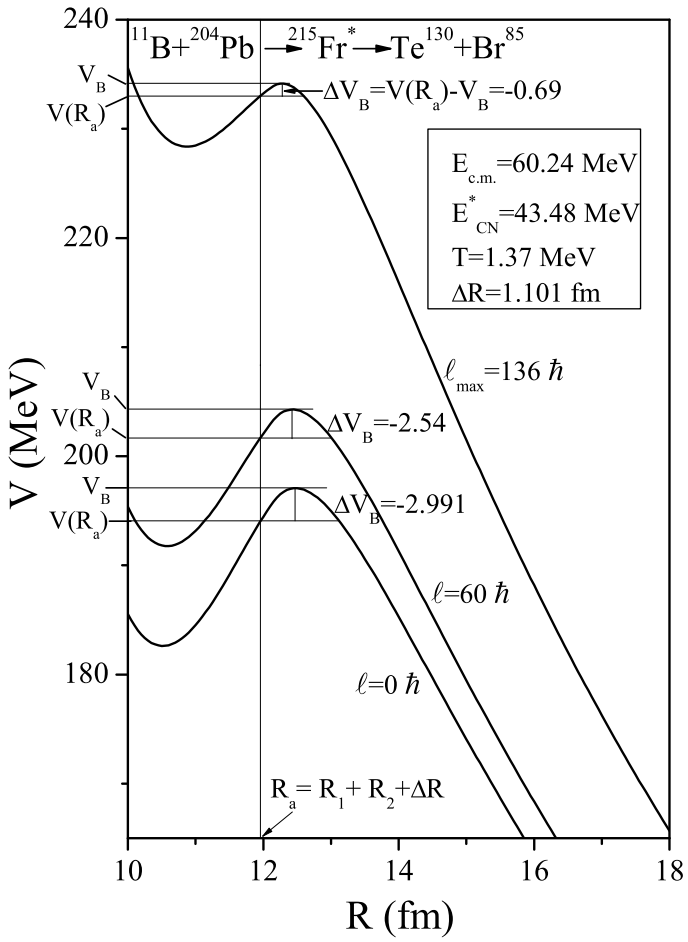

Figure 2.6 The scattering potential for ^{11}B+^{204}Pb→^{215}Fr*→^{130}Te+^{85}Br at $E_{c.m.}$ = 60.24 MeV, calculated at different ℓ-values [16]. The "barrier lowering" $\Delta V_B = V(R_a) - V_B$ for different ℓ's is also shown.

which is zero for the g.s. decay, like for exotic CR. Note that the second equality in Eq. (2.72) is not defined for a negative $Q_{out}(T = 0)$ system since the negative TKE(T=0) has no meaning. Apparently, Eq. (2.72) w.r.t (2.71) suggest that the emission of light-particles starts early in the decay process. The exit channel fragments in Eq. (2.71) are then obtained in the ground-state with TKE(T=0), as can be seen by calculating $E^*_{CN} - E_x$:

$$E^*_{CN} - E_x = |Q_{out}(T)| + TKE(T = 0) + TXE(T). \tag{2.73}$$

The excitation energy TXE(T) (not treated here) is used in, the secondary emission of light particles from the fragments which are otherwise in their ground states with TKE(T=0) in the radial motion. Thus, by defining $Q_{eff}(T)$ as in Eq. (2.71), in this model we treat the LP emission at par with the heavy fragments, called intermediate mass fragments ($IMFs$) emission. Thus, in this model a non-statistical dynamical treatment is attempted for not only the emission of $IMFs$ but also of multiple LPs, understood generally as the statistically evaporated particles in a CN emission. It may be reminded here that the statistical model (CN emission) interpretation of $IMFs$ is not as good as it is for the LP production [67]- [72].

In terms of $Q_{eff}(T)$, the second turning R_b satisfies

$$V(R_a, \ell) = V(R_b, \ell) = Q_{eff}(T, \ell) = TKE(T). \tag{2.74}$$

with the ℓ-dependence of R_a defined by

$$V(R_a, \ell) = Q_{eff}(T, \ell = 0), \tag{2.75}$$

i.e. R_a is the same for all ℓ-values, given by the above equation, and that $V(R_a, \ell)$ acts like an effective Q-value, $Q_{eff}(T, \ell)$, given by the total kinetic energy $TKE(T)$. Then, using Eq. (2.74), $R_b(\ell)$ is given by the ℓ-dependent scattering potentials, at fixed T for coplanar nuclei, as in Eq. (2.12), which is normalized to the exit channel binding energy. This means that all energies are measured $w.r.t$ $B_L(T) + B_H(T)$. The potential illustrated in Fig. 2.6, for ^{215}Fr* $\rightarrow$^{130}Te+^{85}Br, at different ℓ-values, shows that as the ℓ-value increases, the $Q_{eff}(T)$-value (=TKE(T)) increases and hence $V(R_a, \ell)$ increases, since the decay path for all the ℓ-values begins at $R = R_a$.

Finally, the ℓ_{max}-value in Eq. (2.68) is the critical ℓ-value, in terms of the bombarding energy $E_{c.m.}$, the reduced mass μ and the first turning point R_a of the entrance channel η_{in}, given by

$$\ell_c = R_a\sqrt{2\mu[E_{c.m.} - V(R_a, \eta_{in}, \ell = 0)]}/\hbar, \tag{2.76}$$

or, alternatively, it could be fixed for the vanishing of fusion barrier of the incoming channel, called ℓ_{fus}, or else the ℓ-value where the light-particle cross-section $\sigma_{LP}(\ell) \to 0$. This, however, could also be taken as a variable parameter [68, 73].

2.4.1 Concept of "barrier lowering" in DCM

Fusion hindrance phenomenon in coupled channel calculations (ccc) at extreme sub-barrier energies for fusion-evaporation cross-sections in reactions such as ^{58}Ni+^{58}Ni, ^{64}Ni+^{64}Ni and ^{64}Ni+^{100}Mo, and capture cross-sections for ^{48}Ca+^{238}U, ^{244}Pu and ^{248}Cm reactions are one of the topic of current research in Nuclear Physics. DCM also supports the only acceptable explanation for the above said hindrance phenomenon in ccc in terms of the 'modified shape of potential inside the barrier' at sub-barrier energies [74] since the property of 'lowering of barriers' (without modifying the depth of potential pocket) at sub-barrier energies arises in DCM in a simple way via its fitting of the neck-length parameter. The choice of parameter R_a (equivalently, ΔR) for the best fit to the data corresponds to the effects of "barrier lowering" in it for each decay channel, defined for each ℓ as the difference between

$V_B(\ell)$ and $V(R_a, \ell)$, the barrier height and the actually used barrier, as

$$\Delta V_B(\ell) = V(R_a, \ell) - V_B(\ell). \tag{2.77}$$

Note, ΔV_B for each ℓ is defined as a negative quantity as the actual barrier height is effectively lowered, as is also illustrated in Fig. 2.6 for different ℓ values.

2.4.2 Fission fragment anisotropy

The dependence of anisotropy on different quantities can also be explored through DCM within SSPM approach [75]. The fission fragment anisotropy A is related to the total ℓ value (equivalently ℓ_{max}) of the CN, the effective moment-of-inertia I_{eff} of the fissioning nucleus in the transition state (at the saddle point), and the temperature T at the saddle point, as

$$A = 1 + \langle \ell^2 \rangle / 4K_0^2, \tag{2.78}$$

with

$$K_0^2 = T \times I_{eff}/\hbar^2, \tag{2.79}$$

Here I_{eff} is calculated by using the finite-range rotating liquid drop model [76] with T being the temperature of the fissioning nucleus. The value of ℓ_{max} depends on the use of I_S or I_{NS} in the ℓ-dependent potential V_ℓ [Eq. (2.43)]. For fission fragment anisotropies the non-sticking approach is found more suitable contrary to the fitting of evaporation residue and fission cross-sections, where sticking moment of inertia is used [16, 21].

Bibliography

[1] S. S. Malik and R. K. Gupta, Phys. Rev. C **39**, 1992 (1989).

[2] S. Kumar and R. K. Gupta, Phys. Rev. C **55**, 218 (1997).

[3] S. K. Arun, R. K. Gupta, B. B. Singh, S. Kanwar, and M. K. Sharma, Phys. Rev. C **79**, 064616 (2009).

[4] S. K. Arun, R. K. Gupta, S. Kanwar, B. B. Singh, and M. K. Sharma, Phys. Rev. C **80**, 034317 (2009).

[5] G. Sawhney, M. K. Sharma, and R. K. Gupta, Phys. Rev. C **83**, 064610 (2011).

[6] R. Kumar and M. K. Sharma, Phys. Rev. C **85**, 054612 (2012).

[7] R. K. Gupta, R. Kumar, N. K. Dhiman, M. Balasubraniam, W. Scheid, and C. Beck, Phys. Rev. C **68**, 014610 (2003).

[8] M. Balasubraniam, R. Kumar, R. K. Gupta, C. Beck, and W. Scheid, J. Phys. G **29**, 2703 (2003).

[9] R. K. Gupta, M. Balasubraniam, R. Kumar, D. Singh, and C. Beck, Nucl. Phys. A **738**, 479c (2004).

[10] R. K. Gupta, M. Balasubramaniam, R. Kumar, D. Singh, C. Beck, and W. Greiner, Phys. Rev. C **71**, 014601 (2005).

[11] B. B. Singh, M. K. Sharma, R. K. Gupta, and W. Greiner, Int. J. Mod. Phys. E **15**, 699 (2006).

[12] B. B. Singh, M. K. Sharma, and R. K. Gupta, Phys. Rev. C **77**, 054613 (2008).

[13] S. Kanwar, M. K. Sharma, B. B. Singh, R. K. Gupta, and W. Greiner, Int. J. Mod. Phys. E **18**, 1453 (2009).

[14] S. K. Arun, R. Kumar, and R. K. Gupta, J. Phys. G: Nucl. Part. Phys. **36**, 085105 (2009).

[15] M. K. Sharma, S. Kanwar, G. Sawhney, R. K. Gupta, and W. Greiner, J. Phys. G: Nucl. Part. Phys. **38**, 055104 (2011); D. Jain, R. Kumar, M. K. Sharma, and R. K. Gupta, Phys. Rev. C **85**, 024615 (2012).

[16] M. K. Sharma, G. Sawhney, R. K. Gupta, and W. Greiner, J. Phys. G: Nucl. Part. Phys. **38**, 105101 (2011).

[17] M. K. Sharma, G. Sawhney, S. Kanwar, and R. K. Gupta, Mod. Phys. Lett. A **25**, 2022 (2010).

[18] G. Sawhney and M. K. Sharma, Eur. Phys. J. A **48**, 57 (2012).

[19] M. K. Sharma, S. Kanwar, G. Sawhney, and R. K. Gupta, Phys. Rev. C **85**, 064602 (2012).

[20] M. Kaur, R. Kumar, and M. K. Sharma, Phys. Rev. C **85**, 014609 (2012).

[21] M. Kaur and M. K. Sharma, Phys. Rev. C **85**, 054605 (2012).

[22] K. Sandhu, M. K. Sharma, and R. K. Gupta, Phys. Rev. C **85**, 024604 (2012).

[23] J. Maruhn and W. Greiner, Phys. Rev. Lett. **32**, 548 (1974).

[24] R. K. Gupta, W. Scheid, and W. Greiner, Phys. Rev. Lett. **35**, 353 (1975).

[25] A. Săndulescu, R. K. Gupta, W. Scheid, and W. Greiner, Phys. Lett. B **60**, 225 (1976).

[26] R. K. Gupta, A. Săndulescu, and W. Greiner, Phys. Lett. B **67**, 257 (1977); Rev. Roum. Phys. **23**, 51 (1978).

[27] S. Yamaji, W. Scheid, H. J. Fink, and W. Greiner, Z. Phys. A **278**, 69 (1976).

[28] S. Yamaji, W. Scheid, H. J. Fink, and W. Greiner, J. Phys. G: Nucl. Phys. **2**, L189 (1976).

[29] S. Yamaji, K. H. Ziegenhain, H. J. Fink, W. Greiner, and W. Scheid, J. Phys. G: Nucl. Phys. **3**, 1283 (1977).

[30] R. K. Gupta, A. Săndulescu, and W. Greiner, Z. Naturforsch. **32a**, 704 (1977).

[31] R. K. Gupta, C. Pirvulescu, A. Săndulescu, and W. Greiner, Z. Phys. A **283**, 217 (1977); Sovt. J. Nucl. Phys. **28**, 160 (1978).

[32] R. K. Gupta, Z. Physik. A **281**, 159 (1977).

[33] A. Săndulescu, H. J. Lustig, J. Hahn, and W. Greiner, J. Phys. G: Nucl. Phys. **4**, L279 (1978).

[34] H. J. Lustig, J. A. Maruhn, and W. Greiner, J. Phys. G: Nucl. Phys. **6**, L25 (1980).

[35] H. J. Fink, W. Greiner, R. K. Gupta, S. Liran, J.H. Maruhn, W. Scheid, and O. Zohni, in Proceedings of Int. Conf. on Reaction between Complex Nuclei, Nashville, 1974, 21, (Amsterdam: North Holland), pages 2.

[36] R. K. Gupta, IANCAS Bull. (India), **6**, 2 (1990).

[37] V. M. Strutinsky, Nucl. Phys. A **95**, 420 (1967).

[38] R. K. Gupta, N. Singh, and M. Manhas, Phys. Rev. C **70**, 034608 (2004).

[39] G. Audi, A. H. Wapstra and C. Thiboult, Nucl. Phys. A **729**, 337 (2003).

[40] P. Möller, J. R. Nix, W. D. Myers, and W. J. Swiatecki, At. Data Nucl. Data Tables **59**, 185 (1995).

[41] N. J. Davidson, S. S. Hsiao, J. Markram, H. G. Miller, and Y. Tzeng, Nucl. Phys. A **570**, 61c (1994).

[42] P. A. Seeger, Nucl. Phys. **25**, 1 (1961).

[43] S. DeBenedetti, Nuclear Interactions (New York: Wiley) (1964).

[44] W. Myers and W. J. Swiatecki, Nucl. Phys. **81**, 1 (1966).

[45] G. Audi and A. H. Wapstra, Nucl. Phys. A **595**, 4 (1995).

[46] R. K. Gupta, S. Kumar, M. Balasubramaniam, G. Münzenberg, and W. Greiner, J. Phys. G : Nucl. Part. Phys. **28**, 699 (2002).

[47] R. K. Gupta, M. Balasubramaniam, S. Kumar, S. K Patra, G. Münzenberg, and W. Greiner, J. Phys. G : Nucl. Part. Phys. **32**, 565 (2006).

[48] J. Blocki, J. Randrup, W. J. Swiatecki, and C. F. Tsang, Ann. Phys. (NY) **105**, 427 (1977).

[49] Deryagin, Kolloid Z. **69**, 155 (1934).

[50] R. K. Gupta, M. Balasubramaniam, R. Kumar, N. Singh, M. Manhas, and W. Greiner, J. Phys. G: Nucl. Part. Phys. C **31**, 631 (2005).

[51] A. Gray, *Modern Differential Geometry of Curves and Surfaces with Mathematica*, 2nd Edition, CRC Press, Boca Raton, 1997, p.89.

[52] M. Seiwert, W. Greiner, V. Oberacker, and M.J. Rhoades-Brown, Phys. Rev. C **29**, 477 (1984).

[53] N. Malhotra and R. K. Gupta, Phys. Rev. C **31**, 1179 (1985).

[54] M. Münchow, D. Hahn and W. Scheid, Nucl. Phys. A **388**, 381 (1982).

[55] M. J. Rhoades-Brown, V. E. Oberacker, M. Seiwert and W. Greiner, Z. Phys. A **310**, 287 (1983)

[56] C. Y. Wong, Phys. Rev. Lett. **31**, 766 (1973).

[57] S. Kailas (private communication).

[58] H. Kröger and W. Scheid, J. Phys. G **6**, L85 (1980).

[59] R. K. Gupta, M. Manhas, and W. Greiner, Phys. Rev. C **73**, 054307 (2006).

[60] Y. J. Shi and Swiatecki, Phys. Rev. C **54**, 300 (1985).

[61] M. Greiner and W. Scheid, J. Phys. G: Nucl. Phys. **12** L229 (1986).

[62] G. A. Pik-Pichak, Yad. Fiz. **44**, 1421 (1986).

[63] R. Blendowske and H. Walliser, Phys. Rev. Lett. **61**, 1930 (1988).

[64] B. Buck and A. C. Merchant, J. Phys. G: Nucl. Phys. **15**, 615 (1989).

[65] A. Sandulescu, R. K. Gupta, F. Carstoiu, M. Horoi, and W. Greiner, Int. J. Mod. Phys. E **1**, 374 (1992).

[66] R. Blendowske, T. Fliessbach, and H. Walliser, Nucl. Phys. A **464**, 75 (1987).

[67] T. Matsuse, C. Beck, R. Nouicer, and D. Mahboub, Phys. Rev. C **55**, 1380 (1997).

[68] S. J. Sanders, D. G. Kovar, B. B. Back, C. Beck, D. J. Henderson, R. V. F. Janssens, T. F. Wang, and B. D. Wilkins, Phys. Rev. C **40**, 2091 (1989).

[69] S. J. Sanders, Phys. Rev. C **44**, 2676 (1991).

[70] J. Gomez del Campo, R.L. Auble, J.R. Beene, M.L. Halbert, H.J. Kim, A. D'Onofrio, and J.L. Charvet, Phys. Rev. C **43**, 2689 (1991); Phys. Rev. Lett. **61**, 290 (1988).

[71] R. J. Charity, M. A. McMahan, G. J. Wozniak, R. J. McDonald, L. G. Moretto, D. G. Sarantites, L. G. Sobotka, G. Guarino, A. Pantaleo, L. Fiore, A. Gobbi and K. D. Hildenbrand, Nucl. Phys. A **483**, 371 (1988).

[72] C. Beck, R. Nouicer, D. Disdier, G. Duchêne, G. de France, R.M. Freeman, F. Haas, A. Hachem, D. Mahboub, V. Rauch, M. Rousseau, S.J. Sanders, and A. Szanto de Toledo, Phys. Rev. C **63**, 014607 (2001).

[73] S.J. Sanders, D.G. Kovar, B.B. Back, C. Beck, B.K. Dichter, D. Henderson, R.V.F. Janssens, J.G. Keller, S. Kaufman, T.-F. Wang, B. Wilkins, and F. Videbaek, Phys. Rev. Lett. **59**, 2856 (1987).

[74] S. Misicu and H. Esbensen, Phys. Rev. Lett. **96**, 112701 (2006); *ibid* Phys. Rev. C **75**, 034606 (2007).

[75] R. Vandenbosch and J. R. Huizenga, *Nuclear Fission* (Academic: New York) (1973).

[76] A. J. Sierk, Phys. Rev. C **33**, 2039 (1986).

Chapter 3

Decay of odd Fr isotopes formed via different reaction channels

3.1 Introduction

The dynamical cluster-decay model [1]- [9] is used for the first time to study the decay of odd-mass nuclear systems ^{213,215,217}Fr*. The compound nucleus ^{215}Fr* formed in ^{11}B+^{204}Pb and ^{18}O+^{197}Au reaction channels is chosen in reference to [10]. The main aim of this work [3, 4] is to address the question related to entrance channel effects in the decay of ^{215}Fr*, i.e., to identify whether its decay is dependant or independent of its mode of formation. Beside this, the decay paths of compound systems ^{213}Fr* (with $N = 126$) and ^{217}Fr* (with $N = 130$) formed in ^{19}F+^{194,198}Pt reactions [11] are also analysed [6].

The anisotropy data for ^{217}Fr* (with neutron number $N = 130$) is in good accord with the statistical saddle-point model (SSPM [12]) over the entire energy range, except at the highest energy, but for ^{213}Fr* (with $N = 126$) it shows noticeable

deviations from SSPM calculations at a few energies. The authors of [11] associated this deviation with the shell closure property of the CN, whereas in recent work [1] our group considered the possibility of noncompound nucleus (nCN), qf component in the fission cross-section of ^{246}Bk*, a system nearby to ^{213,217}Fr*. Similar observations of anomalous anisotropies for $N = 126$ compound system ^{210}Po* and normal anisotropies for ^{206}Po* with $N = 122$ were also reported earlier [13] in the reactions ^{12}C+^{194,198}Pt.

Here in this chapter, we first concentrate on the entrance channel effects in the decay of ^{215}Fr* formed in ^{11}B+^{204}Pb and ^{18}O+^{197}Au channels in Sec 3.2 and thereafter, we look for the possibilities of the role of magic shells and the qf contribution in σ_{fiss}, if any, for ^{213,217}Fr* nuclei, on the basis of the DCM in Sec. 3.3. Finally, the isotopic behavior of Fr isotopes is studied in Sec. 3.4 and results of our calculations are summarized in Sec. 3.5. This work is published in [3, 6].

3.2 Entrance channel effects and related aspects in decay of ^{215}Fr* nucleus formed in ^{11}B and ^{18}O induced reactions

The entrance channel effects in terms of, say, the presence of noncompound, quasi-fission (qf) component in fission fragment anisotropies and excitation functions of very asymmetric reaction channels forming less fissile systems is still very much an open question [1, 2, 14]. The same question is very recently studied in experiment [10] of the reactions ^{11}B+^{204}Pb and ^{18}O+^{197}Au, leading to the same compound

nucleus (CN) $^{215}Fr^*$, showing no entrance channel effects since, for both the channels, the measured fission fragment anisotropies are found consistent with the statistical saddle point model (SSPM) and fission excitation functions compare nicely with statistical code PACE2 predictions.

The possibility of unexpected presence of qf component has also been explored [14]- [16] for less fissile systems, since it has been known [17] that the systems having entrance channel mass asymmetry α smaller than Bussinaro-Gallone mass asymmetry α_{BG} show preference for pre-equilibrium fission or quasi-fission as compared to the ones with larger α value ($\alpha > \alpha_{BG}$). These observations [17] are based on the variance of measured fission fragment anisotropies w.r.t. their standard saddle point statistical model (SSPM) predictions. In other words, the difference in the measured and SSPM-based anisotropies indicate the possibility of qf, in addition to normal fission process. However, the situation becomes rather complex if the deformed target and/ or projectile combinations are chosen at energies below the Coulomb barrier [18].

Since the experimental data for $^{215}Fr^*$ CN is available [10] on either side of the Coulomb barrier and the mass asymmetry α of the two reaction channels fall on either side of α_{BG}, $^{215}Fr^*$ is a suitable example to study the ff process of a low-energy heavy-ion reaction in the mass region $A \sim$220. The α_{BG} of $^{215}Fr^*$ is 0.855, and those of entrance channel reactions $^{11}B+^{204}Pb$ and $^{18}O+^{197}Au$ are, respectively, α=0.898 and 0.833.

In this work [3], decay of CN $^{215}Fr^*$ formed in two reaction channels $^{11}B+^{204}Pb$ and $^{18}O+^{197}Au$ [10] is studied, over a wide range of $E_{c.m.}$=47-88 MeV, spread on either side of Coulomb barrier (Coulomb barrier is $\approx$57 MeV for $^{11}B+^{204}Pb$ and

≈87 MeV for ^{18}O+^{197}Au channel) using DCM. Although, the chosen compound system as well as the targets and projectiles in the two reaction channels are weakly deformed, and hence the deformation and orientation effects are expected to be small. But such effects in the DCM calculations of ^{215}Fr* system is found to be rather important. Calculations are made for both the excitation functions and fission fragment anisotropies, supporting the SSPM result of non-existence of qf component in both the entrance channels. Note that fission anisotropy, and the reaction channels chosen from Bussinaro-Gallone critical asymmetry point of view, are explored for the first time in the framework of DCM. The calculations and results for both the excitation functions and fission fragment anisotropies are discussed in the following:

Fig. 3.1 shows the calculated fragmentation potentials for the decay of ^{215}Fr*, formed in ^{11}B+^{204}Pb reaction at the compound nucleus excitation energy E^{*}_{CN}=43.48 MeV (T=1.37 MeV), at the extreme ℓ=0 and ℓ_{max} values, using spherical nuclei (Fig. 3.1(a)) and deformation effects of β_{2i} with optimum orientations $\theta_i^{opt.}$ of hot compact configurations (Fig. 3.1(b)), taken from Table 1 of [19]. The optimum orientations θ_i^{opt} are uniquely fixed on the basis of the quadrupole deformation β_{2i} alone of nuclei [19], and are found to hold good [20] for positive but small or any negative value of hexadecapole deformations β_{4i} also included.

We note that in Fig. 3.1, at ℓ=0, the fragmentation potentials are quite similar for spherical and deformed choices of the fragmentations, except for some extra valleys at ^{17}B, ^{26}Mg and ^{27}Al nuclei in the case of deformed considerations. However, these deep valleys, possibly due to the inappropriate β_{2i} values used here [21], get ruled out because of their negligibly small penetrability P across the appropriate

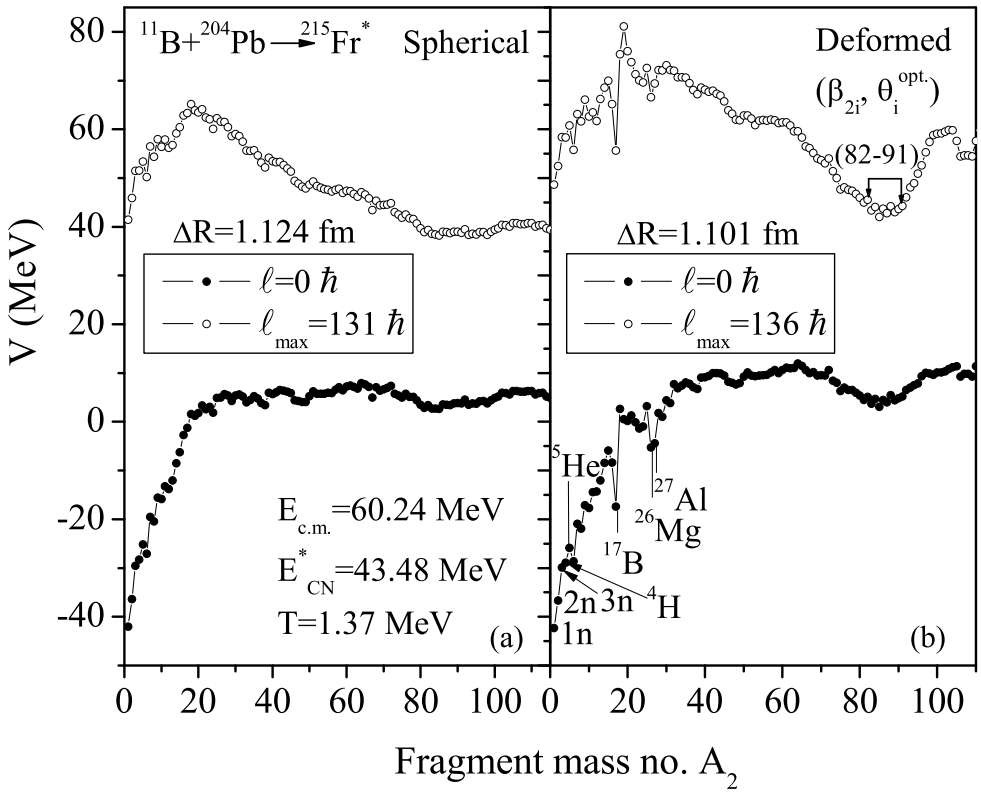

Figure 3.1 Fragmentation potentials as a function of light fragment mass number A_2 for the decay of $^{215}Fr^*$ formed in $^{11}B+^{204}Pb$ reaction channel at a given $E_{c.m.}$, using (a) spherical and (b) deformated considerations. Note that the ΔR and ℓ_{max} values are different, obtained for the best fit to data, which also fixes the fission window for deformed considerations (see the text).

interaction barrier, as discussed later in Fig. 3.3. On the other hand, the structure of potential energy surfaces changes significantly at higher $\ell = \ell_{max}$ values, particularly with the inclusion of deformation and orientation effects. For example, at $\ell = \ell_{max}$, the fission distribution is clearly symmetric for spherical nuclei and becomes rather asymmetric when deformation effects are included (the asymmetric fission window is shown to lie at A_2=82-91). Similarly, the fusion-ERs (LPs: $1n$, $2n$, $3n$ and ^{4}H) are prominent (lower in energy) at ℓ=0, whereas at higher ℓ values the fission fragments start dominating the decay process. These observations clearly indicate that, in addition to the explicit role of angular momentum ℓ, deformations (and

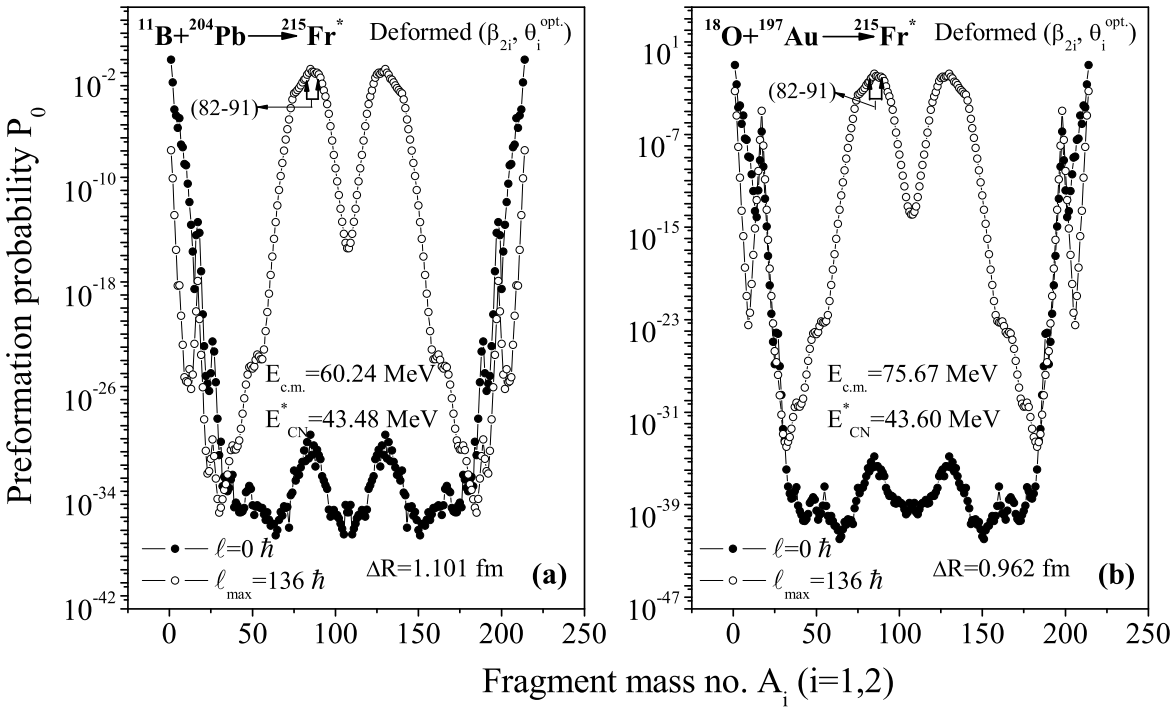

Figure 3.2 Preformation probability P_0 as a function of fragment mass number A_i, i = 1, 2, for the decay of ^{215}Fr*, formed in ^{11}B+^{204}Pb and ^{18}O+^{197}Au reaction channels at about the same E^{*}_{CN}, using deformed considerations (β_2, $\theta_i^{opt.}$).

orientations) also play important role in the decay of ^{215}Fr* nucleus.

Figures 3.2(a) and (b) show the preformation probability P_0 as a function of fragment mass A_i, i = 1, 2, for the decay of ^{215}Fr* formed in ^{11}B+^{204}Pb and ^{18}O+^{197}Au reactions, respectively, calculated at two extreme ℓ-values with deformation and orientation effects included. In order to be able to draw a comparison between the two incoming channels, we have chosen the same CN excitation energy $E^{*}_{CN} \approx$ 43.5 MeV, corresponding to $E_{c.m.}$ = 60.24 MeV and 75.67 MeV, respectively, for ^{11}B+^{204}Pb and ^{18}O+^{197}Au channels. Apparently, $P_0(A_i)$ are nearly independent of the choice of entrance channel, both indicating asymmetric fission mass distributions. For $\ell = \ell_{max}$, the asymmetric maxima lies around A_2=82-91 (plus complementary heavy fragments) for both the channels. Note that the ℓ_{max} value (=136 $\hbar$)

is same for both the reactions. This means that the decay of ^{215}Fr* is independent of mode of its formation, i.e., channel independent, despite the fact that the two entrance-channel mass-asymmetries fall on either side of the α_{BG}.

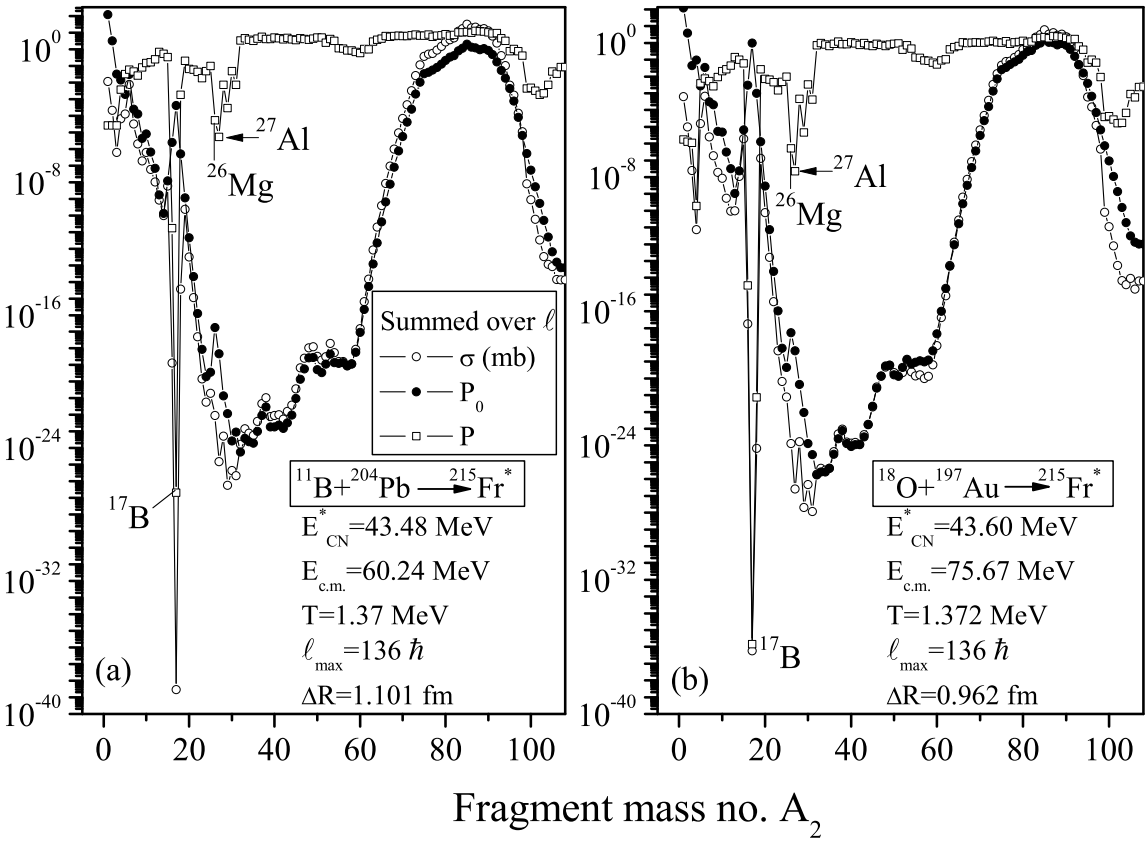

Figure 3.3 The ℓ-summed P_0, P and cross-section σ for the decay of ^{215}Fr* as a function of light fragment mass A_2 for the two entrance channels at different $E_{c.m.}$'s giving nearly the same E^*_{CN}. The ΔR values are also different in the two cases.

Fig. 3.3 shows the ℓ-summed P_0, P and cross-sections σ, as a function of fragment mass number A_2 for ^{11}B+^{204}Pb and ^{18}O+^{197}Au channels at two different $E_{c.m.}$'s (= 60.24 and 75.67 MeV, respectively) forming the CN at about the same E^*_{CN} ($\approx$ 43.5 MeV). It is evident from this figure that (i) σ follows the behavior of P_0, which means that structure effects are contained only in P_0; (ii) P contributes largely to magnitude and has almost no structure effects. The strongly formed fragments ^{17}B,

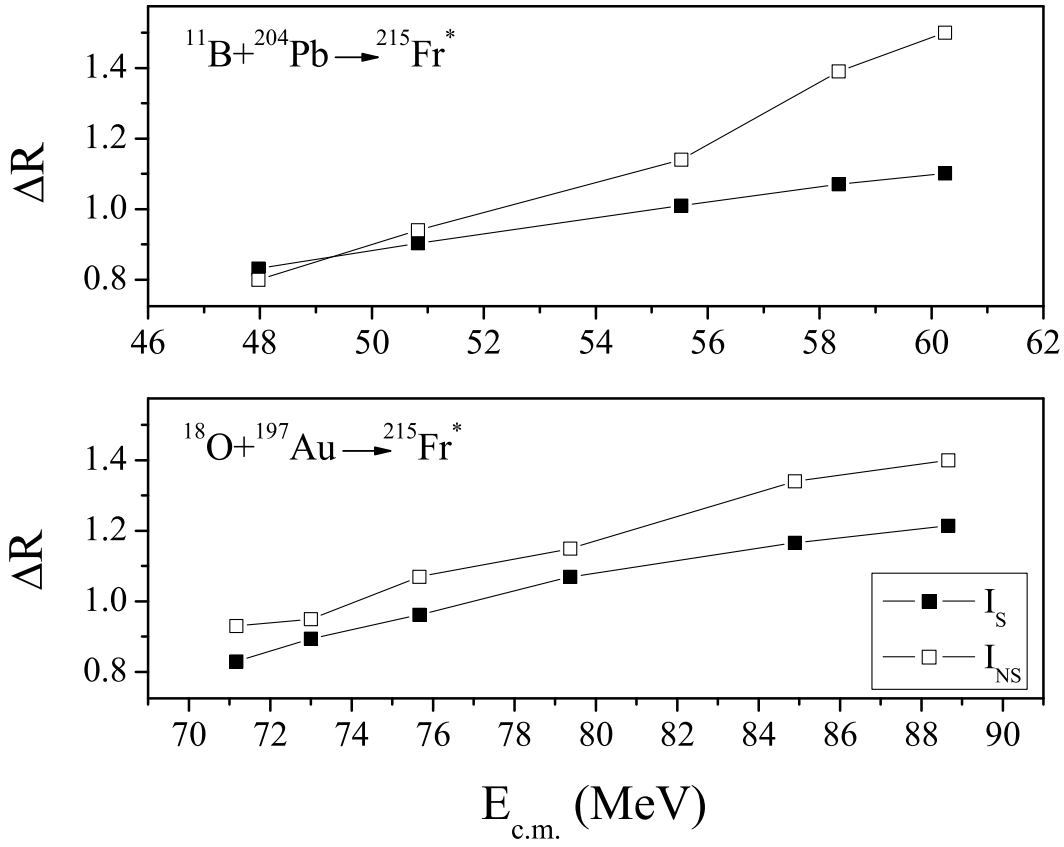

Figure 3.4 The fitted neck-length parameter ΔR as a function of $E_{c.m.}$, for fission decay of CN ^{215}Fr* formed in ^{11}B+^{204}Pb and ^{18}O+^{197}Au reactions, using the sticking (I_S) and non-sticking (I_{NS}) limits of moment-of-inertia.

^{26}Mg and ^{27}Al are shown to have very small P values, and hence their preferential decay (larger P_0 or deeper minima in $V(A_i)$) gets counter balanced by P, which means that the emergence of these valleys should not be taken seriously; (iii) The variation of σ with A_2 is nearly independent of the entrance channel, controlled by the only one parameter of the model, the neck length parameter ΔR, which is shown to be different for the two channels (see Fig. 3.4).

The neck-length parameter ΔR of the model is found to depend strongly on limiting ℓ_{max} value, which in turn depends on the use of sticking or non-sticking limit of moment-of-inertia for angular momentum effects in potential. Note that all

Table 3.1 The DCM calculated decay cross-sections for LPs, σ_{LPs}, and ff, $\sigma_{fission}$, at various $E_{c.m.}$'s for $^{215}Fr^*$ due to the reactions $^{11}B+^{204}Pb$ and $^{18}O + ^{197}Au$, compared with experimental data [10]. Calculations here refer to use of sticking moment-of-inertia I_S.

$E_{c.m.}$ (MeV)	E^*_{CN} (MeV)	T (MeV)	ℓ_{max} ($\hbar$)	ΔR_{fiss} (fm)	σ_{LPs} (mb)	$\sigma_{fission}$ (mb) DCM	Expt.
			$^{11}B+^{204}Pb \rightarrow ^{215}Fr^* \rightarrow A_1 + A_2$				
60.24	43.48	1.37	136	1.101	0.0117	320	319.46
58.34	41.58	1.340	135	1.071	0.00645	233	232.47
55.53	38.77	1.295	136	1.01	0.00217	153	152.47
50.82	34.06	1.2152	135	0.9033	0.000151	39	39.16
47.97	31.21	1.1642	135	0.832	4.99×10^{-6}	7.06	7.24
			$^{18}O+^{197}Au \rightarrow ^{215}Fr^* \rightarrow A_1 + A_2$				
88.66	56.59	1.5602	137	1.214	0.0824	719	718.84
84.89	52.82	1.508	136	1.166	0.0324	372	372.8
79.37	47.30	1.4283	136	1.07	0.00518	169	168.8
75.67	43.60	1.372	136	0.962	0.000641	58.1	58.63
73.00	40.94	1.3303	136	0.894	1.17×10^{-4}	23.4	23.77
71.17	39.10	1.30	137	0.83	6.03×10^{-6}	6.63	6.72

the above calculations are performed for the use of the sticking moment of inertia I_S, which is found of least importance for fission fragment anisotropies (A) calculation. We find that, for fitting the fusion excitation functions (here fission cross-sections), the sticking limit I_S is more appropriate for the proximity potential used here, which, because of its larger magnitude relative to I_{NS}, has consequences for the limiting ℓ_{max} to be much larger, and hence ΔR to be smaller ($\leq$2 fm) in this case. However, for A's, the non-sticking moment of inertia I_{NS} is found more suitable.

For the best-fitted fission cross-sections in Table 3.1 for the use of I_S (and the

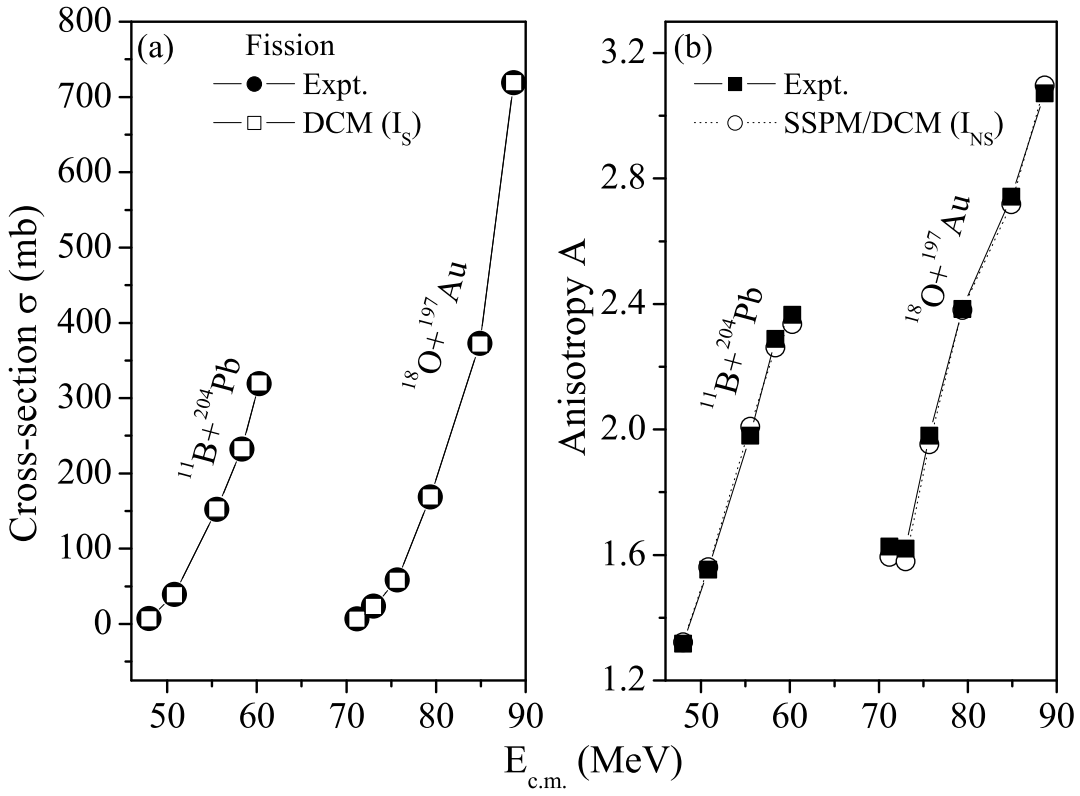

Figure 3.5 (a) The DCM calculated $\sigma_{fission}$ for the decay of compound nucleus ^{215}Fr* formed in ^{11}B+^{204}Pb and ^{18}O+^{197}Au reactions, using the I_S moment-of-inertia, at various $E_{c.m.}$'s, compared with experimental data [10]; (b) The same as for (a) but for the anisotropy A, using the I_{NS} limit of moment-of-inertia.

anisotropy in Table 3.2 for I_{NS}), Fig. 3.4 gives the variation of ΔR with $E_{c.m.}$ for both the reaction channels, plotted for use of I_S (as well as I_{NS}) limit(s). We find that ΔR increases linearly with increase in $E_{c.m.}$, independent of the choice of entrance channel or the limit for moment-of-inertia. Also, we find in Table 3.1 that our calculated contribution of LPs cross-section σ_{LPs} for the case of I_S is negligibly small, $\sim 10^{-2}$ to 10^{-6} mb, much smaller than what is observed for the nearby systems [11]. This means that the decay of ^{215}Fr* is exclusively via the fission process.

Furthermore, in addition to Table 3.1, it is clear from Fig. 3.5(a) that our DCM-calculated fission cross-sections, using I_S, give excellent agreement with data at all

Table 3.2 The DCM calculated fission anisotropies for $^{215}Fr^*$ at various $E_{c.m.}$'s formed in reactions $^{11}B+^{204}Pb$ and $^{18}O+^{197}Au$, compared with experimental data. Calculations here refer to non-sticking moment-of-inertia I_{NS}, and fission cross-sections are also calculated.

$E_{c.m.}$ (MeV)	E^*_{CN} (MeV)	T (MeV)	ℓ_{max} ($\hbar$)	ΔR (fm)	$\sigma_{fission}$ (mb)	Anisotropy A DCM/SSPM	Expt.
			$^{11}B+^{204}Pb\rightarrow^{215}Fr^*$				
60.24	43.48	1.37	25	1.50	9.08×10^{-4}	2.336	2.366
58.34	41.58	1.340	24	1.39	1.47×10^{-4}	2.262	2.289
55.53	38.77	1.295	21	1.14	2.19×10^{-15}	2.009	1.981
50.82	34.06	1.2152	15	0.94	1.92×10^{-30}	1.561	1.554
47.97	31.21	1.1642	11	0.80	5.45×10^{-39}	1.322	1.318
			$^{18}O+^{197}Au\rightarrow^{215}Fr^*$				
88.66	56.59	1.5602	34	1.40	1.95	3.097	3.072
84.89	52.82	1.508	30	1.34	1.12×10^{-1}	2.718	2.742
79.37	47.30	1.4283	26	1.15	8.34×10^{-10}	2.381	2.384
75.67	43.60	1.372	21	1.07	6.26×10^{-18}	1.953	1.980
73.00	40.94	1.3303	16	0.95	1.82×10^{-28}	1.580	1.620
71.17	39.10	1.30	16	0.93	1.07×10^{-29}	1.594	1.627

reported $E_{c.m.}$'s, without invoking any noncompound, quasi-fission contribution in either of the two entrance channels. In other words, our DCM results for fusion excitation functions are in complete accord with experimental observations showing that there is a complete entrance-channel independence of fission cross-sections in the decay of $^{215}Fr^*$ nuclear system.

The fission fragment anisotropies A, are also calculated within the SSPM approach [12], using in Eq. (2.78) the DCM determined ℓ_{max} for I_{NS} limit of moment-of-inertia. The results are presented in Table 3.2, and Fig. 3.5(b), compared with the

available experimental data [10]. The nice comparisons between the DCM-calculated and experimental anisotropies for both the reaction channels further support the fact that entrance channel effects are absent in decay of ^{215}Fr* nucleus formed in ^{11}B+^{204}Pb and ^{18}O+^{197}Au reactions. It is relevant to mention here that, in Table 3.2, the fission cross-sections $\sigma_{fission}$ for ℓ_{max} values determined with in the I_{NS} limit of moment-of-inertia could not be fitted to $\sigma_{fission}$ data.

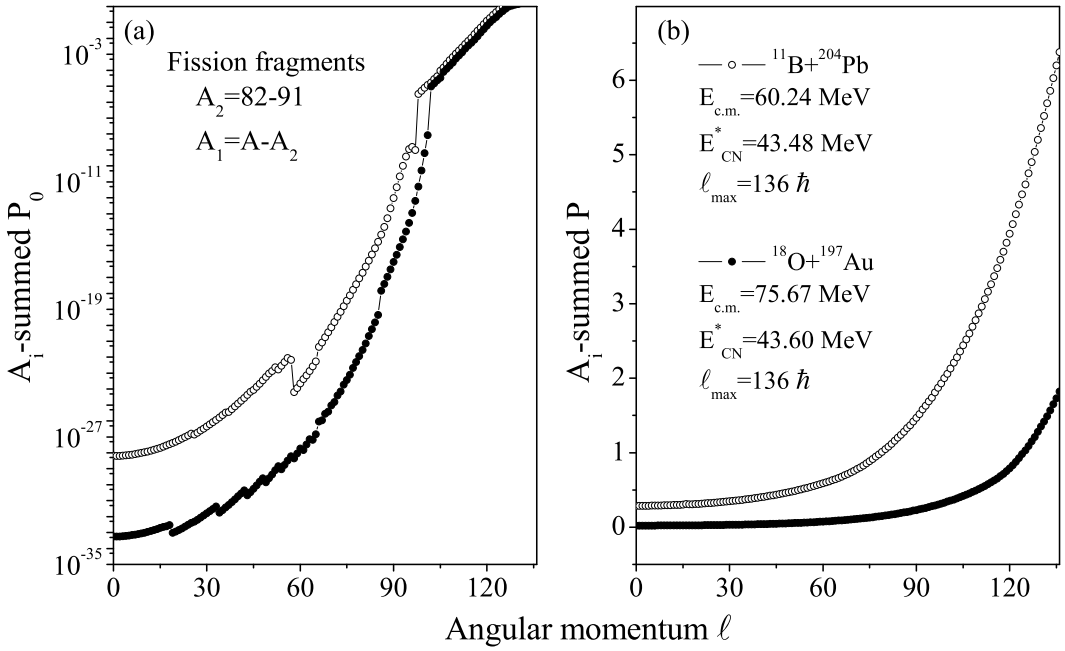

Figure 3.6 The A_i-summed P_0 and P for the fission fragments (A_2=82-91, and complementary heavy fragments, from Fig. 3.1 or Fig. 3.2) plotted as a function of ℓ, for the decay of ^{215}Fr* formed in ^{11}B+^{204}Pb and ^{18}O+^{197}Au channels, at a fixed $E_{c.m.}$ each. The small kinks in $P_0(\ell)$ are possibly due to the numerical instability in the solution of Schrödinger equation.

A comparison of ℓ_{max} values for the two limits of moment-of-inertia in Tables 3.1 and 3.2, shows that anisotropies are best fitted at relatively much smaller ℓ_{max} values, a result of the use of I_{NS} limit, possibly used in the experimental determination of ℓ_{max} values. It may be noted that DCM-based ℓ_{max} values (within non-sticking limit) are larger by 2-7 units as compared to the SSPM estimates for the total ℓ-

values. Apparently, the difference between the DCM ℓ-values and SSPM ℓ-values increases with the increase in c.m. energy. Note that the effective moment-of-inertia I_{eff} at the saddle point in both the cases (DCM and SSPM) is calculated by using the finite-range rotating liquid drop model [22].

Next, in order to investigate the role of angular momentum ℓ in the decay of ^{215}Fr*, we have calculated the A_i-summed P_0 and P as a function of ℓ for the two channels ^{11}B+^{204}Pb and ^{18}O+^{197}Au, presented in Fig. 3.6 for the fission fragments. Evidently, the summed up P_0 and P are quite small up to ℓ=80 $\hbar$, but for ℓ >80 $\hbar$ both P_0 and P rise steeply. This result indicates that the ℓ-window 80$\leq \ell \leq \ell_{max}$ contributes the maximum to the fission of ^{215}Fr*.

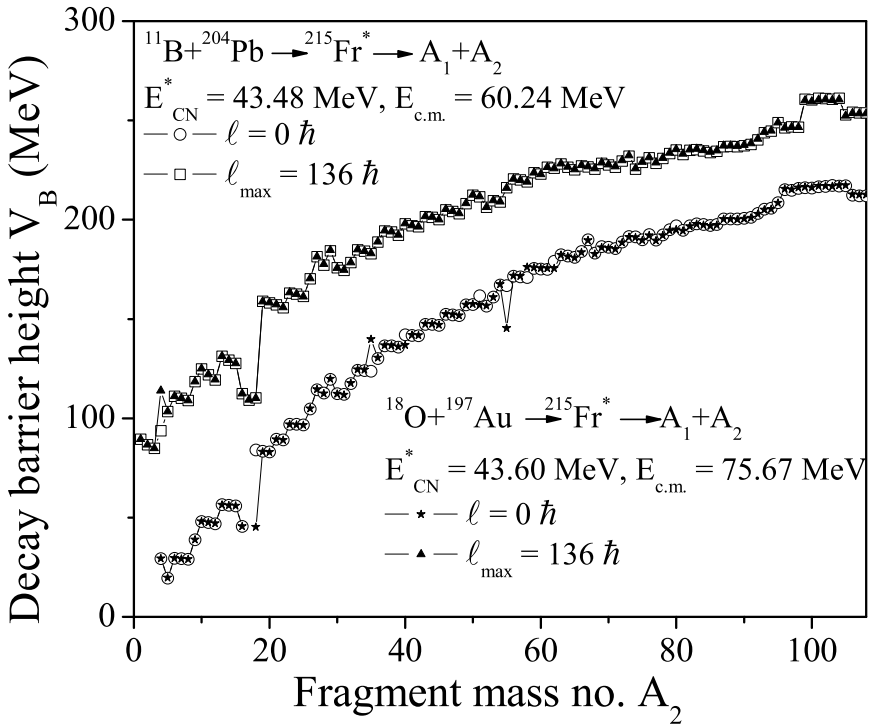

Figure 3.7 The barrier heights V_B as a function of light fragment mass A_2, for the decay of ^{215}Fr*, calculated at two extreme ℓ-values for the two reaction channels at about the same E^*_{CN}.

In Fig. 3.7, we have plotted the barrier heights V_B as a function of light fragment mass A_2 at two different ℓ-values for the decay of ^{215}Fr* formed in ^{11}B+^{204}Pb and ^{18}O+^{197}Au reaction channels at about the same E^*_{CN}. We find that the decay barrier height increases as a function of fragment mass, independent of the entrance channel as well as the angular momentum ℓ-value. This behavior of ℓ-independence is contrary to one for the lighter nuclear system ^{48}Cr (compare with Fig. 7 in [9]), possibly because in lighter nuclei, both LP and IMF (which also include ff region) contribute, whereas in heavy CN, such as ^{215}Fr, only ff contributes. In any case, the entrance-channel independence (together with ℓ-independence) is an interesting result for a weakly fissile CN ^{215}Fr*.

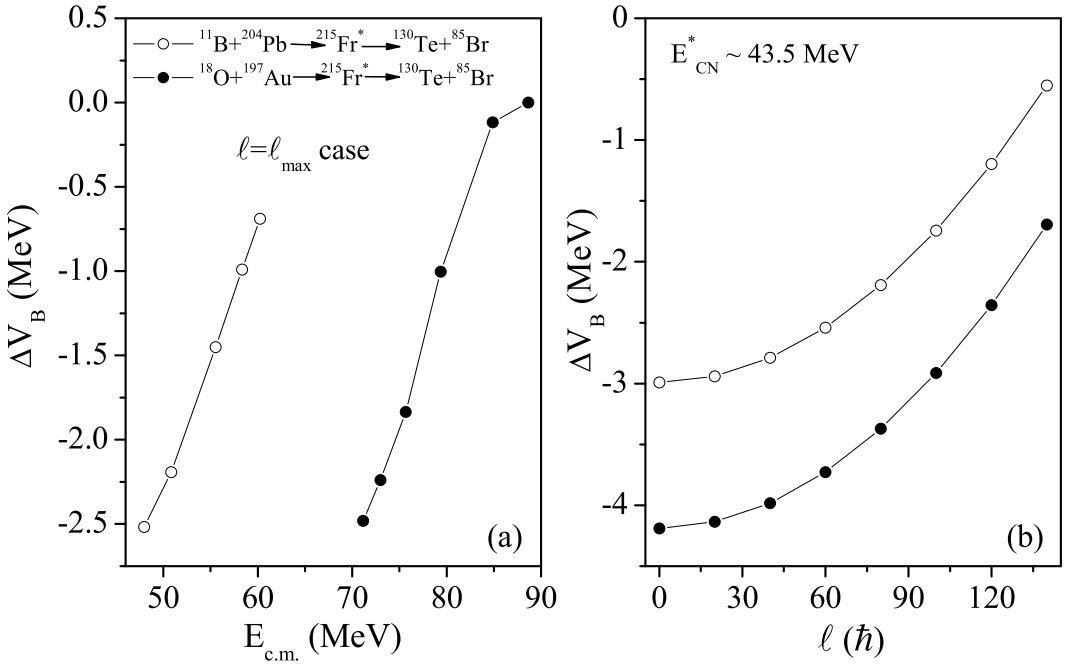

Figure 3.8 (a) Barrier-lowering parameter ΔV_B as a function of $E_{c.m.}$ for the decay of ^{215}Fr*, formed in ^{11}B+^{204}Pb and ^{18}O+^{197}Au reactions, to ^{130}Te+ ^{85}Br fragments, illustrated for the case of $\ell = \ell_{max}$; and (b) the same as for (a) but as a function of ℓ at E^*_{CN} ~43.5 MeV.

Another important result of DCM is its in-built property of 'barrier lowering' at sub barrier energies [8]. Fig. 3.8(a) shows the DCM calculated index of 'barrier lowering' ΔV_B as a function of $E_{c.m.}$ for the decay of ^{215}Fr*, formed in ^{11}B+^{204}Pb and ^{18}O+^{197}Au reactions, respectively, into fragments ^{130}Te+^{85}Br for an illustrative $\ell = \ell_{max}$ case, and the same in Fig. 3.8(b) as a function of ℓ at an illustrative $E^*_{CN} \sim$ 43.5 MeV. Interestingly, ΔV_B increases (effective barrier lowered) as $E_{c.m.}$ decreases to sub-barrier energies, in both the reaction channels. It seems that ΔV_B decreases almost exponentially with the increase in ℓ and is negligibly small at ℓ_{max}.

3.3 Estimation of qf component and possible role of neutron shell closure (N_c=126) in the decay of ^{213,217}Fr* nuclear systems

The decay of ^{213,217}Fr* nuclei are studied at six centre-of-mass (c.m.) energies varying from 80 to 94 MeV, where experimental data are available [11]. The compound nucleus ^{213}Fr* is highly fissile, so σ_{fiss} for ^{213}Fr* is significantly larger over the entire measured energy range, as compared to that for the less fissile ^{217}Fr*. Also, a significant contribution of the evaporation residue cross-section σ_{ER} is measured for both these systems at some of the energies (three of total six), in contrast to ^{215}Fr* where only σ_{fiss} is measured [10].

Calculations are made with in the DCM [6] for spherical, β_2-deformed and (β_2-β_4)-deformed fragments. A comparative study of ^{213}Fr* with ^{210}Po* [13] (both with $N = 126$) is also carried out in order to investigate the role of shell effects. It is

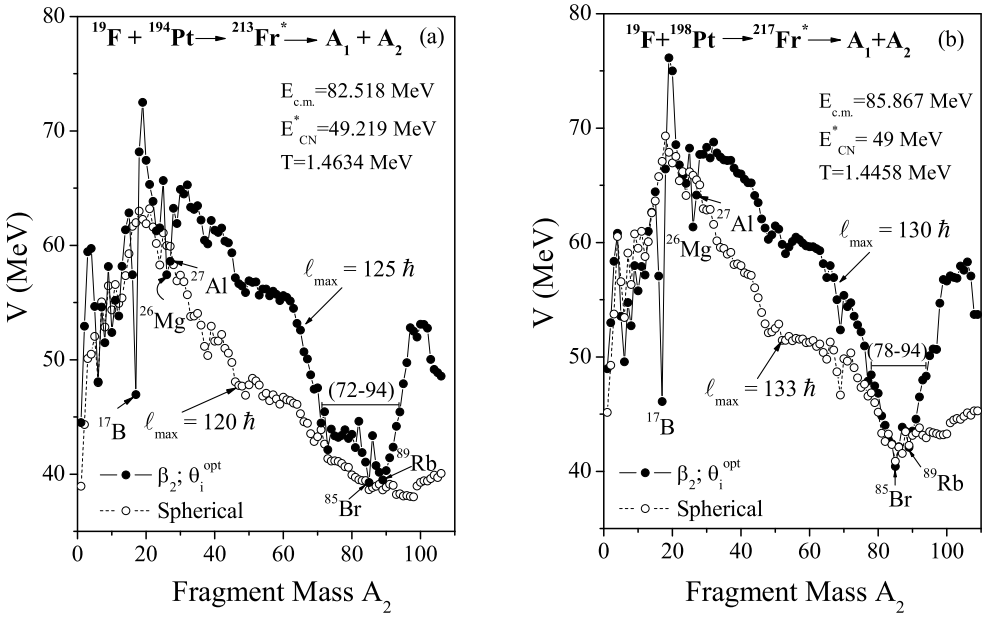

Figure 3.9 Fragmentation potential V as a function of light fragment mass number A_2 for the decay of compound systems ^{213,217}Fr*, plotted for the ℓ_{max}-value, for both cases of spherical and β_2-deformed nuclei.

relevant to mention here that DCM is based on collective fragmentation process and hence can address the role of magic number of decaying fragments alone and not that of the parent nucleus.

Figures 3.9(a) and (b) show the calculated potential energy surfaces, respectively, for the decay of ^{213}Fr* and ^{217}Fr* at one each of the incident c.m. energies such that the two compound nuclei formed have the same excitation energy E^*_{CN} (∼49 MeV). For a comparative investigation, it is essential to keep the excitation energy the same. One may notice in Fig. 3.9 that the fragmentation potentials are relatively smooth for the spherical case, whereas the same show many new deep minima for β_2 deformed fragments. Besides this, with the inclusion of β_2-deformation, the fission distribution pattern changes from near symmetric to asymmetric fragmentation for both the systems. Specifically, there is only one mass region of A_2=72-94 with at

least two strong minima around deformed magic Z_2=36 ($^{85}_{35}$Br and $^{89}_{37}$Rb minima) and spherical magic Z_1=50 ($^{128}_{52}$Te and $^{124}_{50}$Sn nuclei, since Z=87 for Fr) as the asymmetric fission valleys for ^{213}Fr*, whereas the same for ^{217}Fr* refers to A_2=78-94 with double minima again around Z_2=36 (at ^{85}Br and ^{89}Rb) and Z_1=50 (^{132}Te and ^{128}Sn). Note that other deeper minima at A_2=17, 26, 27 do not affect the total cross-section as these get ruled out due to very small penetrability P.

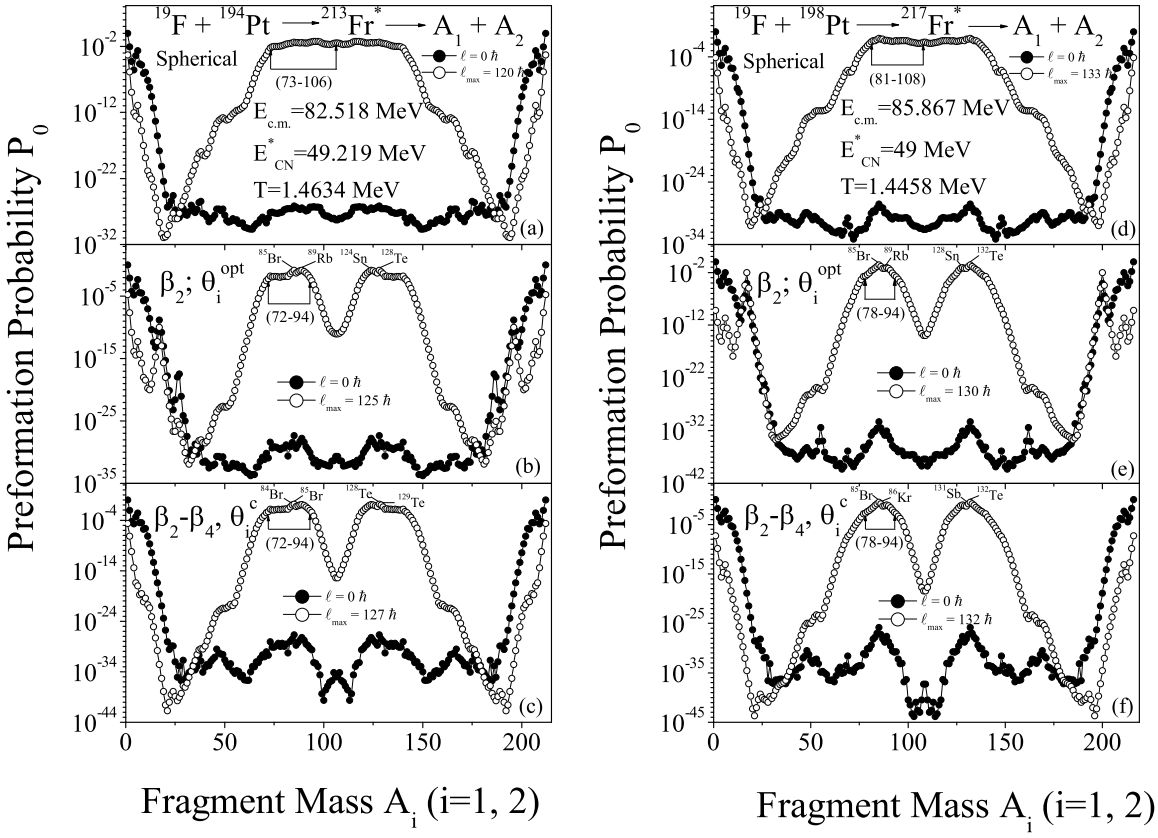

Figure 3.10 Preformation probability P_0 as a function of fragment mass number (A_i), i=1,2, for the decay of ^{213,217}Fr*, taking nuclei to be spherical, β_2 or β_2-β_4 deformed, with appropriate orientation effects.

The above result of fission valleys is more clearly understood in terms of preformation probability P_0, plotted as a function of the fragmentation mass, at two extreme ℓ-values, ℓ=0 and ℓ_{max}, for both the spherical and deformed considera-

tions in Fig. 3.10. For β_2-deformed calculations, the "optimal" orientations θ_i^{opt} are included [19], whereas for higher multipole (β_2-β_4)-deformations "compact" orientations θ_i^c are included [20]. Apparently, we first observe that the distribution yields for ^{213}Fr* and ^{217}Fr* are nearly identical for spherical as well as for β_2-deformed cases, except that they refer to different mass regions. The mass fragmentation is clearly symmetric for the spherical cases and asymmetric for β_2-deformed cases for both ^{213}Fr* and ^{217}Fr* decays.

The asymmetric fragmentation remains intact even if we include higher multipole deformations up to hexadecapole β_4. Comparing ^{213}Fr* with ^{217}Fr*, however, a small difference could be said to be visible in the two distributions for the $\ell = \ell_{max}$ case in that the hump (a shoulder) in mass fragmentation of ^{213}Fr* is somewhat stronger than in the case of ^{217}Fr*. The hump or shoulder in both cases is due to the above noted double minima (at ^{85}Br and ^{89}Rb and the corresponding heavy fragments ^{128,132}Te and ^{124,128}Sn) in the potential energy surfaces of Fig. 3.9(a) and Fig. 3.9(b), i.e., due to the deformed magic shell around $Z_2 = 36$ and spherical magic shell around $Z_1 = 50$.

An exactly similar situation with a pronounced hump due to deformed $Z_2 = 34$ shell and spherical $Z_1 = 50$, like that for ^{213}Fr* ($N = 126$), is depicted in Fig. 3.11 for the ^{210}Po* ($N = 126$) system, calculated at the same value of $E^*_{CN} \sim 49$ MeV with deformation and orientation effects included for the case up to hexadecapole. Note that for the decay of ^{210}Po*, we have fitted only the fission data since the comparative study is confined only to the fission process. Thus, deformation and orientation effects seem to bring out the shell effects in the decay process of two compound systems. It may be relevant to mention here that the authors of Refs. [11, 13]

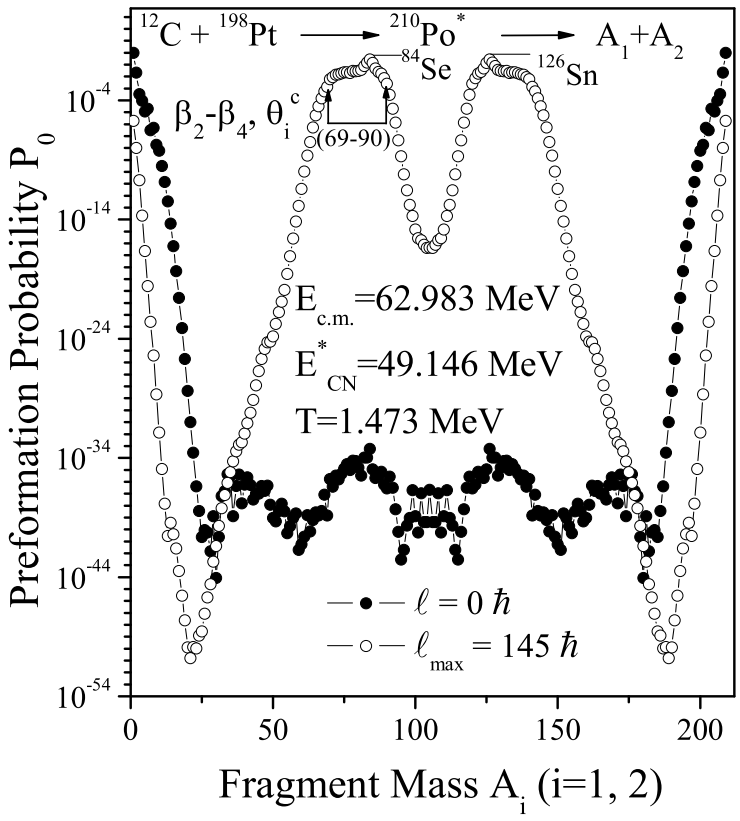

Figure 3.11 Same as for Fig. 3.10, but for ^{210}Po* compound system and for (β_2-β_4)-deformed considerations alone.

associated the anomaly in fission anisotropy of ^{213}Fr* and ^{210}Po* with the neutron shell closure $N = 126$ of the compound systems, which does not seem to play any role in DCM.

The interesting feature of this study is that the experimental data can be fitted with either of the possible choices, i.e., spherical, β_2-alone and β_2-β_4 deformed fragments. The near exact comparison between the calculations and data for both the systems, plotted in Fig. 5 of [6], possibly indicate that the quasi-fission (qf) component in either of the two σ_{fiss} data is rather small or absent. This point is further investigated by evaluating the cross-section for the projectile-like fragment

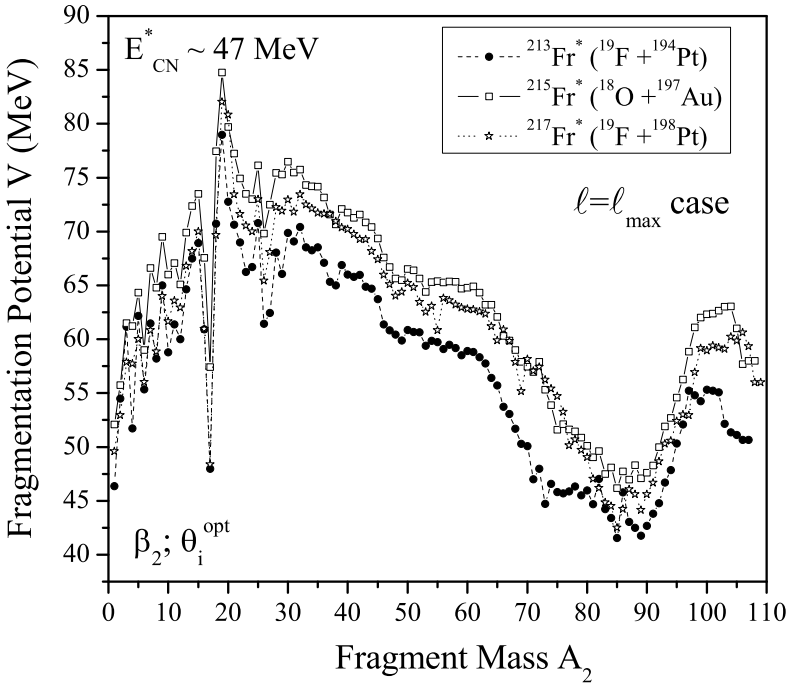

Figure 3.12 Fragmentation potentials V as a function of light fragment mass number A_2 for the compound systems ^{213,215,217}Fr* at $E^*_{CN} \sim 47$ MeV, with the respective ℓ_{max} values of 133, 136, and 137 $\hbar$.

(A_2=19), which gives the qf cross-section of about 4-10% of σ_{fiss} (for the lowest to highest energy) for ^{213}Fr* and 8-10% for ^{217}Fr* at ΔR taken same as for fission cross-section ($P_0 = 1$ for the qf process).

Such a small qf contribution in fission cross-section may arise due to, say, the not-yet-measured, fission mass distributions for these reactions. The above result is in agreement with recent measurements of mass-angle correlations and fission fragment angular distributions in two other reactions ^{16}O+^{197}Au and ^{27}Al+^{186}W forming the same compound system ^{213}Fr* [23], showing no evidence of a nCN, qf component in these decays. One may notice that in the two different experiments [11, 23], the ^{213}Fr* nucleus is formed at a comparable energy range via different projectile-target combinations.

3.4 Effect of adding neutrons

Finally, the isotopic behavior of Fr nuclei is studied by adding two neutrons to ^{213}Fr* nucleus to form ^{215}Fr*, and calculating their fragmentation potentials together with that for ^{217}Fr* compound system, at a comparable $E^*_{CN} \sim 47$ MeV in Fig. 3.12. For β_2-deformed choice, an asymmetric fragmentation is preferred for ^{213,215,217}Fr* nuclei, in agreement with the calculation for ^{215}Fr* alone. It may be relevant to remind here that cross-sections for ^{215}Fr* nucleus formed in ^{18}O+^{197}Au reaction at $E_{c.m} = 79.37$ MeV (equivalently, $E^*_{CN} = 47.30$ MeV) are fitted (refer Fig. 3.5(a) and Table 3.1) in reference to data of [10] and further details on the fitting of ^{213,217}Fr* data can be seen in [6].

3.5 Summary

The dynamical cluster-decay model (DCM) is applied for the first time to study the fusion-fission dynamics of odd mass Fr isotopes. The entrance channel effects in the decay of ^{215}Fr* nucleus, formed in ^{11}B+^{204}Pb and ^{18}O+^{197}Au reactions, is studied and the role of magic shell(s) along with the possibility of quasi-fission component in σ_{fiss} are investigated for compound nuclei ^{213,217}Fr*, by using DCM.

The DCM based results show that the decay of CN ^{215}Fr* is entrance channel independent, in agreement with experimental observations and statistical model (PACE2) calculations. The entrance channel independence of the decay of ^{215}Fr* is concluded by means of (i) angular momentum (ℓ) independence, i.e., ℓ_{max} is observed to be same for the two reaction channels chosen across Bussinaro-Gallone limit α_{BG}, (ii) Decay barrier height increases as a function of fragment mass, independent of the

entrance channel, (iii) The DCM-calculated fission fragment anisotropies are found consistent with experimental data, supporting the entrance channel independence of these reactions. Also, the role of sticking versus non-sticking moment of inertia is found important for the limiting angular momentum ℓ_{max}, since fission anisotropy is found to support the non-sticking limit I_{NS}, whereas the sticking limit I_S is best suited to fusion excitation functions. Interestingly 'barrier lowering' also seems operative in both the reaction channels at sub-barrier energies.

For either of the ^{213,217}Fr* nuclei, the qf component in the fission cross-section, comes out to be nearly absent or small, in agreement with recent experimental observations for some other reactions. The choices of either spherical or quadrupole deformation (β_2) alone and higher multipole deformations (β_2, β_3, β_4) do not account for the $N = 126$ shell closure effect since the DCM is based on collective clusterization method and the magic shell effects of compound nucleus do not come in to play in DCM. Instead, a small hump or shoulder is seen due to deformed shell closure around $Z_2 = 36$ and spherical shell closure around $Z_1 = 50$, which is somewhat more pronounced in case of ^{213}Fr* ($N = 126$) decay as compared to ^{217}Fr* ($N = 130$) mass fragmentation. Besides the deformed shell closure effects, deformations and orientations seem to play a significant role in the decay of Fr isotopes.

Bibliography

[1] B. B. Singh, M. K. Sharma, and R.K. Gupta, Phys. Rev. C **77**, 054613 (2008).

[2] R. K. Gupta and M. Bansal, Int. Rev. Phys. (I.RE.PHY.) **5**, 74 (2011).

[3] M. K. Sharma, G. Sawhney, R. K Gupta, and W. Greiner, J. Phys. G: Nucl. Part. Phys. **38**, 105101 (2011).

[4] M. K. Sharma, G. Sawhney, S. Kanwar, and R. K. Gupta, *Int. Symp. on Forefront of Researches in Exotic Nuclear Structures, Niigata, (Tokamachi, Niigata, Japan, 1-4 March, 2010)* published in Mod. Phys. Lett. A **25**, 2022 (2010).

[5] M. K. Sharma, S. Kanwar, G. Sawhney, R. K. Gupta, and W. Greiner, J. Phys. G: Nucl. Part. Phys. **38**, 055104 (2011).

[6] M. K. Sharma, S. Kanwar, G. Sawhney, and R. K. Gupta, Phys. Rev. C **85**, 064602 (2012).

[7] R. K. Gupta, *Clusters in Nuclei*, Lecture Notes in Physics, **818**, edited by C. Beck, Vol. I (Springer-Verlag, Berlin, Heidelberg, 2010) p. 223.

[8] S. K. Arun, R. Kumar and R. K. Gupta, J. Phys. G: Nucl. Part. Phys. **36**, 085105 (2009).

[9] B. B. Singh, M. K. Sharma, R. K. Gupta, and W. Greiner, Int. J. Mod. Phys E **15**, 699 (2006).

[10] S. Appannababu, S. Mukherjee, N. L. Singh, P. K. Rath, G. K. Kumar, R. G. Thomas, S. Santra, B. K. Nayak, A. Saxena, R. K. Choudhury, K. S. Golda, A. Jhingan, R. Kumar, P. Sugathan, and H. Singh, Phys. Rev. C **80**, 024603 (2009).

[11] K. Mahata, S. Kailas, A. Shrivastava, A. Chatterjee, P. Singh, S. Santra, and B. S. Tomar, Phys. Rev. C **65**, 034613 (2002).

[12] R. Vandenbosch and J. R. Huizenga, *Nuclear Fission* (Academic: New York) (1973).

[13] A. Shrivastava, S. Kailas, A. Chatterjee, A. M. Samant, A. Navin, P. Singh, and B. S. Tomar, Phys. Rev. Lett. **82**, 699 (1999).

[14] R. Tripathi, K. Sudarshan, S. Sodaye, A. V. R. Reddy, K. Mahata, and A. Goswami, Phys. Rev. C **71**, 044616 (2005).

[15] R. Rafiei, R. G. Thomas, D. J. Hinde, M. Dasgupta, C. R. Morton, L. R. Gasques, M. L. Brown, and M. D. Rodriguez, Phys. Rev. C **77**, 024606 (2008).

[16] R. G. Thomas, D. J. Hinde, D. Duniec, F. Zenke, M. Dasgupta, M. L. Brown, M. Evers, L. R. Gasques, M. D. Rodriguez, and A. Diaz-Torres, Phys. Rev. C **77**, 034610 (2008).

[17] V. S. Ramamurthy and S. S. Kapoor, Phys. Rev. Lett **54**, 178 (1985).

[18] R. G. Thomas, R. K. Choudhary, A. K. Mohanty, A. Saxena, and S. S. Kapoor, Phys. Rev. C **67**, 041601 (2003).

[19] R. K. Gupta, M. Balasubramaniam, R. Kumar, N. Singh, M. Manhas, and W. Greiner, J. Phys. G : Nucl. Part. Phys. **31**, 631 (2005).

[20] R. K. Gupta, M. Manhas, and W. Greiner, Phys. Rev. C **73**, 054307 (2006).

[21] P. Möller, J. R. Nix, W. D. Myers, and W. J. Swiatecki, At. Nucl. Data Tables **59**, 185 (1995).

[22] A. J. Sierk, Phys. Rev. C **33**, 2039 (1986).

[23] S. Appannababu, S. Mukherjee, B. K. Nayak, R. G. Thomas, P. Sugathan, A. Jhingan, E. Prasad, D. Negi, N. N. Deshmukh, P. K. Rath, N. L. Singh, and R. K. Choudhury, Phys. Rev. C **83**, 034605 (2011).

Chapter 4

Dynamical decay process of ^{219,220}Ra* formed in the ^{10,11}B + ^{209}Bi reactions

4.1 Introduction

In the previous chapter, the decay of odd-mass nuclear systems ^{213,215,217}Fr* formed in different reaction channels was studied using Dynamical Cluster-Decay Model (DCM). The role of entrance channel effects and magic shells was discussed respectively in reference to ^{215}Fr* and ^{213,217}Fr* systems. Beside this, the presence of a noncompound nucleus, qf component and role of angular momentum along with deformation and orientation effects was also addressed.

In addition to these features, we present here in this chapter, the dynamics of complete fusion (CF) and incomplete fusion (ICF) processes for the nuclide ^{219,220}Ra* populated via fusion of ^{10}B and ^{11}B with ^{209}Bi over a wide range of energies using

DCM. The fission and α-active heavy reaction paths are nicely explored and the application of DCM in reference to ICF and subsequent decay channels is worked out for the first time in this work. In the following a general introduction in reference to the dynamics of ^{10,11}B + ^{209}Bi reaction is described. Sec. 4.2 presents our calculations and results for excitation functions of both CF and ICF processes. Finally, a summary of our results is given in Sec. 4.3.

The interaction of light heavy ion projectiles (Z $\sim$10) and high-Z targets at energies near and above the Coulomb barrier have been a topic of considerable interest [1]- [3]. The formation and decay of an equilibrated compound nucleus is the main reaction mechanism of heavy-ion collisions at low energies. In a conventional picture of fusion the two colliding nuclei fuse, only if they overcome the potential barrier due to their mutual Coulomb and nuclear interactions and subsequently the compound nucleus decays via the emission of light particles resulting in the formation of evaporation residues (ER) or the fissioning of the composite system. However at relatively higher incident energies this picture starts to become invalid, with reactions involving pre-equilibrium particle emission and projectile fragmentation or breakup becoming important. Such processes lead to incomplete fusion or incomplete momentum transfer, indicating that some interesting nuclear aspect can be explored using them.

The complete fusion (CF) is said to occur when entire projectile fuses with target nucleus while, only a part of projectile fuses with target nucleus in case of incomplete fusion (ICF) and unfused fragment continues to move in forward cone with almost projectile velocity. The linear momentum transfer in ICF reactions is less that that in CF reactions. The main motivation of ICF studies is to explore the effect of

various entrance channel parameters, such as projectile energy, mass asymmetry of interacting partners, etc. Such ICF processes can change the nature of the reaction products, as has been investigated in detail for the stable weakly bound nuclei ^{9}Be and ^{6,7}Li [4]. Distinguishing between ICF and CF is quite challenging from both the experimental and the theoretical point of view [5, 6].

The systematics presented by Morgenstern *et al.* [7] have shown that ICF component contributes more towards the total reaction cross-sections for mass asymmetric systems as compared to mass symmetric systems. Reactions involving incomplete mass transfer have been extensively studied in the past few decades and may broadly be divided into three categories, namely, quasi-elastic transfer (QET) reactions, incomplete fusion (ICF) reactions, and deep inelastic collision (DIC). The contribution from noncompound nucleus fission results in deviation of the fission fragment angular anisotropy from statistical theory calculations and equivalent suppression in the formation of evaporation residues is observed.

In this chapter [8], the decay of ^{219,220}Ra* formed in the ^{10,11}B + ^{209}Bi reactions has been studied using DCM [8]- [16] at various centre-of-mass (c.m.) energies above the fusion barrier V_B, ranging from $E_{c.m.}$ = 52.10 - 71.45 MeV [17] (fusion barrier is $\approx$ 48.64 MeV for ^{10}B + ^{209}Bi channel and $\approx$ 48.19 MeV for ^{11}B + ^{209}Bi channel). These nuclei de-excite by fission along with contribution from neutron evaporation which is the dominant evaporation mode. The neutron evaporation channels in this reaction are mainly $1n$, $2n$, $3n$ and $4n$ whose ℓ dependences, $\sigma_{xn}(\ell), x = 1, 2, ...,$ are predicted. In addition to this, excitation functions for other charged particle evaporation residues ^{213}Rn ($\alpha 2n$), ^{212}Rn ($\alpha 3n$), ^{211}Rn ($\alpha 4n$), ^{216}Fr ($p2n$), ^{215}Fr ($p3n$) and ^{214}Fr ($p4n$) produced in ^{10}B + ^{209}Bi reaction are also calculated using DCM.

For a compound nucleus reaction, the complete fusion (CF) cross-section σ_{CF} is defined as the sum of the cross-section due to the emission of light particles (LPs), the so-called evaporation residue σ_{ER} and the fission cross-section due to the decay of compound nucleus into symmetric and/or near symmetric fragments, the so-called fusion-fission component σ_{ff}. In general $\sigma_{CF}(=\sigma_{ER}+\sigma_{Fiss})$ where different compound nucleus reactions show any one of them as a dominant decay mode.

A study of Gasques *et al.* [17] shows fusion suppression in ^{10,11}B + ^{209}Bi reactions. The observed suppression of complete fusion is associated to the low binding energy of ^{10,11}B, which breaks up into charged fragments (e.g. ^{10}B may break up into ^{6}Li and an α-particle, ^{8}Be and ^{2}H, ^{9}Be and proton). This is supported by the significant incomplete fusion cross sections observed for both the reactions [17]. The most favorable breakup threshold energy is 4.512 MeV for ^{10}B and 9.244 MeV for ^{11}B projectiles. An attempt has been made to apply DCM in context of ICF process along with CF process, the details of this work are presented in Sec. 4.2.

4.2 Calculations and discussion

First of all, we study the fissioning path of ^{219,220}Ra* compound systems formed in ^{10,11}B induced reactions and the role of higher multipole deformations (up to hexadecapole) is studied in reference to "optimum" and "compact" orientation approach respectively for β_2 and β_2-β_4 deformations in Sec. 4.2.1. The application of DCM in reference to charged particle evaporation residues formed via successive decay pattern is described in Sec. 4.2.2 and finally the ICF component arising due to the weak binding of projectile is discussed in Sec. 4.2.3.

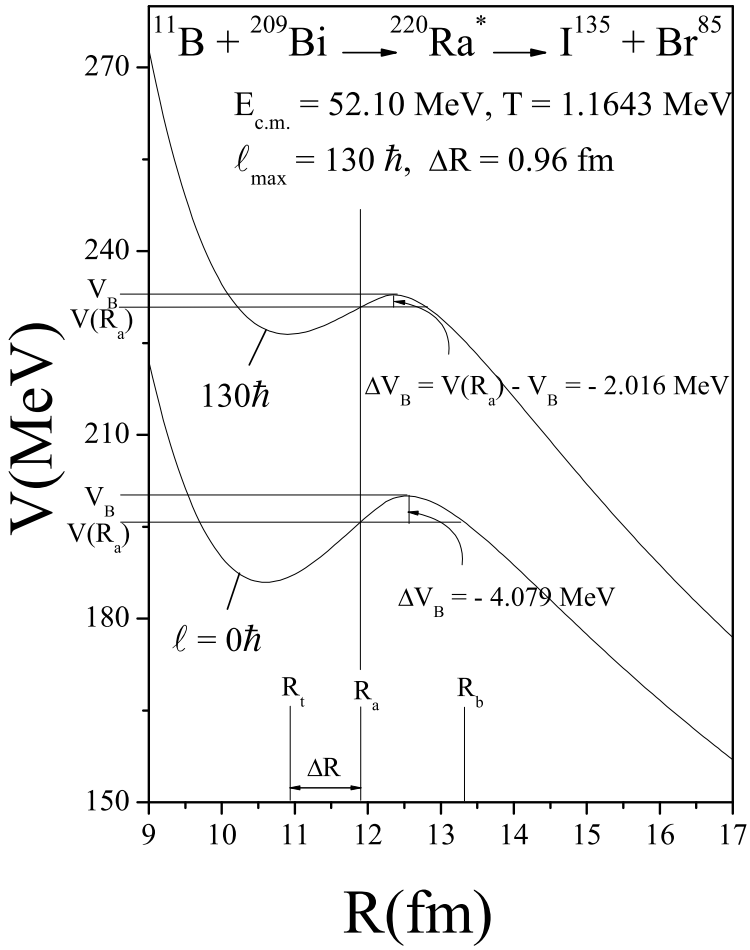

Figure 4.1 The scattering potential $V(R)$ for the decay ^{220}Ra$^*\rightarrow^{135}$I+^{85}Br at $T = 1.1643$ MeV at different ℓ-values. The definition of "barrier lowering" $\Delta V_B = V(R_a) - V_B$ is also shown in this figure for both $\ell = 0$ and ℓ_{max}-values.

4.2.1 Role of deformations in fission excitation functions and estimation of ER cross-sections

Fig. 4.1 shows the scattering potential for $^{220}Ra^*\rightarrow^{135}I + ^{85}Br$ at temperature T = 1.1643 MeV and different ℓ-values i.e ℓ=0 and ℓ_{max}. Here R_a is the first turning point of the penetration path, used for calculating the penetrability P. The compound nucleus temperature T (in MeV) is given by Eq. (2.17) with level density parameter taken as $a = A/9$. Depending on mass of compound nucleus and related reaction

conditions, different values of level density parameter are used, but in the framework of DCM we generally use $a = A/9$ for heavy compound systems and $a = A/10$ for superheavy ones.

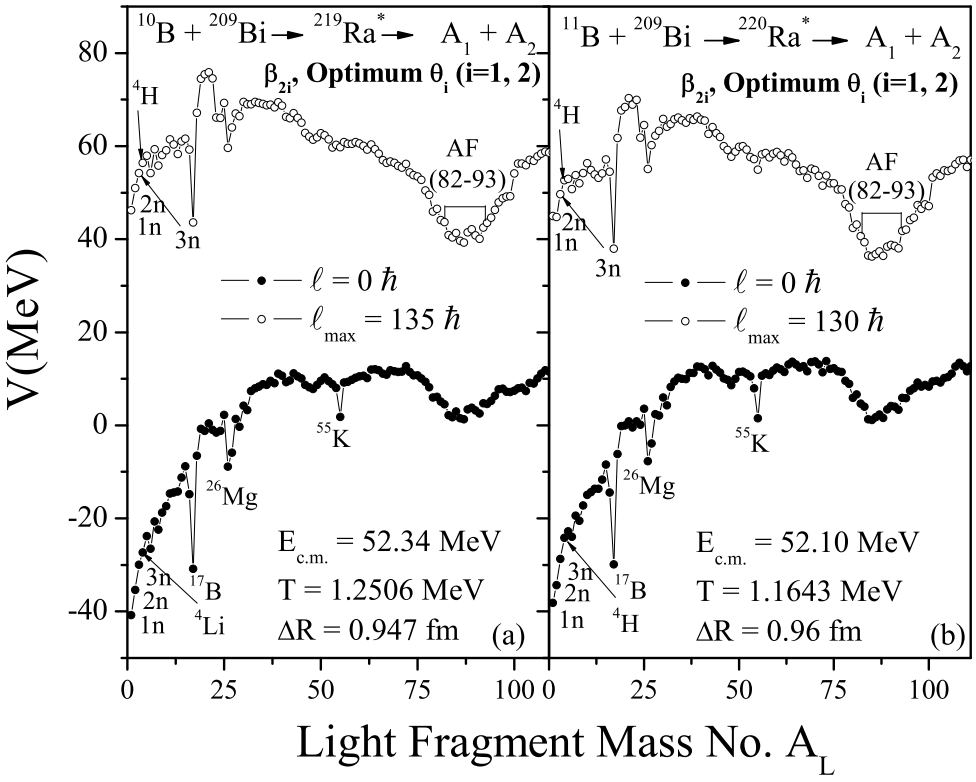

Figure 4.2 Fragmentation potential as a function of light fragment mass no. (A_L), for the decay of ^{219}Ra* and ^{220}Ra*, formed in ^{10}B+^{209}Bi and ^{11}B+^{209}Bi reactions at about same $E_{c.m.} \sim 52$ MeV, using deformed considerations (β_2, $\theta_i^{opt.}$)

Fig. 4.2 illustrates the fragmentation potentials $V(A)$ minimized in charge coordinate η_Z, respectively for the decay of ^{219}Ra* and ^{220}Ra* at the two extreme ℓ=0 and ℓ_{max} values at comparable centre of mass energy $E_{c.m.} \sim 52$ MeV, using β_2-deformations with "optimum" orientation approach. The calculations are made for different neck length parameters ΔR, chosen to fit the respective experimental data on fission cross-sections. It is clearly evident from Fig. 4.2 that the evaporation residue (ER) contribution is most prominent at ℓ=0 whereas the contribution

of fission fragments in the asymmetric fission channel (AF) (in this case) starts dominating at ℓ_{max}. It may be worth mentioning that the fission fragments are not identified in [17] and DCM favors asymmetric fission distribution.

Interestingly the characteristics of the emitted LPs (the ER) change with the addition of neutron i.e. with the increase of the N/Z ratio of CN, the minima at ^{4}Li changes to ^{4}H, though there is no noticeable change in the structure of $V(A_2)$ in going from ^{219}Ra to ^{220}Ra system. The deeper minima at A_2=17, 26, 55 arise possibly due to the improper extrapolated deformations [18], which otherwise do not affect the total cross-section as they get ruled out due to very small penetrability P not shown here (see, e.g., similar results in Refs. [10, 11]).

The fact that the AF fission pattern arises due to the inclusion of deformations and orientations, is evident from Fig. 4.3 where the results of an equivalent spherical calculation in Fig. 4.3(a) are compared with deformation included calculations in Figs. 4.3(b) and 4.3(c). Fig. 4.3 shows the preformation probability P_0 for the decay of ^{220}Ra* formed in ^{11}B + ^{209}Bi reaction at $E_{c.m.}$ = 52.10 MeV, calculated by solving the stationary Schrödinger equation in η for the fragmentation potential shown in Fig. 4.2 at ℓ=0 and ℓ_{max} values for both the spherical as well as deformed considerations. The calculations are done for deformed fragments using quadrupole (β_2) deformations having "optimum" orientation θ_i^{opt} taken from Table 1 of [15] and higher-multipole deformations (β_2-β_4) having compact orientations θ_i^c of hot configurations [16]. The preformation probability P_0 of the fragments (before tunneling through the barrier) accounts for the structure effects of the compound nuclear system. It has been shown explicitly in Fig. 4.3 that the inclusion of deformations and orientations effects of the decaying fragments changes the relative preforma-

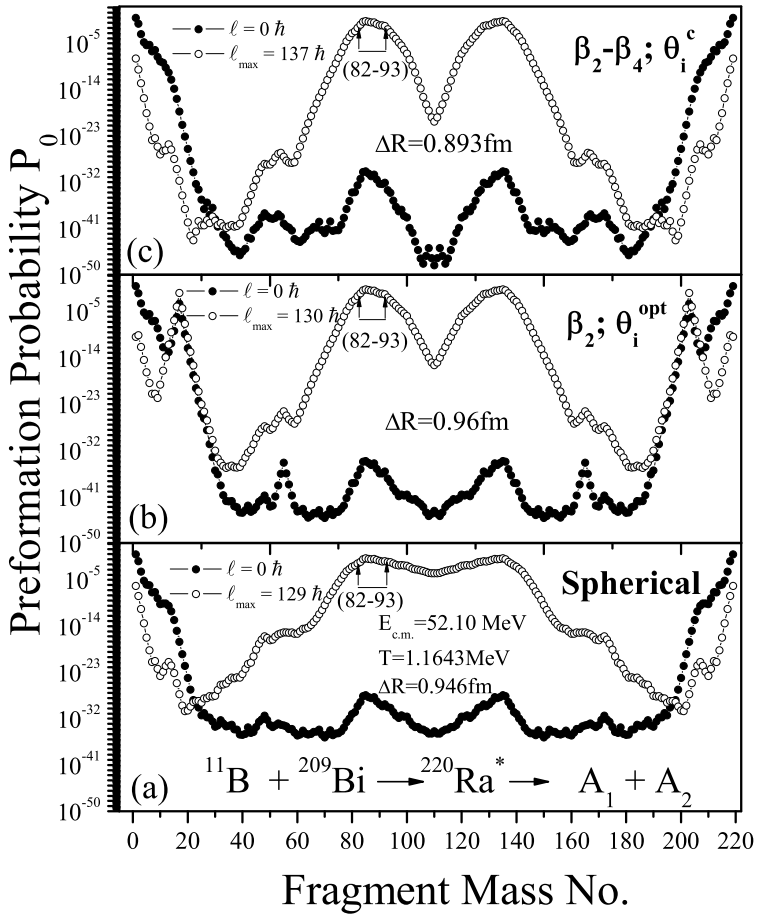

Figure 4.3 Preformation probability P_0 as a function of fragment mass number, for the decay of compound system ^{220}Ra*, plotted for $\ell = 0$ and ℓ_{max}-values, for spherical and deformed nuclei.

tion probability P_0 quite significantly, and hence, equivalently, the potential energy surface (PES). We find that the fission distribution pattern changes from relatively symmetric to asymmetric fragmentation with the inclusion of quadrupole (β_2) as well as higher multipole deformations (β_2-β_4).

Although symmetric fragments contribute more for spherical fragmentation process as compared to that for β_2 or β_2-β_4 deformed case, the fragments in the range A_2 = 82-93 (plus complementary heavy fragments) seem to be the prominent con-

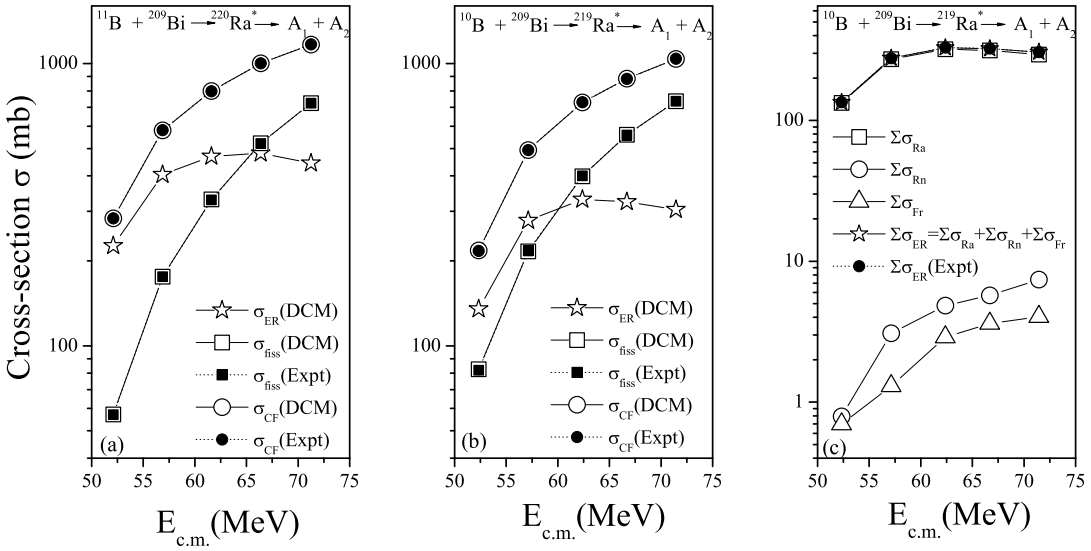

Figure 4.4 Comparison of the experimental fission σ_{fiss} and the complete fusion cross-section, σ_{CF}, with calculations using DCM for (a) ^{11}B + ^{209}Bi and (b)^{10}B + ^{209}Bi reactions. Panel (c) shows the DCM-calculated individual evaporation residue cross-section produced through xn, αxn and pxn emission channels in the decay of ^{219}Ra* compared with experimental total ER cross-section.

tributors toward fission cross-sections for all the chosen fragmentation paths. However, the mass distribution at $\ell = \ell_{max}$ remains almost same when one goes from quadrupole deformed (β_2) to hexadecapole (β_2-β_4) deformed system; the same is not true for ℓ=0 case. At ℓ=0, one may see significant change in PES for β_2 and β_2-β_4 choices. Such variations could be of interest to investigate the ground state decays and nuclear structure effects related to Ra isotopes. An interesting feature of the present study is that the experimental data on fission cross-section could be fitted with spherical as well as with β_2 alone and β_2-β_4 deformed choice of fragmentation, which in turn, provide an unique opportunity to comment on the conclusive role of deformations on the decay path of ^{219,220}Ra* nuclei formed in ^{10,11}B induced reactions over a wide range of incident energies.

Fig. 4.4 (panels (a) and (b)) and Table 4.1 show the comparison of DCM calcu-

Table 4.1 The decay cross-sections for evaporation residues, fission, and complete fusion calculated using DCM at different $E_{c.m.}$'s for the ^{10,11}B + ^{209}Bi reactions forming ^{219,220}Ra* compound systems, compared with experimental data [17]. Here σ_{CF}=σ_{ER}+σ_{fiss}.

$E_{c.m.}$	T	ℓ_{max}	ΔR_{ER}	σ_{ER}	ℓ_{max}	ΔR_{fiss}	$\sigma_{fission}$(mb)		σ_{CF}(mb)	
(MeV)	(MeV)	($\hbar$)	(fm)	(mb)	($\hbar$)	(fm)	DCM	Expt.	DCM	Expt.
^{10}B+^{209}Bi$\rightarrow^{219}$Ra$^* \rightarrow A_1 + A_2$										
52.34	1.2506	128	1.792	135	135	0.947	82.7	82 ± 1	217.7	217 ± 3
57.13	1.3282	126	1.883	278	136	1.033	216	217 ± 2	494	494 ± 5
62.38	1.4082	126	1.914	330	136	1.117	399	400 ± 4	729	730 ± 8
66.68	1.4705	129	1.894	324	138	1.1532	560	559 ± 6	884	883 ± 9
71.45	1.5366	128	1.911	304	137	1.1784	735	735 ± 7	1039	1040 ± 9
^{11}B+^{209}Bi$\rightarrow^{220}$Ra$^* \rightarrow A_1 + A_2$										
52.10	1.1643	118	1.92	226	130	0.96	57.2	57 ± 1	283.2	283 ± 7
56.88	1.2468	118	2.002	404	130	1.036	176	176 ± 2	580	581 ± 7
61.61	1.3233	123	1.970	469	133	1.111	330	329 ± 3	799	798 ± 7
66.38	1.3962	119	2.037	481	130	1.175	522	521 ± 5	1003	1003 ± 9
71.25	1.4668	120	2.029	444	131	1.1958	724	724 ± 7	1168	1169 ± 10

lations, based on β_2 deformed considerations, with experimental data [17] for σ_{fiss} and σ_{CF} of ^{219}Ra* and ^{220}Ra* compound systems. Fig. 4.4(c) is discussed later in section Sec. 4.2.2. The term CF refers to complete fusion and is defined as the sum of light particle (LPs) or evaporation residue cross-section σ_{ER} and the fission cross-section σ_{fiss} (due to the contribution from asymmetric fragments in present case) from the decay of the compound nucleus. Thus the contribution of ER can be obtained from the complete fusion cross-section, as

$$\sigma_{ER} = \sigma_{CF}^{Expt} - \sigma_{fiss}^{Expt}$$

Note that the R_a (equivalently, ΔR) values are different for the fission and ER process and they are chosen in reference to σ_{fiss} and $\sigma_{ER} = (\sigma_{CF}^{Expt} - \sigma_{fiss}^{Expt})$ data.

We notice from Fig. 4.4 and Table 4.1 that for both the compound systems we get an almost exact fit with the experimental data for fission as well as complete fusion cross-sections, using the quadrupole deformations (β_2) and "optimum" orientations θ^{opt} in DCM. It may be noted that the contribution of IMFs in the range A_2 =15-19, giving rise to "shoulder", in the ^{11}B + ^{209}Bi $\rightarrow$ ^{220}Ra* $\rightarrow$ A_1 + A_2 reaction for β_2 deformed case (see Fig. 4.3(b)) comes out to be negligibly small $\sim 10^{-6}$ to 10^{-10} mb, thereby indicating negligible contribution of quasi-fission (qf) component.

The deduced variation of the neck-length parameter ΔR as a function of $E_{c.m.}$ for both the ER and fission processes in ^{219}Ra and ^{220}Ra is shown in Fig. 4.5(a). Our analysis on the basis of DCM calculations show that ER is a prompt process since ΔR for this process is larger than that for fission for both the systems. In other words, the ΔR obtained via fitting procedure of fission (A_L = 82-93) cross-section is smaller than that obtained for evaporation residue (A_L = 1-4) cross-section. This result is consistent with the observation in [14] which shows that ΔR is larger for ER as compared to fission which simply means that ER process occurs first and the fission follows it, indicating that ER and fission processes occur at different time scales.

The use of different ΔR and/or ℓ_{max} values for different processes is also made in our earlier publications [12, 13]. Interestingly, the neck-length parameter ΔR is almost same for the fission process of ^{219}Ra and ^{220}Ra whereas the same for ER process is larger for heavier isotope i.e. ^{220}Ra. This can be inferred that the fission takes place almost at same time scale for ^{219}Ra and ^{220}Ra, and that the ER takes relatively more time for ^{219}Ra as compared to ^{220}Ra. This observation may be associated with relatively larger ER cross-sections observed in case of ^{220}Ra as

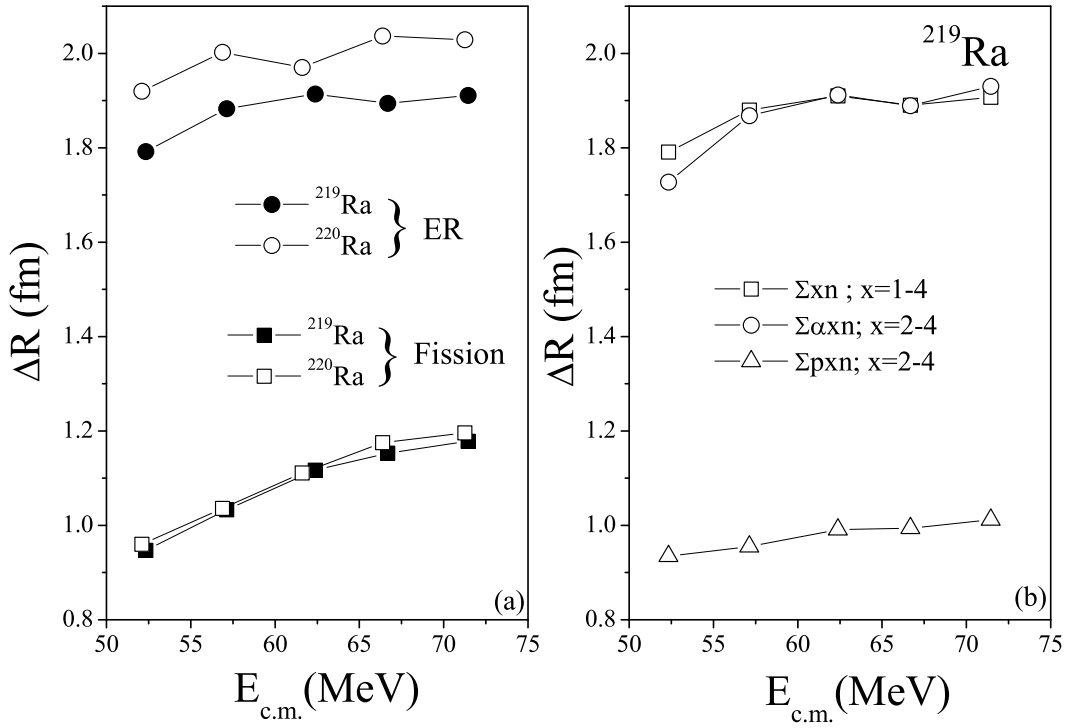

Figure 4.5 (a) The variation of fitted parameter ΔR with $E_{c.m.}$ for ER and fission processes in decaying ^{219,220}Ra* systems and (b) same as for (a) but for individual evaporation residue cross-section produced through xn, αxn and pxn emission channels in the decay of ^{219}Ra*.

compared to ^{219}Ra. The ΔR for the xn, αxn and pxn emission channels in the decay of ^{219}Ra is shown in Fig. 4.5(b), also discussed later in Sec. 4.2.2. Interestingly the neck length parameter ΔR for xn and αxn channel is similar to the one obtained for ER path, and that of pxn channel is similar to the ΔR values of fission process. One may conclude from here that pxn reaction rate is relatively slow and its time scale is similar to the one obtained for fission process.

Fig. 4.6(a) shows the "barrier lowering" parameter ΔV_B as a function of $E_{c.m.}$ for both the entrance channels forming ^{219}Ra and ^{220}Ra compound systems. Since the fission process consists of mainly AF, ΔV_B is illustrated for most probable asymmetric fission fragments, and for $\ell = \ell_{max}$. We notice from Fig. 4.6(a) that the "barrier

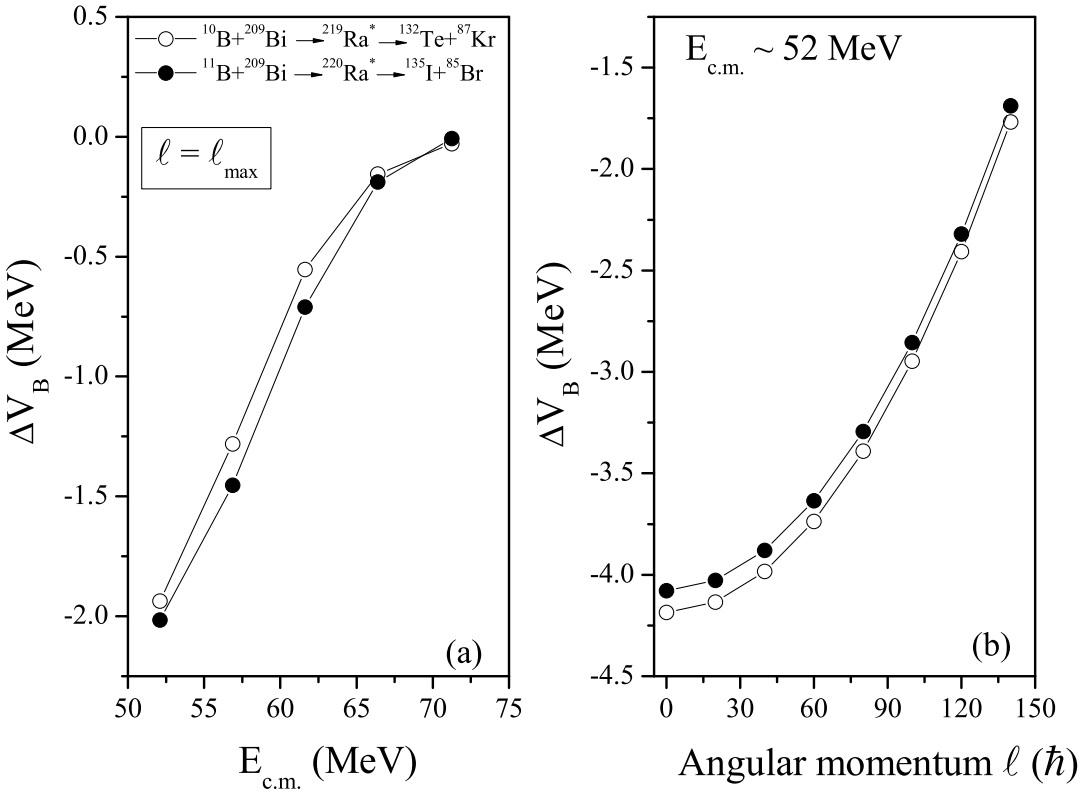

Figure 4.6 (a) Barrier lowering parameter ΔV_B in the DCM, as defined by Eq. (2.77) as a function of $E_{c.m.}$ for the asymmetric fission fragments illustrated for case of $\ell = \ell_{max}$ in the decay of ^{219}Ra* and ^{220}Ra* and (b) same as for (a) but ΔV_B as a function of ℓ at $E_{c.m.} \sim 52$ MeV.

lowering" at lower incident energies is an inbuilt property of the DCM i.e., ΔV_B increases with decreasing incident energy, and reaches a near constant zero value at the higher energies for both the channels. From Fig. 4.6(b) one can find that ΔV_B decreases exponentially with the increase in ℓ value for the decay of ^{219,220}Ra* into most probable asymmetric fission fragments. This observation is consistent with Fig. 4.1, where ΔV_B is shown to decrease with increase in ℓ value. It may be noted in Figs. 4.6(a) and (b) that dependance of ΔV_B on $E_{c.m.}$ and or ℓ-values is almost independent of projectile mass.

4.2.2 Excitation functions of charged-particle evaporation residues

Interestingly, in the experiment [17], apart from the contribution of fission cross-sections, a significant contribution from the cross-sections of the neutron evaporation channel i.e. $\sum \sigma_{xn}; x = 3, 4, ..6$ producing residual Ra evaporation residues along with a smaller contribution from other charged-particle evaporation residues produced through the αxn and pxn ($x = 2, 3, 4$) emission channels (namely Rn and Fr isotopes) in ^{219}Ra and ^{220}Ra are shown to contribute towards complete fusion cross-section of the ^{10}B + ^{209}Bi and ^{11}B + ^{209}Bi reactions. In addition to this, a significant amount of noncompound nucleus components in the form of incomplete fusion (ICF) - where one of the fragment produced in the breakup of projectile interacts with the target, is also measured in [17]. It may be noted that the contribution of fission cross-sections comes only from the CF, since the fission following ICF is expected to be negligible due to the lower angular momentum and excitation energy brought in by an ICF fragment [4]. Thus the contribution of ICF cross-section comes from evaporation residues (Rn and Fr isotopes) as will be discussed later in Sec. 4.2.3.

The calculated preformation probability (P_0) and penetration probability (P) as a function of angular momentum ℓ are shown in Fig. 4.7 for the LPs (neutron evaporation) for ^{219}Ra at highest value of energy $E_{c.m.} = 71.45$ MeV. Here the ℓ_{max}-value is fixed for the light-particle (here $xn, x = 1 - 4$) cross-sections $\sum_x \sigma_{xn}(\ell) \rightarrow 0$. We notice that at this highest energy, mass 1 fragment i.e ($1n$), seems to be preformed strongly in the DCM calculations contrary to experiments [17] where mass 3 ($3n$)

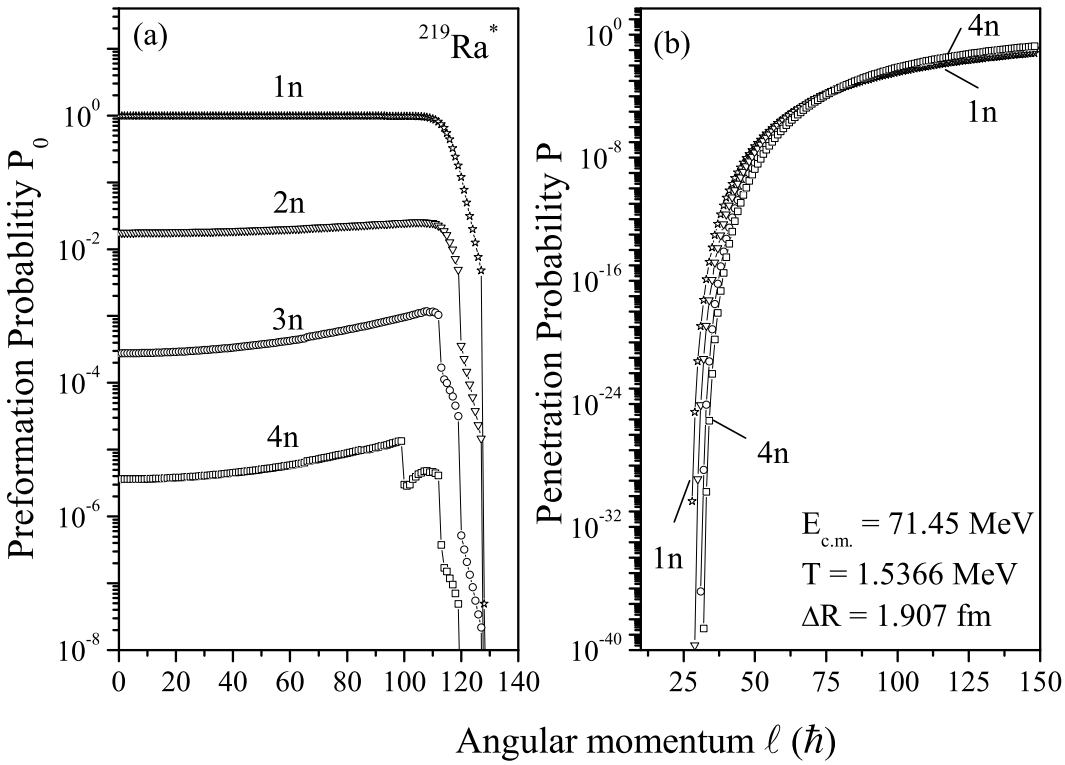

Figure 4.7 The preformation probability P_0 and penetrability P as a function of angular momentum ℓ for LP's $(xn, x = 1 - 4)$ calculated for the compound system ^{219}Ra* by using the fragmentation potential of Fig. 4.2.

to mass 6 $(6n)$ has a major contribution in light-particle cross-sections. However the behavior presented by penetrability is different i.e. the contribution of $1n$ is dominant at lower ℓ-value and the preference changes to $4n$ at higher ℓ-values.

Fig. 4.8 represents the contributions of different light-particle exit channels xn to the total evaporation cross-section $\sigma_{ER}(\ell)$ $(=\sum_x \sigma_{xn}(\ell))$ as a function of angular momentum ℓ. These calculations are done at energies near and above the barrier i.e. at $E_{c.m.} = 52.34$ MeV and 71.45 MeV. It is evident from Fig. 4.8 that a major contribution to the σ_{ER} comes from the $1n$ channel in our calculations contrary to experiments, where the $3n$ to $6n$ evaporation cross-sections dominate the neutron evaporation process. It may be because of the range of neck length parameter ΔR, which we take maximum upto 2 fm in context of the proximity interactions.

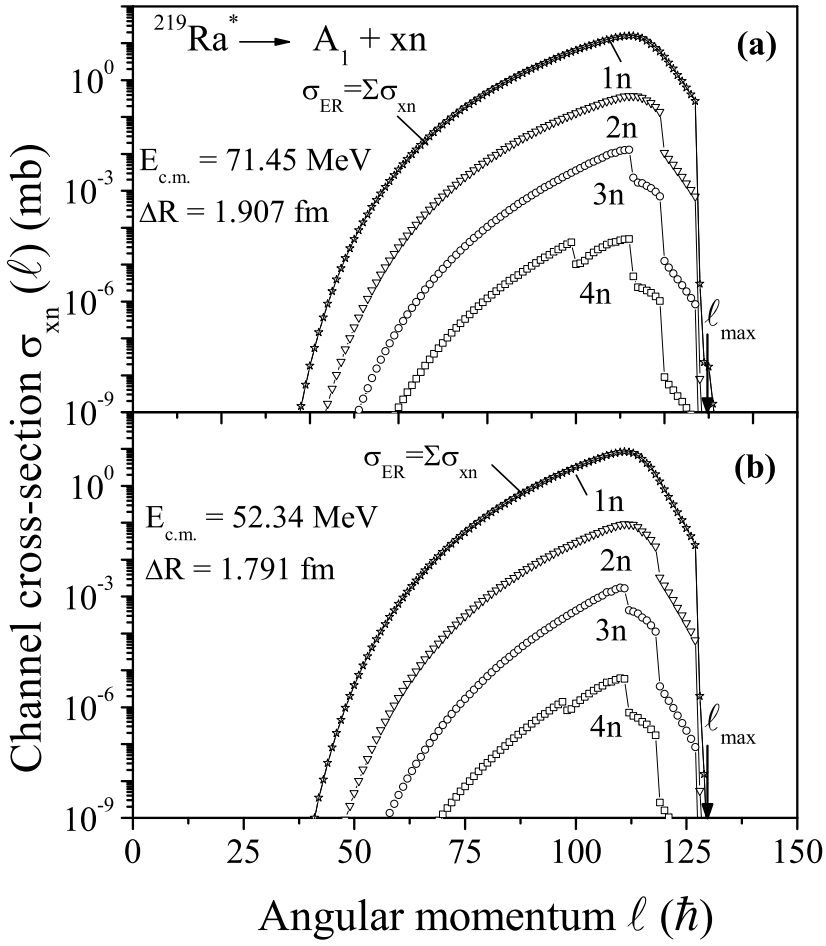

Figure 4.8 Contributions of different LP's, the xn, to the total cross-section $\sigma_{ER}(\ell)$ at different $E_{c.m.}$'s: (a) at $E_{c.m.}$ = 71.45 MeV and (b) 52.34 MeV.

It is well known that the Coulomb interaction alone is not enough to describe the formation of a compound nuclear system, beside this the nuclear interaction plays a very significant role. The long range part of the interaction potential are determined from the Coulomb and centrifugal interactions, and the short distance behavior strongly depends upon the nuclear surface properties, resulting in potential pockets which determine the characteristics of the compound system formed due to the collision between the two nuclei. Blocki *et al.* [19] introduced a simple formula for nucleus-nucleus interaction energy as a function of separation between the surfaces of

Table 4.2 The DCM calculated cross-sections for the neutron evaporation residues obtained by summing xn ($x = 1-4$) neutron evaporation channels for different $E_{c.m.}$'s following the complete fusion of ^{10,11}B with ^{209}Bi forming ^{219,220}Ra* compound systems, compared with experimental data [17].

$E_{c.m.}$ (MeV)	T (MeV)	ℓ_{max} ($\hbar$)	ΔR (fm)	$\sum_{xn}\sigma_{Ra}$(mb) DCM ($x = 1-4$)	Expt.
		^{10}B+^{209}Bi$\rightarrow^{219}$Ra$^* \rightarrow A_1 + A_2$			
52.34	1.2506	128	1.791	133	134 ± 3
57.13	1.3282	126	1.88	272	273 ± 5
62.38	1.4082	126	1.91	320	322 ± 7
66.68	1.4705	129	1.89	314	315 ± 7
71.45	1.5366	128	1.907	294	294 ± 5
		^{11}B+^{209}Bi$\rightarrow^{220}$Ra$^* \rightarrow A_1 + A_2$			
52.10	1.1643	118	1.92	226	226 ± 7
56.88	1.2468	118	2.002	403	403 ± 7
61.61	1.3233	123	1.970	469	462 ± 6
66.38	1.3962	119	2.037	477	471 ± 7
71.25	1.4668	120	2.029	437	430 ± 7

the two colliding nuclei, known as the "pocket formula" of proximity potential. The proximity formula for the interaction potential is free from any adjusting parameter and uses the measured values of surface tension and surface diffuseness. Since both the thickness of the nuclear surface and the range of the nuclear interaction are of the order of 1.5-2 fm, therefore the range of ΔR is constrained to a limit of $\sim$ 2 fm.

However, if one relaxes this condition and allow $\Delta R > 2$ fm then the reported $\sum \sigma_{xn}$ cross-section can also be achieved without including $1n$ or $2n$ cross-section. But in present calculations we have taken $\Delta R \leq 2$ fm and hence $1n$ cross-section contribute maximum towards ER component.

The calculated total cross-section for the neutron evaporation residues obtained

Table 4.3 The DCM calculated cross-sections for individual charged particle (αxn) evaporation residues formed via the complete fusion in ^{10}B+^{209}Bi reaction, compared with the experimental data [17].

$E_{c.m.}$ (MeV)	ΔR (fm)	$\sigma_{\alpha 2n}(^{213}\text{Rn})$ (mb)	$\sigma_{\alpha 3n}(^{212}\text{Rn})$ (mb)	$\sigma_{\alpha 4n}(^{211}\text{Rn})$ (mb)	$\sum\sigma_{Rn}$(mb) DCM	Expt.
52.34	1.727	0.75	2.58×10^{-2}	1.97×10^{-2}	0.793	0.798
57.13	1.868	2.98	6.48×10^{-2}	3.27×10^{-2}	3.08	3.08
62.38	1.912	4.72	8.86×10^{-2}	3.31×10^{-2}	4.84	4.83
66.68	1.889	5.57	1.25×10^{-1}	2.71×10^{-2}	5.72	5.74
71.45	1.93	7.20	1.86×10^{-1}	3.80×10^{-2}	7.43	7.42

by summing $1n$, $2n$, $3n$ and $4n$ evaporation channels forming different Ra isotopes for the ^{10}B + ^{209}Bi and ^{11}B + ^{209}Bi reactions are listed in Table 4.2. It is clearly evident from Tables 4.1 and 4.2 that neutron evaporation residues contributes maximum to complete fusion cross-section at lower energies whereas contribution of fission is maximum at higher energies. One may see that ΔR and ℓ_{max}-values for neutron evaporation and total evaporation residues for ^{10}B induced channel in Tables 4.1 and 4.2 are quite identical. Note that even ΔR taken for evaporation residue work nicely for $\sum\sigma_{xn}$ cross-sections as is evident from the Table 4.2 for the case of ^{11}B induced channel. This shows that neutron evaporation is the major contributor towards ER process and the reported αxn and pxn cross-sections contribute minimal towards total fusion cross-section which is also evident from Fig. 4.4(c).

In addition to this, the cross-section for the other charged evaporation residues ^{213}Rn, ^{212}Rn, ^{211}Rn, ^{216}Fr, ^{215}Fr and ^{214}Fr which are formed via the αxn and pxn emission from ^{219}Ra nucleus are also listed in Tables 4.3 and 4.4, respectively. It may be noted that ICF process dominates the $\sum\sigma_{Rn}$ and $\sum\sigma_{Fr}$ cross-sections, having, respectively 7% and 10% contribution through CF route. The $\sum\sigma_{Rn}$ and $\sum\sigma_{Fr}$

Table 4.4 The DCM calculated cross-sections for individual charged particle (pxn) evaporation residues formed via the complete fusion in ^{10}B+^{209}Bi reaction, compared with the experimental data [17].

$E_{c.m.}$ (MeV)	ΔR (fm)	$\sigma_{p2n}(^{216}\text{Fr})$ (mb)	$\sigma_{p3n}(^{215}\text{Fr})$ (mb)	$\sigma_{p4n}(^{214}\text{Fr})$ (mb)	$\sum\sigma_{Fr}$(mb) DCM	Expt.
52.34	0.935	8.24×10^{-2}	1.65×10^{-1}	0.45	0.697	0.69
57.13	0.955	2.24×10^{-1}	3.31×10^{-1}	0.74	1.30	1.3
62.38	0.991	6.63×10^{-1}	7.31×10^{-1}	1.53	2.89	2.9
66.68	0.994	8.39×10^{-1}	9.71×10^{-1}	1.81	3.62	3.6
71.45	1.012	9.58×10^{-1}	11.7×10^{-1}	1.92	4.04	4

coming from CF route in ^{10}B induced channel are listed in Tables 4.3 and 4.4 and the ICF component is dealt in Sec. 4.2.3.

We notice from Fig. 4.5(b) that different neck length parameters ΔR's are chosen to fit cross-section for individual channels at different energies which shows different reaction time scale for ER produced through pxn emission channel as compared to xn and αxn emission channels which occur almost simultaneously. It is to be noted that centre-of-mass energies have been corrected to study the decay of Rn and Fr isotopes from parent nucleus ^{219}Ra. The correction has been made on the basis of the assumption that equal energy is being distributed among all the nucleons of the composite system formed. Since energies are different so the choice of taking different ΔR's (and hence the correspondingly ℓ_{max}) also seems justified.

4.2.3 Incomplete fusion cross-sections

The CF data clearly indicate that Ra isotopes result from neutron evaporation from the compound nucleus formed following complete fusion of the projectile (^{10,11}B)

Table 4.5 The cross-sections calculated using DCM for incomplete fusion products resulting from the reaction of ^{6}Li with ^{209}Bi forming ^{215}Rn* compared with experimental data [17] along with the corrected centre-of-mass energies $E^{c}_{c.m.}$.

$E^{c}_{c.m.}$ (MeV)	ℓ_{max} ($\hbar$)	ΔR (fm)	$\sigma_{1n}(^{214}\mathrm{Rn})$ (mb)	$\sigma_{2n}(^{213}\mathrm{Rn})$ (mb)	$\sigma_{3n}(^{212}\mathrm{Rn})$ (mb)	$\sigma_{4n}(^{211}\mathrm{Rn})$ (mb)	$\sum\sigma_{Rn}$(mb) DCM	Expt.
31.98	133	1.455	10.5	4.24×10^{-2}	4.18×10^{-4}	6.07×10^{-6}	10.5	10.60
34.90	135	1.543	40.3	1.97×10^{-1}	3.00×10^{-3}	4.51×10^{-5}	40.5	40.92
38.11	132	1.612	64.1	3.49×10^{-1}	4.83×10^{-3}	8.08×10^{-5}	64.5	64.17
40.75	133	1.631	75.7	4.90×10^{-1}	8.22×10^{-3}	1.47×10^{-4}	76.2	76.26
43.65	132	1.664	97.7	7.19×10^{-1}	1.28×10^{-2}	2.58×10^{-4}	98.5	98.58

with the target (^{209}Bi). The Rn and Fr nuclei result from αxn and pxn decay from Ra nuclei. Thus the complete fusion followed by αxn and pxn evaporation leads to Rn and Fr residual nuclei. The DCM calculated cross-sections for αxn and pxn evaporation residues formed via complete fusion are listed in Tables 4.3 and 4.4 for illustrative case of the ^{10}B channel.

In the following we shall deal with ICF based cross-sections reported due to break up of ^{10}B projectile. The breakup of the projectile into two charged fragments provides a mechanism for the direct production of Rn and Fr isotopes e.g. the breakup of ^{10}B into ^{6}Li and ^{4}He followed by absorption of ^{6}Li by ^{209}Bi will lead to the formation of ^{215}Rn nuclei directly. Similarly the breakup of ^{10}B into ^{8}Be and ^{2}H, ^{9}Be and ^{1}H followed by absorption of ^{8}Be and ^{9}Be respectively will lead to the formation of ^{217}Fr and ^{218}Fr. Subsequent evaporation of neutrons from these nuclei will give rise to various isotopes of Rn and Fr. Note that these Rn and Fr cross-sections are mainly attributed to ICF [17], where following the breakup of the projectile, just one of the charged fragments fuses with the target. For example, the

Table 4.6 The cross-sections calculated using DCM for incomplete fusion products resulting from the reaction of ^{8}Be with ^{209}Bi forming ^{217}Fr* along with the corrected centre-of-mass energies $E^c_{c.m.}$.

$E^c_{c.m.}$ (MeV)	ℓ_{max} ($\hbar$)	ΔR (fm)	$\sigma_{1n}(^{216}\text{Fr})$ (mb)	$\sigma_{2n}(^{215}\text{Fr})$ (mb)	$\sigma_{3n}(^{214}\text{Fr})$ (mb)	$\sum_{xn}\text{Fr(mb)}$ $(x = 1-3)$
42.25	128	1.494	5.86	9.18×10^{-2}	4.07×10^{-4}	5.95
46.11	130	1.533	10.8	1.80×10^{-1}	9.00×10^{-4}	11.0
50.35	131	1.591	24.4	4.74×10^{-1}	2.73×10^{-3}	24.9
53.82	132	1.61	29.9	6.47×10^{-1}	4.85×10^{-3}	30.5
57.67	132	1.62	33.1	8.62×10^{-1}	7.07×10^{-3}	34.0

reaction product ^{212}Rn is expected to be formed by complete fusion ($\alpha 3n$) channel and/or incomplete fusion (i.e., the fusion of ^{6}Li by ^{209}Bi) followed by emission of three neutrons from ^{215}Rn*. The remaining α-fragment (^{4}He) of the incident ion is assumed to go on moving with beam velocity in forward direction without any noticeable interaction with target nucleus. Thus the cross-sections of ^{214,213,212,211}Rn evaporation residues may be attributed to the contribution coming from incomplete fusion process of the type

$$^{10}\text{B}(^{6}\text{Li} + ^{4}\text{He}) \Rightarrow ^{6}\text{Li} + ^{209}\text{Bi} \Rightarrow ^{215}\text{Rn} + ^{4}\text{He} \qquad (\alpha \text{ as spectator})$$

Also the contribution for the cross-sections of ^{216,215,214}Fr evaporation residues comes from the incomplete fusion process of the type

$$^{10}\text{B}(^{8}\text{Be} + ^{2}\text{H}) \Rightarrow ^{8}\text{Be} + ^{209}\text{Bi} \Rightarrow ^{217}\text{Fr} + ^{2}\text{H} \qquad (\text{deuteron as spectator})$$

Alternatively the contribution for the ^{216,215,214}Fr evaporation residues cross-sections may also come from the incomplete fusion process of the type

$$^{10}\text{B}(^{9}\text{Be} + ^{1}\text{H}) \Rightarrow ^{9}\text{Be} + ^{209}\text{Bi} \Rightarrow ^{218}\text{Fr} + ^{1}\text{H} \qquad (\text{hydrogen as spectator})$$

The cross-sections for the incomplete fusion products of Rn and Fr isotopes are listed in Tables 4.5, 4.6 and 4.7. Note that DCM have been applied successfully

Table 4.7 The cross-sections calculated using DCM for incomplete fusion products resulting from the reaction of ^{9}Be with ^{209}Bi forming ^{218}Fr* compared with experimental data [17] along with the corrected centre-of-mass energies $E^{c}_{c.m.}$. Here $\sum\sigma_{Fr}$=$\sum_{xn}$Fr+$\sum_{yn}$Fr

$E^{c}_{c.m.}$ (MeV)	ℓ_{max} ($\hbar$)	ΔR (fm)	$\sigma_{2n}(^{216}\text{Fr})$ (mb)	$\sigma_{3n}(^{215}\text{Fr})$ (mb)	$\sigma_{4n}(^{214}\text{Fr})$ (mb)	$\sum_{yn}$Fr(mb) ($y=2-4$)	$\sum\sigma_{Fr}$(mb) DCM	Expt.
47.31	131	1.494	0.248	3.98×10^{-3}	1.79×10^{-5}	0.252	6.20	6.21 ± 0.9
51.64	132	1.533	0.583	9.42×10^{-3}	4.77×10^{-5}	0.592	11.6	11.7 ± 1.8
56.39	131	1.591	1.24	2.07×10^{-2}	1.13×10^{-4}	1.26	26.2	26.1 ± 2.7
60.28	132	1.61	1.72	3.86×10^{-2}	2.25×10^{-4}	1.76	32.3	32.4 ± 3.6
64.58	132	1.62	2.15	5.24×10^{-2}	3.35×10^{-4}	2.20	36.2	36 ± 3.6

for CN decay processes and this is one of the first attempt when its being applied to investigate ICF process. It is well known that in ICF process, the projectile breaks up into two parts before fusion and hence the properties of projectile and their respective energies get modified. So an energy correction has been made on the projectile (or lab) energy (or equivalently on the centre-of-mass energies). The modified energy of new projectile in ICF process is worked out as

$$E^{P}_{ICF} = \frac{E}{A}\times A^{P} - \frac{E}{A}\times A^{E}$$

where A^{P} represent the mass of actual projectile (without breakup) and A^{E} is the mass of ejectile/spectator nucleus.

It is clearly evident from Tables 4.5-4.7 that our DCM based ICF cross-sections find good fitting procedures with the experimental ICF cross-sections at all the reported energies. One can see that the incomplete fusion contribution increases with the c.m energy (or projectile energy) which is expected as the break-up probability

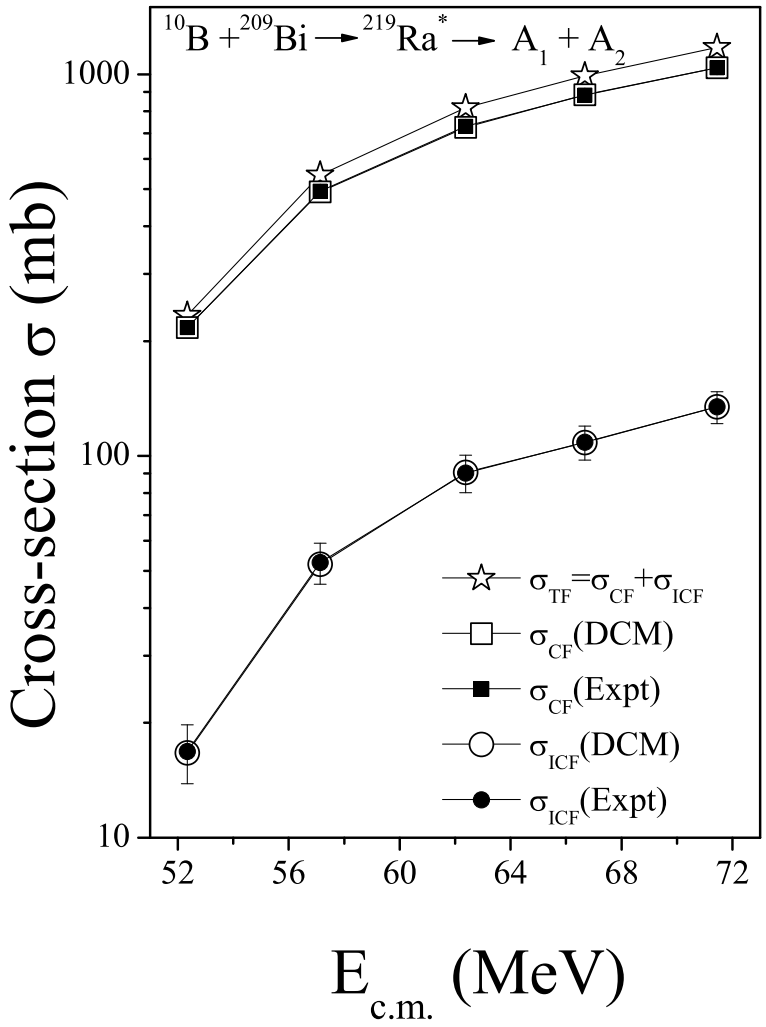

Figure 4.9 Total fusion cross-section along with the individual complete (σ_{CF}) and incomplete fusion contributions (σ_{ICF}) calculated using DCM compared with the experimental σ_{CF} and σ_{ICF} at different energies for the ^{10}B + ^{209}Bi system.

of the incident ion increases significantly with projectile energy.

It may be noted that only $\sum \sigma_{Rn}$ and $\sum \sigma_{Fr}$ are reported in [17] and here we have predicted individual contribution of Rn and Fr isotopes, contributing towards ICF component. The contributions coming from all incomplete fusion channels σ_{ICF} (=$\sum \sigma_{Rn}$+ $\sum \sigma_{Fr}$) and the complete fusion σ_{CF} (obtained by summing the fission and evaporation residue cross-sections) along with the total-fusion cross-section σ_{TF}(= σ_{CF} + σ_{ICF}) for ^{10}B + ^{209}Bi system is shown in Fig. 4.9.

As can be observed from the Fig. 4.9, the ICF contribution to the total-fusion cross-section is small as compared to CF contribution. One may see that the separation between the plot for σ_{TF} (stars) and σ_{CF} (squares) increases with c.m. energy (or projectile energy) indicating that contribution of ICF is larger at highest projectile energy. This may be due to the increasing probability of break up of incident projectile into α cluster (^{6}Li + α) and/or (^{8}Be + ^{2}H and ^{9}Be + ^{1}H) as the projectile energy increases.

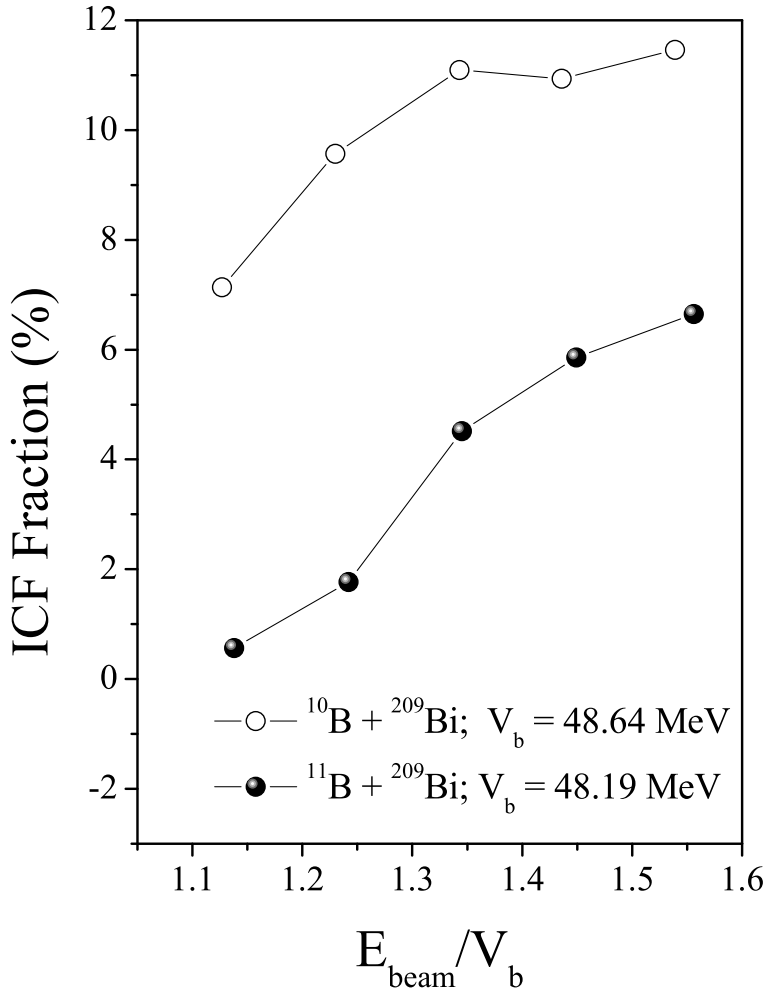

Figure 4.10 Percentage incomplete fusion fraction (F_{ICF}) as a function of reduced projectile energy (E_{beam}/V_b) for the ^{10}B + ^{209}Bi and ^{11}B + ^{209}Bi systems.

Further, the effect of projectile energy and mass asymmetry of interacting partners on the relative contributions of complete and incomplete fusion fraction is worked out and the percentage incomplete fusion fraction (F_{ICF}) for both the systems is calculated as [20]

$$F_{ICF} = \frac{\Sigma\sigma_{ICF}}{\sigma_{TF}} \times 100$$

The F_{ICF} for both the systems is plotted as a function of reduced projectile energy (E_{beam}/V_b, where V_b is Coulomb barrier of respective systems) in Fig. 4.10. Note that, here the ICF data is fitted only for ^{219}Ra compound nucleus and the same for ^{220}Ra is taken from [17]. It is clear from Fig. 4.10 that the relative percentage F_{ICF} is $\approx$ 7% of the total-fusion cross-section (σ_{TF}) at the lowest energy (i.e., $\approx$ 52 MeV) in case of ^{10}B + ^{209}Bi system, which increases with the projectile energy. However at the highest energy (i.e., $\approx$ 71 MeV), the relative percentage of ICF fraction approaches to $\approx$ 11% of σ_{TF}. Similarly the ICF fraction for ^{11}B + ^{209}Bi system at $\approx$ 52 MeV is $\approx$ 0.5 % of σ_{TF}, but at $\approx$ 71 MeV, it approaches to $\approx$ 7% of the total-fusion cross-section. One can clearly see that over a range of projectile energies, the ICF fraction is more for ^{10}B + ^{209}Bi system than that for ^{11}B + ^{209}Bi system, which shows the sensitiveness of ICF fraction to the mass asymmetry of interacting partners, supporting the systematics presented by Morgenstern *et al.* [7].

It may be reminded here that CF contribution consists of fission, neutron evaporation along with other charged-particle evaporation residues. Since the DCM calculated CF and ICF cross-sections compare nicely with experimentally determined CF and ICF cross-sections so one may conclude that DCM can also be applied for ICF process along with its well-established application in the CF process.

4.3 Summary

Summarizing, in this chapter we have calculated fission excitation functions for the reactions of ^{10}B and ^{11}B with ^{209}Bi forming ^{219}Ra* and ^{220}Ra* compound systems over a wide range of incident energies using DCM. The DCM calculated σ_{fiss} (as well as the σ_{ER}) find nice comparison with the experimental data for both the compound systems with negligible contribution of quasi-fission component. In addition to this, the excitation functions for CF obtained by summing the fission, neutron evaporation and charged-particle evaporation residues produced through the αxn and pxn ($x = 2, 3, 4$) emission channels for ^{219}Ra system at various incident c.m. energies are found to be in good agreement with the experimental data. Experimentally the fusion suppression is shown to be operating in these reactions and the observed suppression is attributed to the prompt breakup of projectile into different clusters, the probability of breakup increases with the incident projectile energy. So, an attempt has been made for the first time to study ICF processes using DCM. Interestingly, the ICF-calculated excitation functions formed in ^{219}Ra system show good agreement with the experimental data, within one parameter fit of the model and relevant energy corrections. It may be noted that individual contributions of ICF cross-sections of various isotopes of Rn and Fr is estimated using DCM.

The deformation effects upto hexadecapole are duly worked out in context of $^{11}\text{B} + {}^{209}\text{Bi} \rightarrow {}^{220}\text{Ra}^{*} \rightarrow A_1 + A_2$ reaction and the fragmentation path changes its behavior from relatively symmetric to asymmetric fragment distribution with inclusion of deformation effects. The behavior of neck length parameter indicate that fission occur almost simultaneously in ^{10}Bi and ^{11}Bi induced reactions whereas the ER of ^{220}Ra occurs relatively at an early stage.

Bibliography

[1] F. Schussler, H. Nifenecker, B. Jakobsson, V. Kopljar, K. Soderstrom, S. Leray, C. Ngo, S. Souza, J. P. Bondorf, and K. Sneppen, Nucl. Phys. A **584**, 704 (1995).

[2] E. Gadioli, C. Brattari, M. Cavinato, E. Fabrici, E. Gadioli Erba, V. Allori, A. Di. Filippo, S. Vailati, T. G. Stevens, S. H. Connell, J. P. F. Sellschop, F. M. Nortier, G. F. Steyn, and C. Marchetta, Nucl. Phys. A **641**, 271 (1998).

[3] S. Gupta, B. P. Singh, M. M. Musthafa, H. D. Bhardwaj, and R. Prasad, Phys. Rev. C **61**, 064613 (2000).

[4] M. Dasgupta, P. R. S. Gomes, D. J. Hinde, S. B. Moraes, R. M. Anjos, A. C. Berriman, R. D. Butt, N. Carlin, J. Lubian, C. R. Morton, J. O. Newton, and A. Szanto de Toledo, Phys. Rev. C **70**, 024606 (2004).

[5] N. Keeley, R. Raabe, N. Alamanos, and J. L. Sida, Prog. Part. Nucl. Phys. **59**, 579 (2007).

[6] L. F. Canto, P. R. S. Gomes, R. Donangelo, and M. S. Hussein, Phys. Rep. **424**, 1 (2006).

[7] H. Morgenstern, W. Bohne, W. Galster, K. Grabisch, and A. Kyanowski, Phys. Rev. Lett. **52**, 1104 (1984).

[8] G. Sawhney and M. K. Sharma, Eur. Phys. J. A **48**, 57 (2012).

[9] M. Kaur, R. Kumar, and M. K. Sharma, Phys. Rev. C **85**, 014609 (2012).

[10] M. K. Sharma, G. Sawhney, R. K. Gupta, and W. Greiner, J. Phys. G: Nucl. Part. Phys. **38**, 105101 (2011).

[11] G. Sawhney, M. K. Sharma, and R. K. Gupta, Phys. Rev. C **83**, 064610 (2011).

[12] M. K. Sharma, S. Kanwar, G. Sawhney, R. K. Gupta, and W. Greiner, J. Phys. G: Nucl. Part. Phys. **38**, 055104 (2011); D. Jain, R. Kumar, M. K. sharma, and R. K. Gupta, Phys. Rev. C **85**, 024615 (2012).

[13] B. B. Singh, M. K. Sharma, and R. K. Gupta, Phys. Rev. C **77**, 054613 (2008).

[14] S. Kanwar, M. K Sharma, B. B Singh, R. K. Gupta, and W. Greiner, Int. J. Mod. Phys E **18**, 1453 (2009).

[15] R. K. Gupta, M. Balasubramaniam, R. Kumar, N. Singh, M. Manhas, and W. Greiner, J. Phys. G : Nucl. Part. Phys. **31**, 631 (2005).

[16] R. K. Gupta, M. Manhas, and W. Greiner, Phys. Rev. C **73**, 054307 (2006).

[17] L. R. Gasques, D. J. Hinde, M. Dasgupta, A. Mukherjee, and R. G. Thomas, Phys. Rev. C **79**, 034605 (2009).

[18] P. Möller, J. R. Nix, W. D. Myers, and W. J. Swiatecki, At. Nucl. Data Tables **59**, 185 (1995).

[19] J. Blocki, J. Randrup, W.J. Swiatecki, and C.F. Tsang, Ann. Phys. (N.Y.) **105**, 427 (1977).

[20] P. P. Singh, B. P. Singh, M. K. Sharma, Unnati, D. P. Singh, R. Prasad, R. Kumar, and K. S. Golda, Phys. Rev. C **77**, 014607 (2008).

Chapter 5

Decay of ^{241}Pu* formed in ^{9}Be+^{232}Th around Coulomb barrier using static and dynamic deformations

5.1 Introduction

The reaction dynamics of hot and rotating compound nucleus ^{241}Pu* formed in ^{9}Be + ^{232}Th reaction around the Coulomb barrier ($\approx$ 42.16 MeV), at energies ranging from 37 to 48 MeV, is studied using the dynamical cluster-decay model (DCM) which is extended to include the temperature dependant (dynamic) deformations effects of nuclei. It is important to note that so far only the static deformations [1] have been used in our previous chapters, to address a number of nuclear behavior using a

variety of heavy ion reactions. However, in the present work, possible fragmentation path in reference to temperature dependant (dynamic) deformations [2, 3] is also worked out in the framework of DCM to analyze the possible role of T-dependant deformations in the reaction under consideration. The dynamic deformations disappear exponentially as a function of temperature. This means that with the increase in temperature (T), the effect of dynamic deformations decreases and approaches to zero at higher temperature. In the following some general features relevant to this work are discussed and details of the calculations are given in further section.

It has been established that the fusion reactions induced by weakly bound projectiles contribute immensely in the development and understanding of nuclear reaction dynamics. These reactions are sensitive to not only the entrance channel of interacting heavy ions forming the compound nucleus, but also to the other aspects of intermediate composite as it equilibrates in energy, mass, angular momentum and orientation degrees of freedom. It is well known that the entrance channel mass asymmetry η [$= (A_T - A_P)/(A_T + A_P)$, where A_T and A_P are the target and projectile mass, respectively] with respect to the Businaro-Gallone critical mass asymmetry α_{BG} plays an important role in the reaction dynamics [4, 5]. Several measurements involving reactions with lighter projectiles like ^{6,7}Li, ^{9}Be, ^{10,11}B and ^{12}C on deformed actinide targets, found that the anisotropies exceed the standard statistical saddle-point model (SSPM) predictions by large amounts, at sub-barrier energies. This anomalous behavior of the fragment anisotropies has been a subject of extensive investigations both experimentally and theoretically in the recent past. It was reported in Ref. [6] that anomalous fragment anisotropies in case of highly fissile target nuclei arise due to admixture of compound nucleus (CN) fission along

with noncompound nucleus (nCN) fission events in form of QF, ICF or DIC.

Various models like pre-equilibrium fission model of Ramamurthy and Kapoor [6, 7] and entrance channel dependent (ECD) K-state model by Vorkapic and Ivanisevic [8] were proposed to explain the anomalous fission fragment angular distribution for the systems having contribution from noncompound nucleus fission. A systematic study [9] on the behavior of stable weakly bound projectiles ^{6,7}Li and ^{9}Be on heavy targets like ^{208}Pb and ^{209}Bi was made and observed that complete fusion (CF) is suppressed by around 30%. This fusion suppression was observed to be associated with the presence of ICF.

Recently, ^{9}Be beam is used and fission fragment anisotropies, together with fission excitation functions are measured for compound nucleus ^{241}Pu* formed by the ^{9}Be + ^{232}Th reaction over a wide range of energies spread around Coulomb barrier [10]. As expected, σ_{fiss} for the highly fissile ^{241}Pu* is the major contributor to the total decay cross-sections and the contribution from evaporation residue cross-section σ_{ER} is not measured in [10]. Comparison of anisotropy data for CN ^{241}Pu* is in good accord with the predictions of SSPM at above barrier energies but show significant deviations for energies below the barrier. The higher anisotropy observed for ^{9}Be + ^{232}Th reaction cannot be explained in terms of other reaction mechanisms such as quasi-fission since it takes place for more symmetric systems and usually for projectiles heavier than $A = 20$ [11]. Also for this system $\eta > \alpha_{BG}$, therefore deviation of the fission fragment angular distribution from statistical theory is not expected on the basis of pre-equilibrium fission model [6, 7]. Thus, the noted deviation in the measured anisotropy data from SSPM predictions seem to be associated with the possible breakup of loosely bound ^{9}Be projectile nucleus as suggested in

Ref. [10].

The compound system $^{241}Pu^*$ ($\alpha_{BG} = 0.882$) formed in ^{9}Be + ^{232}Th ($\eta = 0.925$) reaction is chosen in reference to [10]. The projectile, target, and the compound nucleus formed are all strongly deformed so the role of deformation and orientation effects is expected to be important in the context of present study. The calculations are performed using DCM [12]- [16] for deformed fragments using quadrupole (β_2) deformations having "optimum" orientations θ^{opt} taken from Table 1 of Ref. [17] and the higher multipole deformations (β_2-β_4) having "compact" orientations θ^c of hot configurations [18].

It is observed that with the inclusion of temperature dependent (dynamic) deformations of the decaying fragments, potential energy surface (PES) change quite significantly and as a result the relative preformation probabilities P_0 for all the fragments gets modified accordingly. Also the scattering potential (corresponding barrier position, height and frequency) is modified with the inclusion of temperature dependent deformations of outgoing fragments, thereby affecting the tunneling probability P through barrier.

In this work the data of Ref. [10] is used to fix the only parameter of DCM "neck-length parameter ΔR". For deformations up to β_2 (quadrupole), the fission distribution remains asymmetric for both the cases of static and dynamic deformed considerations, whereas a small contribution of symmetric fission is also observed when higher order static deformation effects up to β_4 (hexadecapole) are included. The calculated fission-fragment anisotropies are found to be consistent with the SSPM and pre-equilibrium fission (PEQ) model predictions at above barrier energies, but fails to reproduce the same at near and below barrier energies in agreement

with [10]. The main aim of this work is (i) to study the role of static and dynamic deformations in the decay of $^{241}Pu^{*}$ using DCM at both the below-and above barrier energies; (ii) to identify the time scale at which fission fragments are emitted for static and dynamic choice of deformations; (iii) to investigate barrier modification effect, particularly at below barrier region, as such effect is known to be important to resolve the issue of fusion hindrance in coupled channel calculations; (iv) to investigate fission anisotropies in context of $^{9}Be+^{232}Th$ reaction; (v) to explore the possibility of nCN competing channel, if any, on the basis of DCM. This information is expected to impart important information for overall understanding of fusion-fission dynamics involved in weakly bound reactions.

In general, static deformation of the nucleus has its origin in shell effects and at high excitation energies the shell effects vanish and thus static deformation should approach zero [2,3,19]. So in order to simulate this effect the deformation parameter β_i is taken to be temperature dependent in DCM using the relation [2,3].

$$\beta_{\lambda i}(T) = exp(-T/T_0)\beta_{\lambda i}(0); i = 1, 2$$

where $\beta_{\lambda i}(0)$ is static deformation and T_0 is the temperature of the nucleus at which shell effects start to vanish (T_0=1.5 MeV) [2]. Thus the choice of temperature dependent deformation parameter is consistent with static deformation when the temperature approaches zero i.e. $T \rightarrow 0$.

The organization of chapter is as follows: The results of our calculations for both the fission excitation functions and fission fragment anisotropies are discussed in Sec. 5.2 and a brief summary of results in Sec. 5.3.

5.2 Calculations

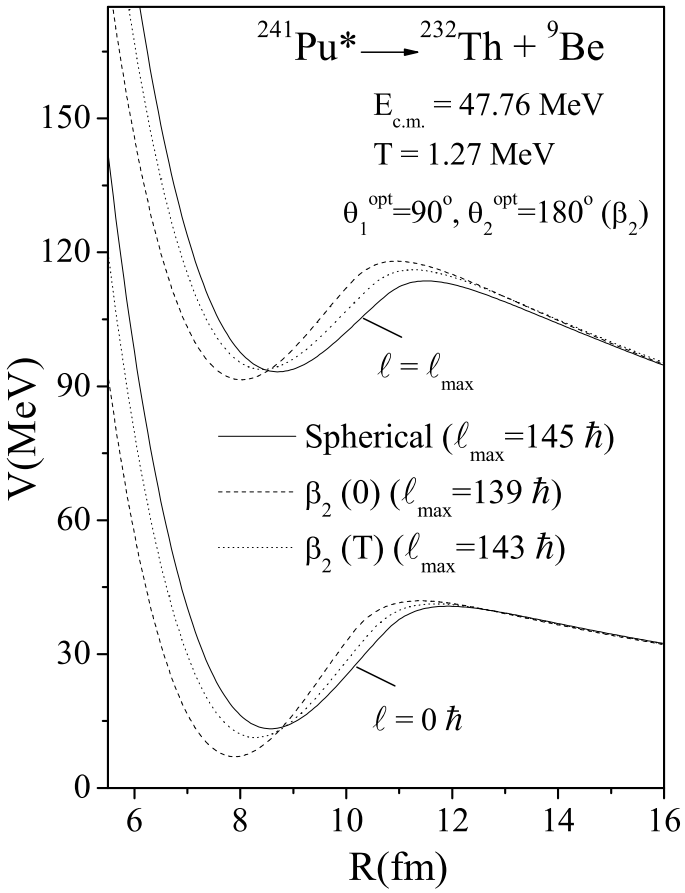

Figure 5.1 The scattering potential $V(R)$ for the decay of ^{241}Pu*→^{232}Th+^{9}Be at $E_{c.m.}$ = 47.76 MeV calculated at ℓ=0 and ℓ_{max} taking the two fragments as spheres, with static and dynamic considerations up to β_{2i} alone having "optimum" hot orientations θ_i^{opt} of Table 1 in Ref. [17].

In this section, the characteristics of decay barrier height, potential energy surfaces, preformation probability, penetrability, and barrier-lowering effect are studied using DCM, for the use of both static and dynamic deformations in the decay of compound nucleus ^{241}Pu* formed in the ^{9}Be + ^{232}Th reaction. The angular momentum dependence of above mentioned variables is studied to get fission excitation functions to be compared with experimental data [10]. These calculations are performed

for the use of sticking moment of inertia I_S which is found to be more appropriate for obtaining the fission cross-sections which involve comparatively larger limiting ℓ_{max} value whereas the non-sticking moment of inertia I_{NS} is found more appropriate for anisotropy calculations.

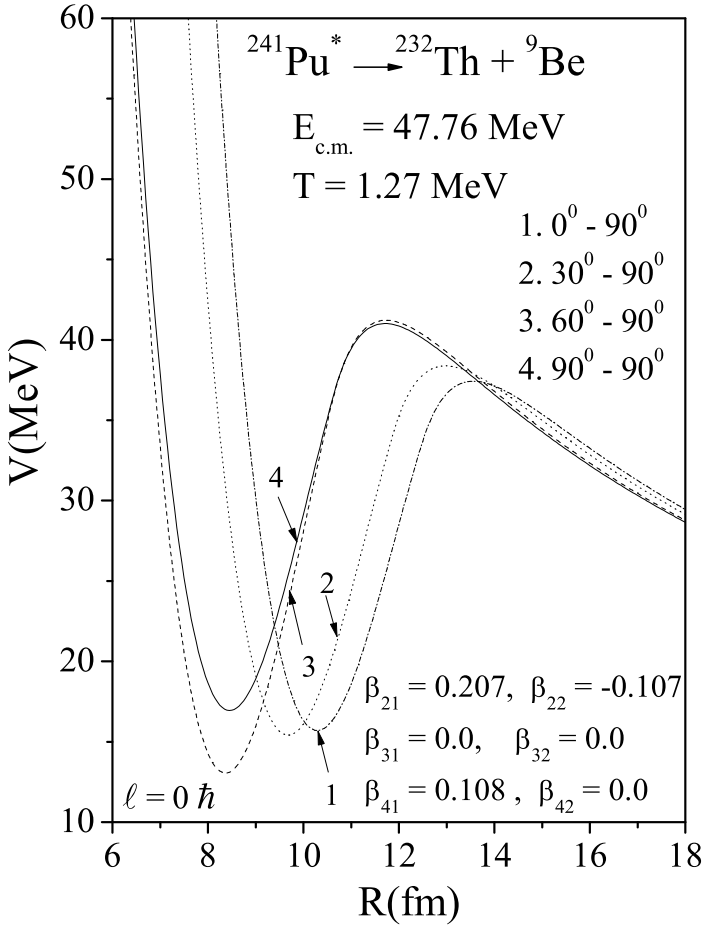

Figure 5.2 Scattering potential $V(R)$ for ^{241}Pu$^{*}\rightarrow{}^{232}$Th+^{9}Be reaction at various illustrative orientations for the case of static multipole deformations included up to hexadecapole at $\ell = 0$.

The scattering potential in Fig. 5.1, at fixed T = 1.27 MeV (equivalently, $E_{c.m.}$ = 47.76 MeV) for ℓ = 0 and ℓ_{max} cases show that the barrier position as well as barrier height get modified with the inclusion of deformation and orientation degree of freedom, thereby affecting the tunneling probability. Solid lines are with

spherical considerations, dashed and dotted lines are with static and dynamic choices of quadrupole deformation parameter β_2 alone. Note that the calculated compound nucleus decay cross-section, in DCM depends on penetrability P as given by Eq. (2.68), and hence on the deformations and orientations of nuclei. Similarly, the fact that orientation θ degree of freedom modifies the barrier strongly, is illustrated in Fig. 5.2 for the $\ell = 0$ case.

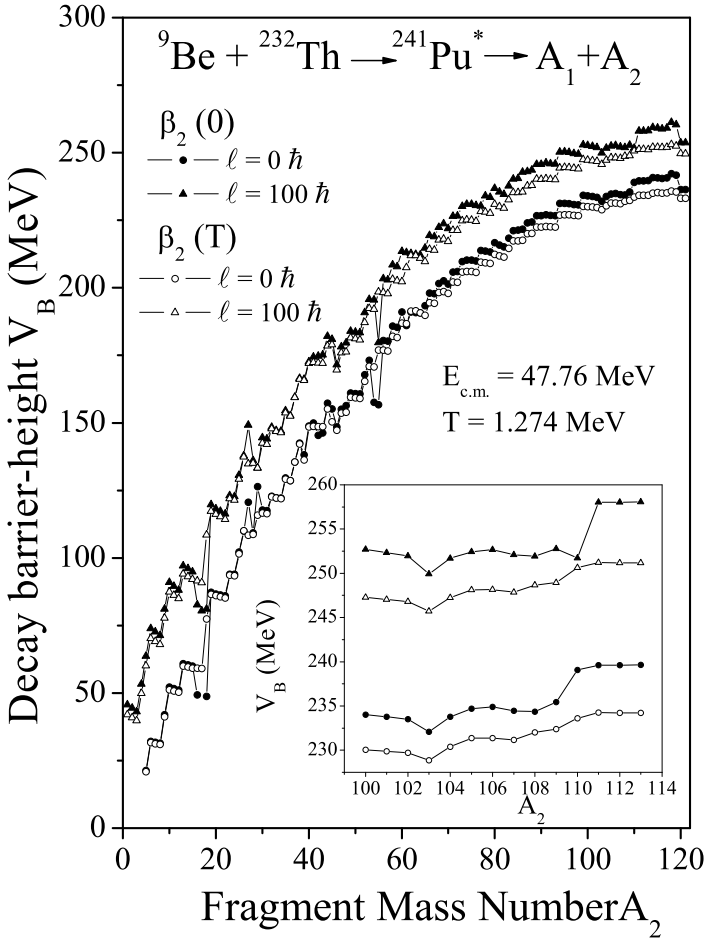

Figure 5.3 The barrier height V_B as a function of light fragment mass (A_2), for the decay of $^{241}Pu^*$ formed in $^{9}Be+^{232}Th$, calculated at two different ℓ-values for both static and dynamic choices of deformation up to quadrupole (β_2) alone.

In order to see the relative effect of static and dynamic deformations, the (decay)

barrier height V_B is plotted as a function of light fragment mass A_2 for the decay of ^{241}Pu* formed in ^{9}Be + ^{232}Th reaction at two different ℓ-values in Fig. 5.3, with deformation effects included up to β_2 alone. It is clearly evident that decay barrier height (V_B) increases as a function of fragment mass, independent of static and dynamic deformations. This behavior is similar with the one observed for the use of static deformations in the decay of heavy compound systems ^{215}Fr* and ^{204}Po* [13, 14]. The V_B distribution for the fission window with fragments A_2 = 100-113, chosen to fit the respective experimental data [10] is more pronounced at both ℓ = 0 and ℓ = 100 $\hbar$ values as shown in the inset of Fig. 5.3.

One can clearly see that V_B decreases, and hence the decay probability increases, with the inclusion of dynamical deformations in the decay of ^{241}Pu*. In other words, the decay barrier height is strongly influenced with the inclusion of static/dynamic deformations in case of heavy nuclear system having fission as prominent decay channel. Therefore a comprehensive study of static and dynamic deformations in the fragmentation process of a nuclear system may impart useful information in the context of nuclear reaction dynamics.

Fig. 5.4 shows the fragmentation potential $V(A)$, minimized in mass coordinate η_A, at the two extreme ℓ- values plotted on either side of Coulomb barrier ($E_{c.m.}$ = 37.13 MeV and $E_{c.m.}$ = 47.76 MeV), for ^{9}Be + ^{232}Th reaction. Here the cases of static and dynamic deformations are plotted for quadrupole deformation β_2 alone [panel (a) and (b)], as well as for higher multipole deformations up to hexadecapole (β_2-β_4) [panel (c) and (d)]. These calculations are made for different neck length parameters ΔR, chosen to fit the experimental data on fission cross-sections. We notice following interesting results in Fig. 5.4:

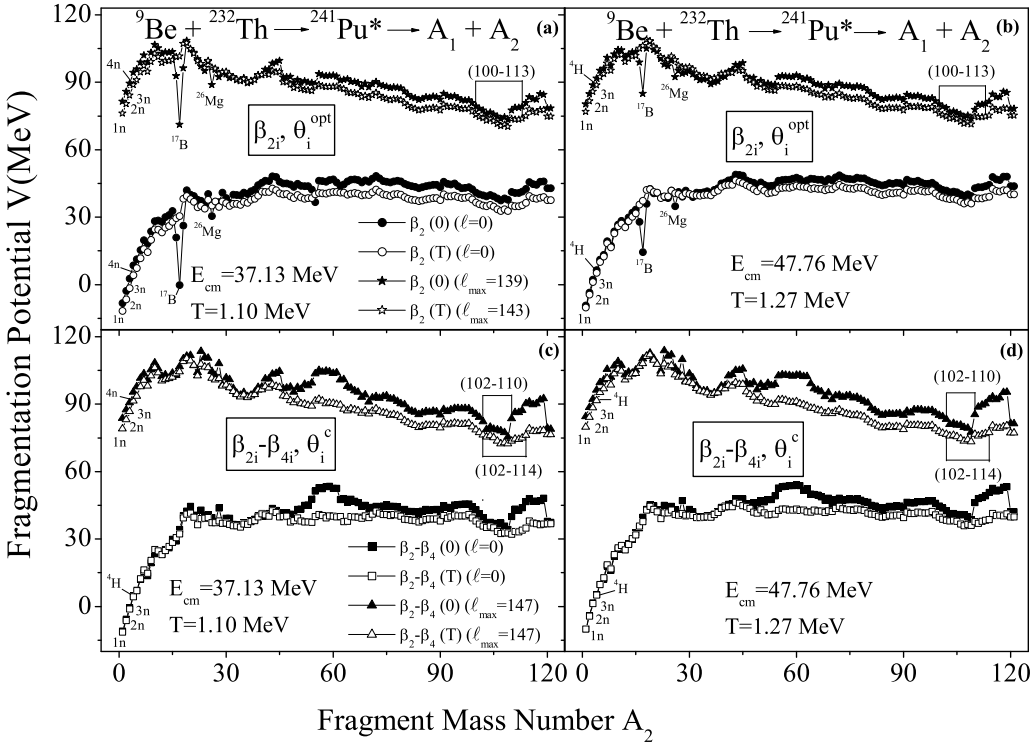

Figure 5.4 Fragmentation potentials $V(A_2)$ as a function of fragment mass number A_2 for the decay of ^{241}Pu*, plotted at extreme ℓ-values, for both static and dynamic choices of deformation up to quadrupole (β_2) alone and hexadecapole (β_2-β_4) deformed fragments.

(i) the fragmentation potentials are quite similar for both the choices of static and dynamic deformed considerations up to β_2 alone, except for the fissioning region. Also some extra valleys at ^{17}B and ^{26}Mg fragments are observed for the case of $\beta_2(0)$ (Figs. 5.4(a) and (b)), but they get ruled out in calculations due to their negligible penetrability P values.

(ii) With the inclusion of temperature dependence in higher multipole deformations (β_2-β_4) of the decaying fragments, the potential energy surface (PES) change significantly for $A_2 > 50$ and hence the relative preformation probability P_0 for all the fragments would change accordingly. However there is no noticeable change in the structure of $V(A_2)$ up to $A_2 = 50$, except in the characteristics of emitted LPs.

(iii) The contributing LP(s) change in going from $\ell = 0$ to ℓ_{max} with the inclusion of higher multipole deformations up to β_4 (Fig. 5.4(c)). However the result does not remain consistent with the increase in energy from below to above barrier.
(iv) The ER contribution ($A_2 \leq 4$) are prominent (lower in energy) at $\ell = 0$ whereas at $\ell = \ell_{max}$ the fission fragments start dominating in the decay process.
(v) The ℓ_{max} remains same over a wide range of incident energies for both the static and dynamic considerations for β_2 deformed case as well as for β_2-β_4 deformed fragments.

The above results are investigated further in terms of the preformation probability P_0 plotted as a function of fragment mass number ($A_i, i = 1, 2$) (see Fig. 5.5). One may notice from Figs. 5.4(a,b) and 5.5(a,b) that for β_2-deformed choice of nuclei, asymmetric fragmentation is preferred for both the cases of static and dynamic deformations, and the fragments in mass range A_2 = 100-113 (plus complementary heavy fragments) contribute towards fission fragments. In other words the fragmentation behavior remains asymmetric for both the cases over the range of energy under consideration. Although, one may see some contribution of symmetric fission fragments as well but its magnitude is negligibly small. With the inclusion of higher multipole deformations (β_2-β_4) of the decaying fragments, the relative preformation probability P_0 shows some variation as is evident from Fig. 5.5(c,d).

The distribution yield is asymmetric for static as well as dynamic deformed considerations just like that for β_2-deformed case. Here again some symmetric fragments are prominent for β_2-$\beta_4(0)$ case. In other words some symmetric fragments are appearing particularly for static deformed case, whose contribution seems more prominent for higher order deformations and at higher incident energies. The emer-

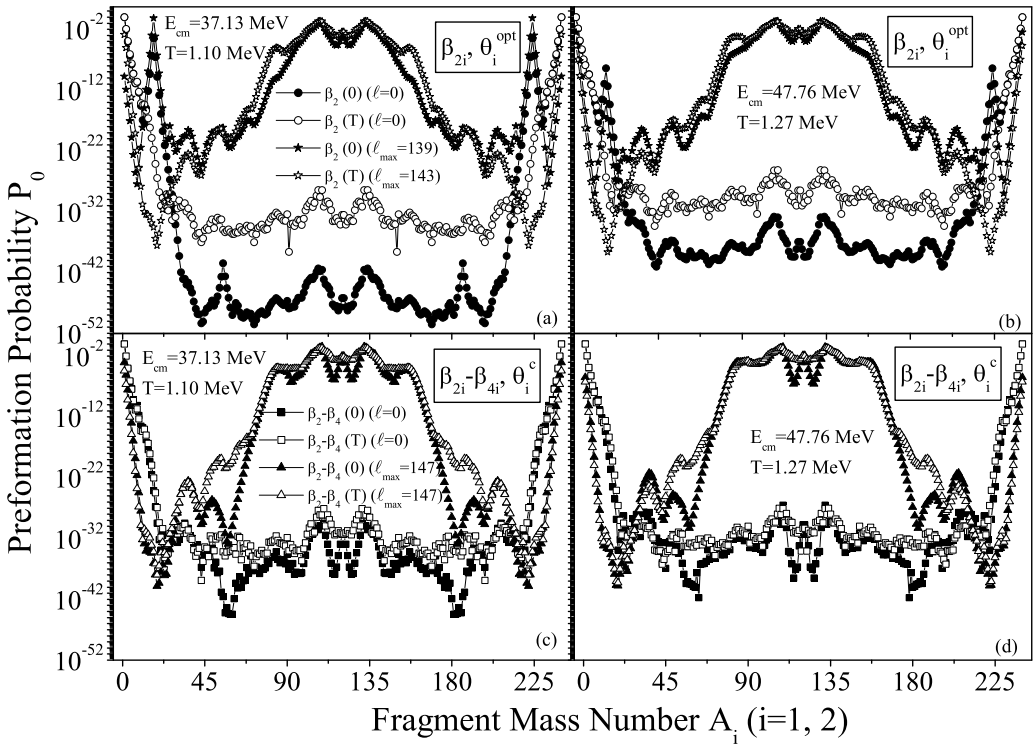

Figure 5.5 Preformation probability P_0 as a function of fragment mass number A_i, $i = 1, 2$, calculated by using the fragmentation potential of Fig. 5.4.

gence of symmetric mass distribution along with observed asymmetric fragmentation provides the possibility of the fine structure in fission of ^{241}Pu* nucleus.

For a further analysis of different fission regions, the symmetric fission (SF) peak to asymmetric fission (AF) peak ratio plotted as a function of $E_{c.m.}$ is shown for the use of static considerations in higher multipole deformations (β_2-β_4) of the decaying fragments. Here AF peak corresponds to fragment mass A_2 = 102-110 and SF corresponds to $A_2 = 120$ at all the measured energies. In order to predict the relative contribution of SF to AF peak ratio at higher energies, the ΔR values are obtained by extrapolating the fitted ΔR values for the measured fission cross-sections. It is clear from Fig. 5.6 that symmetric fission region contributes a very small though non

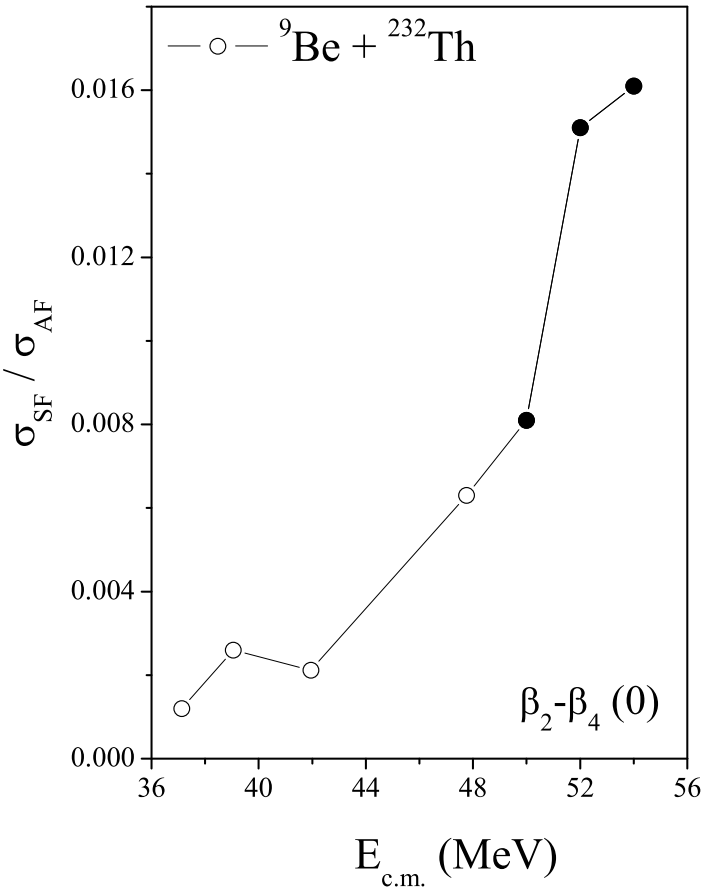

Figure 5.6 The SF-peak to AF-peak ratio plotted as a function of the incident $E_{c.m.}$ for ^{241}Pu* compound system. The filled circles show the peak ratio at extrapolated energies.

zero ($\sim$ 1.6 %) to the FF (fusion fission) cross-section at highest extrapolated centre of mass energy in comparison to $\sim$ 0.63 % at highest available $E_{c.m.}$ (= 47.76 MeV) which signifies the asymmetric fragmentation path in the decay of ^{241}Pu* nuclear system. These differences in the fission valley structure of fragmentation potentials or equivalently in preformation yields due to static or dynamical considerations in higher multipole deformations up to hexadecapole on either side of Coulomb barrier suggest the presence of fine/sub-structure of fission fragments. In other words the inclusion of static and dynamical deformations in DCM provide some new insight into the understanding of nuclear structure effects related to decay of ^{241}Pu* nucleus.

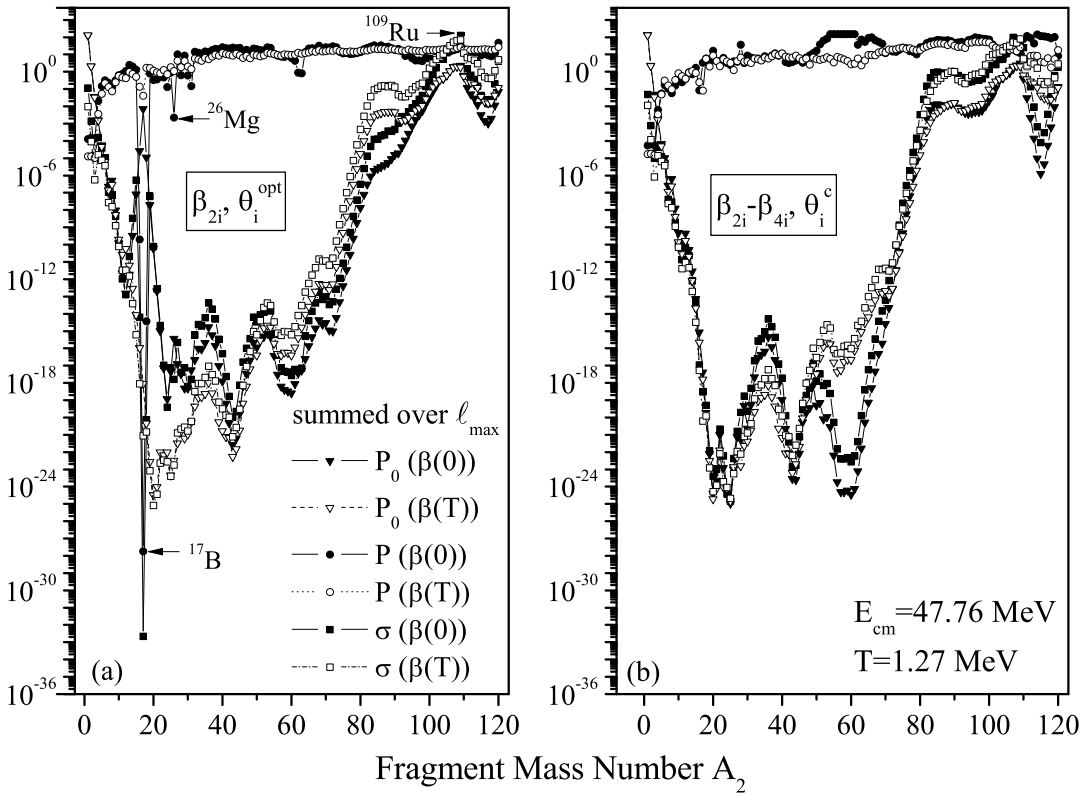

Figure 5.7 The ℓ-summed preformation probability P_0, penetration probability P and cross-section σ for the decay of ^{241}Pu* as a function of fragment mass A_2 at $E_{c.m.}$ = 47.76 MeV for both static and dynamic choices of deformation. Part (a) shows the comparison for deformed choice of nuclei up to β_2 and part (b) for deformations up to β_4.

Fig. 5.7 shows the ℓ- summed preformation probability P_0, penetrability P and cross-sections σ, with summation up to $\ell = \ell_{max}$, as a function of the light-mass fragment A_2 at highest $E_{c.m.}$ = 47.76 MeV (T =1.27 MeV). Fig. 5.7(a) show the results with static and dynamic deformed consideration up to β_2 alone and Fig. 5.7(b) shows the same with the choice of higher multipole deformations (β_2-β_4). We note that ℓ- summed P is almost constant and thus contributes mainly to the magnitude of cross-sections independent of static or dynamical deformation effects for quadrupole as well as for the hexadecapole deformed fragments. Also P tends to zero for the ^{17}B fragment (so also for ^{26}Mg) which occur as a strong minimum

in the fragmentation potential of Fig. 5.4 or as a maximum in the preformation probability of Fig. 5.5.

On the other hand σ follows the behavior of P_0 which shows an interesting structure with significant preformation factors for asymmetric mass fragments. The preformation probability P_0 and penetrability P changes with the inclusion of dynamical deformations thereby affecting the compound nucleus decay cross-sections. However the preformation probability is more sensitive and get strongly modified as compare to penetrability. It may be pointed out here that the reported fusion-fission (FF) cross-sections correspond to asymmetric fission = ($A_{CN}/2 \pm 20$) and the fragments in the mass range A_2=100-114 seem to contribute towards fission cross-sections over a wide range of incident energy, however no individual fragments are identified in the experiment [10].

The above result of a favored asymmetric fragmentation in DCM is also depicted in Fig. 5.8 where the DCM calculated cross-section for the LPs (A_2 = 1-4 summed) is compared with the most probable asymmetric fragment A_2 =109 (shown in Fig. 5.7) alone, as a function of angular momentum, up to ℓ_{max}. It is clear from figure that the contribution of light-particles cross-section σ_{LPs}, summed up to ℓ_{max} is almost zero compared to the cross-section of most probable asymmetric fragment for both the cases of static and dynamic deformed consideration up to β_2 alone. Interestingly, although the ℓ_{max} (=143 $\hbar$) obtained for the use of dynamical considerations up to β_2 is large, its cross-section for most probable asymmetric fragment (A_2 = 109) is smaller as compared to static consideration up to β_2 having lower ℓ_{max} value equal to 139 $\hbar$. This happens because the preformation probability P_0 and penetrability P for ^{109}Ru* fragment for the use of $\beta_2(0)$ is larger than $\beta_2(T)$ such that the product

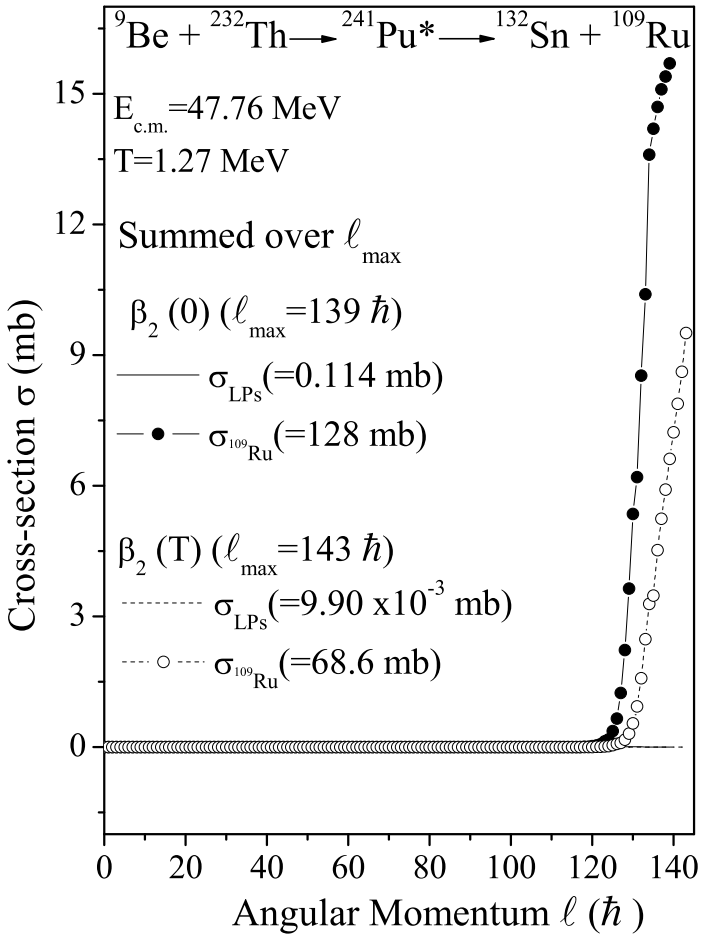

Figure 5.8 Variation of cross-section for asymmetric fission fragment of mass A_2=109 ($\sigma_{A_2=109}$), and summed up cross-section for LPs (A_2=1-4) (σ_{LPs}), as a function of angular momentum for decay of ^{241}Pu*.

P_0P is larger, and hence so is the compound nucleus decay cross-section.

Fig. 5.9 shows the fission cross-section σ_{fiss} as a function of $E_{c.m.}$ for the compound system ^{241}Pu*, calculated using DCM and compared with the experimental data along with coupled-channel code CCFUS calculations [10]. The DCM calculated σ_{fiss} fit the data very nicely at all the energies for both the cases of static and dynamic choices of deformation up to β_2 alone and β_2-β_4 deformed fragments. Such a near exact comparison between the calculations and data for both the choices of static and dynamic considerations indicate that the quasi-fission (qf) component is

either small or missing. We have also calculated σ_{LPs} contribution which is negligibly small at all energies, $\sim 10^{-1}$ to 10^{-7} mb and decreases with decreasing c.m. energy. This means that σ_{fiss} is the main contribution to the total decay cross section thereby indicating highly fissile nature of ^{241}Pu*.

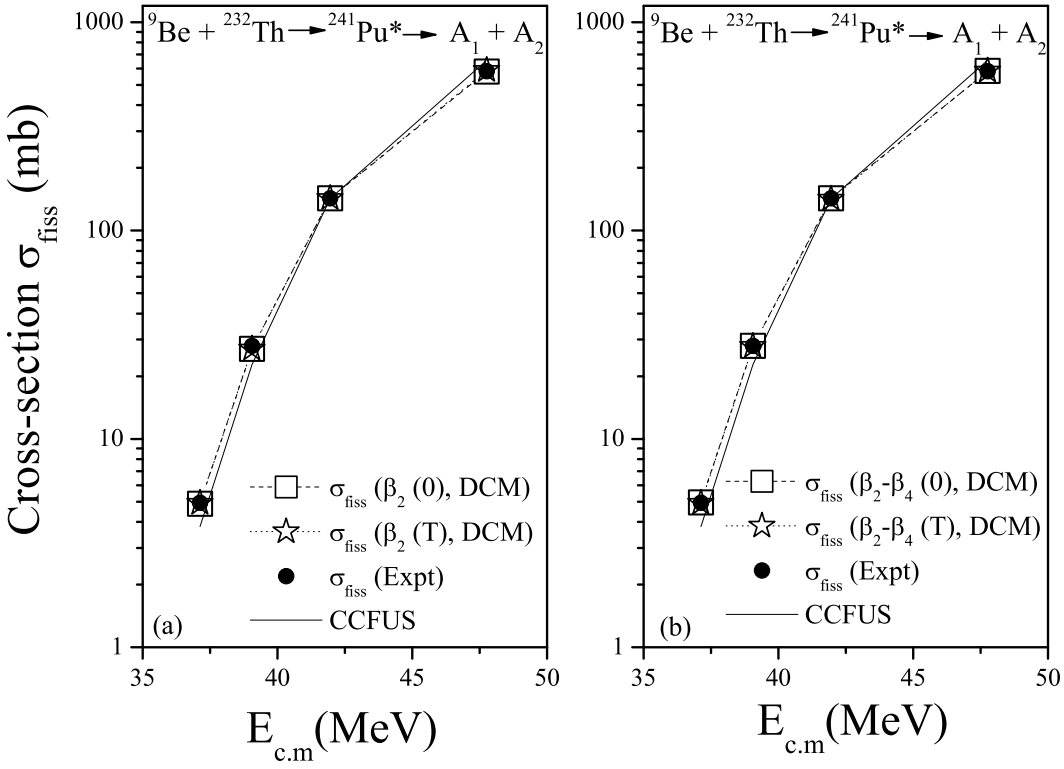

Figure 5.9 The DCM calculated σ_{fiss} for the decay of CN ^{241}Pu* formed in ^{9}Be + ^{232}Th reaction, compared with experimental data along with CCFUS predictions [10] for both static and dynamic choices of deformation up to (a) quadrupole (β_2) alone and (b) hexadecapole (β_2-β_4) deformed fragments.

The only parameter used to fit the data is the neck-length $\Delta R(T)(= R_a(T) - R_1(\alpha_1, T) - R_2(\alpha_1, T))$, as shown in Fig. 5.10. It is to be noted that the neck-length parameter ΔR, fixing the barrier-lowering parameter ΔV_B, for the best fit to fission data is found to be dependent strongly on the limiting ℓ_{max} value, which in turn depends on the use of sticking or non-sticking limit of moment of inertia

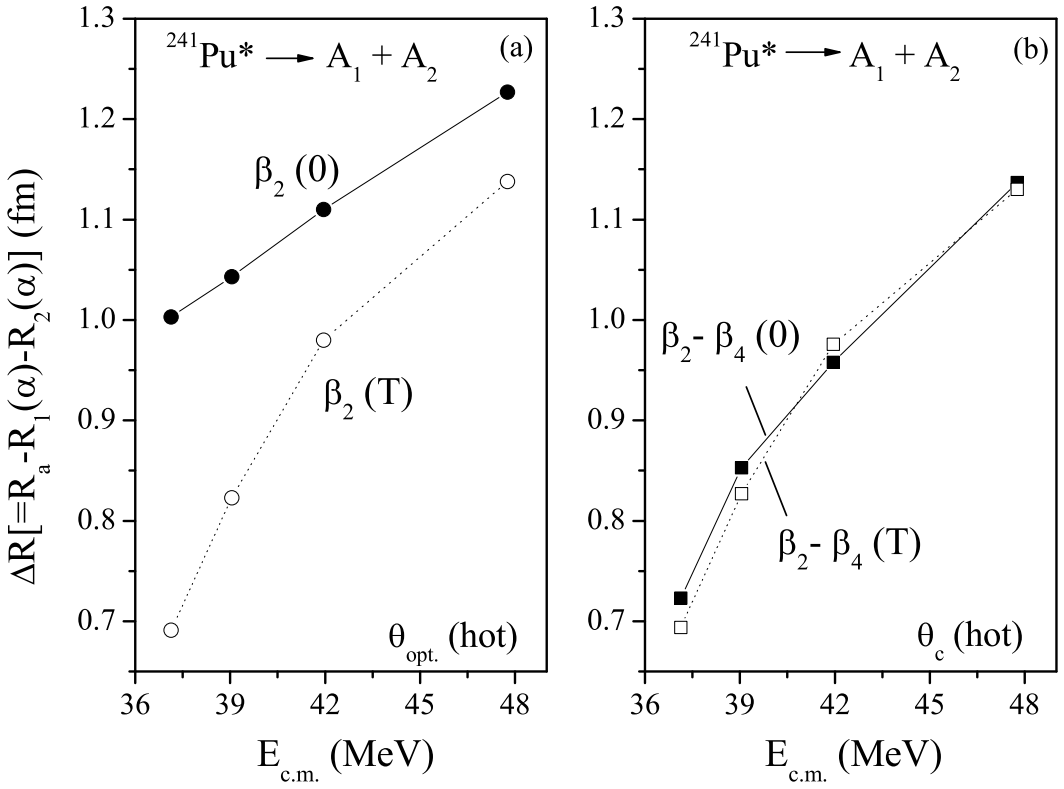

Figure 5.10 The variation of fitted parameter ΔR with $E_{c.m.}$ for fission decay of CN ^{241}Pu* formed in ^{9}Be + ^{232}Th reaction for the use of both static and dynamic consideration in (a) β_2 alone and (b) β_2-β_4 deformation parameters.

for angular momentum effects in potential. All the calculations presented above are for the sticking moment of inertia I_S which is found to be more appropriate for fitting the fission cross-sections [13]. We find that ΔR varies smoothly from above-barrier to below-barrier energies for both the cases of static and dynamic considerations. The choice of different ΔR means to indicate different reaction time scale for static and dynamical choices of deformation. The use of static and dynamic choices of deformation up to β_4 deformed fragments indicates almost same value of neck length parameter ΔR, however the same is not true for deformation effects up to β_2 alone, where ΔR for static deformations is much higher than that for dynamical deformations.

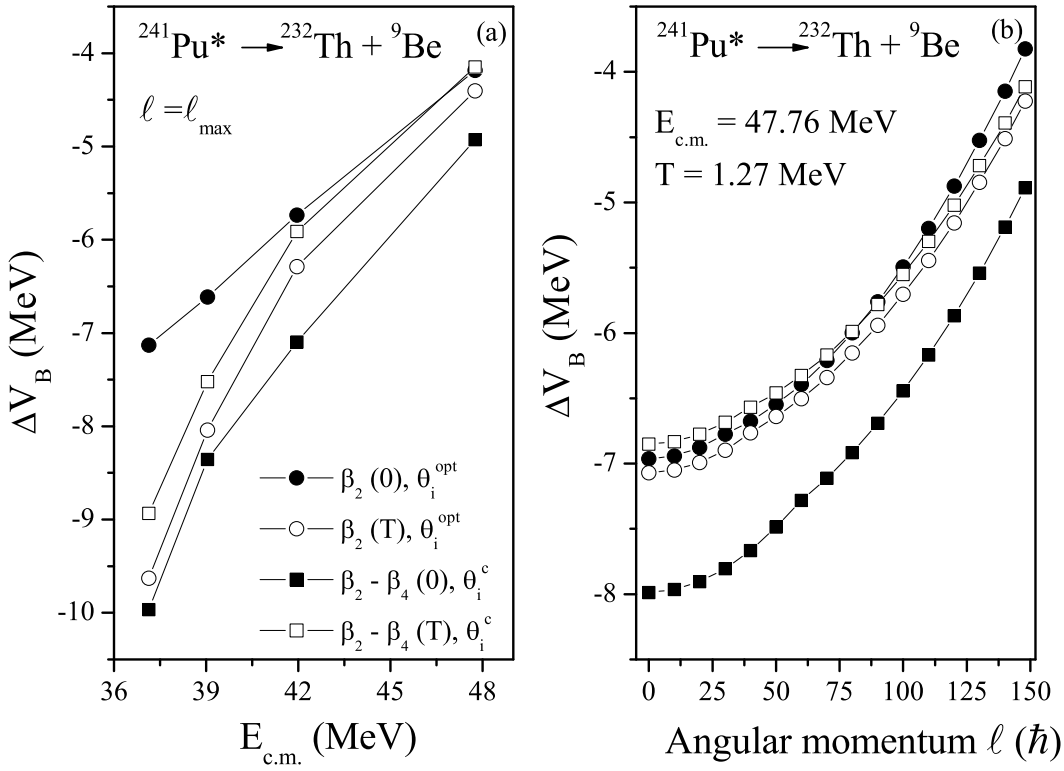

Figure 5.11 (a) Barrier-lowering parameter ΔV_B as a function of $E_{c.m.}$ for the decay of ^{241}Pu* to ^{232}Th+^{9}Be fragments, illustrated for the case of $\ell = \ell_{max}$ and (b) same as for (a) but ΔV_B as a function of ℓ at $E_{c.m.}$=47.76 MeV.

The barrier modification effect is also worked out as an in-built property of the fitting parameter, the neck-length parameter, shown in Fig. 5.11(a) as a function of $E_{c.m.}$ for the decay of ^{241}Pu* at $\ell = \ell_{max}$ and the same in Fig. 5.11(b) as a function of ℓ at highest c.m energy, $E_{c.m.}$ = 47.76 MeV. One may observe that the barrier modification is minimum for the highest energy and becomes larger and larger as the c.m. energy decreases, with maximum up to 10 MeV for the use of static consideration up to hexadecapole (β_2-β_4) deformed fragments. The maximum barrier modification for the case of dynamic consideration up to β_2 alone is ∼9.5 MeV. In general, the ΔV_B for dynamical case lies in between that for β_2 static and β_2-β_4 static. It is to be noted that the"compact" orientations change with the inclusion of

temperature dependent deformations whereas the "optimum" orientations remains intact which mean to say that "compact" orientations are sensitive to the magnitude of both the quadrupole and higher multipole deformations. The overall conclusion of above calculations is that the "barrier lowering" effect at sub-barrier energies is clearly present in DCM irrespective of static or dynamic deformation effects.

It is clearly evident from Fig. 5.11(b) that ΔV_B decreases in magnitude with the increase in angular momentum and the modification becomes small but not negligible at large value of angular momentum because with the inclusion of ℓ-dependant potential the barrier position (R_B) start shifting towards the left and thereby comes closer to R_a. Thus the present study clearly point out the importance of static and dynamical deformations (and orientations) in DCM along with the explicit role played by angular momentum ℓ in the decay of ^{241}Pu* nucleus. Since the present study is confined to a small limited energy range, so the role of dynamical deformations is less pronounced here but it could be of further interest to investigate the same over a wide range of energies spread around the Coulomb barrier, which could impart important information regarding the dynamics involved in heavy ion reactions.

Finally, the fission fragment anisotropies (A) are calculated using DCM within the SSPM approach [20] (see Eq. (2.78). Note that non-sticking moment-of-inertia I_{NS} is found to be more appropriate for the anisotropy calculations [13, 14] whereas the sticking moment-of-inertia I_S is more appropriate for obtaining the fission cross-sections which has consequences for the limiting ℓ_{max}- value to be much larger than for the non-sticking moment-of-inertia i.e. I_{NS}. For the calculation of anisotropy, same value of neck length parameter ΔR is taken, as obtained for the best fit to data

Table 5.1 The fission anisotropies calculated using DCM for ^{241}Pu* formed in the ^{9}Be + ^{232}Th reaction, at various $E_{c.m.}$'s. Calculations here refer to non-sticking limit of moment of inertia.

$E_{c.m.}$ (MeV)	ℓ_{max} ($\hbar$)	Anisotropy A DCM
37.13	12	1.237
39.05	12	1.230
41.95	15	1.340
47.76	21	1.606

on fission cross-sections using $\beta_2(0)$ deformed considerations with deformations taken from the theoretical estimates of [1] (refer Fig. 5.10). Fig. 5.12 shows the comparison of fission anisotropies calculated using DCM and the available experimental data along with the results of the SSPM and PEQ model predictions for the decay of CN ^{241}Pu* at various centre-of-mass energies spread across the Coulomb barrier.

Table 5.1 shows that anisotropies are fitted at ℓ_{max} value relatively smaller as compared to the one mentioned in Fig. 5.4 (or Fig. 5.5). This happens as a result of the use of I_{NS} approach in DCM for fitting anisotropies. It may be noted here that the choice of neck-length parameter for the above barrier predictions of SSPM anisotropy is obtained by extrapolating the values of Fig. 5.10 for static β_2-deformations. The behavior of DCM based fission-fragment anisotropies is found to be consistent with the SSPM or PEQ (see Fig. 5.12). It is clear from the Fig. 5.12 that at energies far above the barrier, the calculations are able to explain fission anisotropy data, but fail to reproduce the same at near and below barrier energies. The disagreement between the calculated and experimental anisotropies at these near and below barrier energies suggests the contribution from noncompound nucleus (nCN) fission in the reaction. The nCN fission may be attributed to quasi-fission

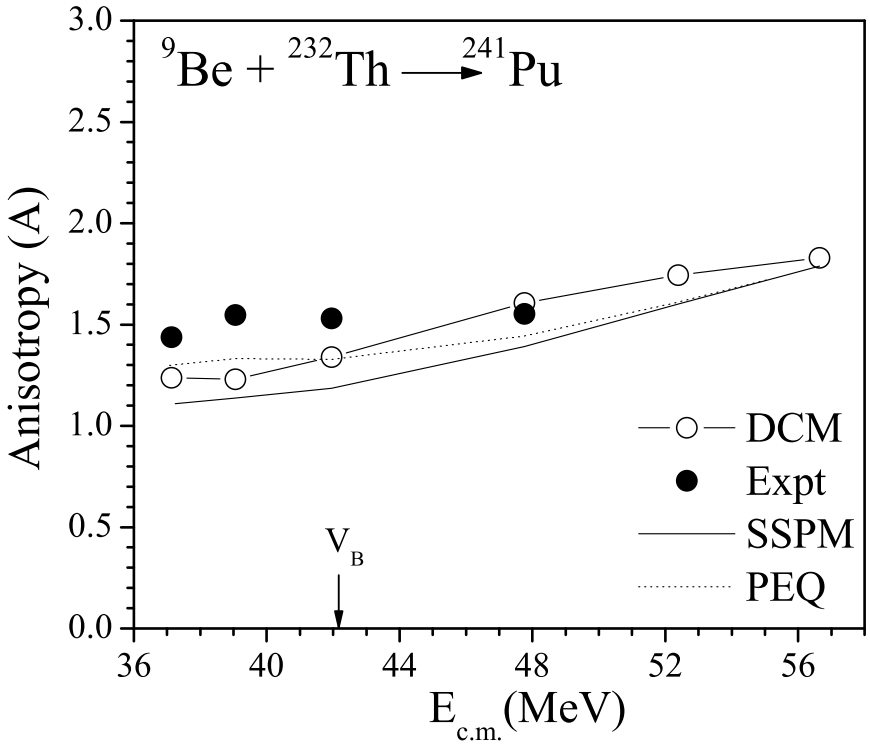

Figure 5.12 The DCM calculated fission anisotropies for CN $^{241}Pu^*$ formed in ^{9}Be + ^{232}Th reaction, using the non-sticking moment of inertia I_{NS}, at various $E_{c.m}$'s compared with experimental data along with SSPM and PEQ model predictions [10]. The arrow shows the position of Coulomb barrier.

(qf) and/or incomplete fusion (ICF) processes. The excellent agreement between DCM calculated fission cross-sections and experimental data leaves very possibility for the quasi-fission component in the decay of $^{241}Pu^*$. Hence, the deviation of theoretical estimates from anisotropy data for $^{241}Pu^*$ may be attributed to possible break up of loosely bound projectile nucleus ^{9}Be in agreement with Appannababu *et al.* [10].

Generally the fusion induced by weakly bound projectile leads to two distinct processes: CF (complete fusion) in which entire projectile fuses with target nucleus and ICF (incomplete fusion) where, only a part of projectile fuses with target nucleus. In reference to [9] the contribution of fission cross-sections comes mainly from

the CF since fission following ICF is expected to be negligible due to the lower angular momentum and excitation energy brought in by an ICF fragment. It could of further interest to investigate contribution of evaporation residues formed in ICF process due to break up of ^{9}Be nucleus into ^{8}Be + ^{1}n or into ^{5}He + ^{4}He in order to have complete understanding regarding the dynamics of fusion-fission process with stable weakly bound projectile. It may be noted that DCM calculations are sensitive towards the choice of neck length parameter "ΔR" which is taken in reference to available experimental data. In present case the data is available only for fission cross-sections and hence appropriate values of ΔR could not be estimated for ER and/or ICF paths. However if one takes same value of ΔR as reported in Fig. 5.10 for fission, then the contribution of ER or ICF remains negligibly small. In general ΔR, for ER is expected to be larger than that for fission so the possibility of ER and/or ICF component in ^{9}Be + ^{232}Th$\rightarrow A_1+A_2$ reaction is not completely ruled out. An experimental confirmation of ER and ICF data may resolve the issue.

5.3 Summary

The comparative role of static and dynamic deformations is studied in DCM in context of ^{9}Be + ^{232}Th $\rightarrow$ ^{241}Pu* reaction at both below-and above-barrier energies. The DCM gives a good description of the fusion-fission cross-sections, at various incident energies or compound nucleus excitation energies E^{*}, within a single parameter description ΔR for the use of both static and dynamic choices of deformation up to quadrupole (β_2) alone and up to hexadecapole (β_2-β_4) deformations. The preformation factor P_0 is shown to get modified with the inclusion of dynamical deformations

and hence the cross-sections change considerably. The change in penetrability P is not so strong as that for P_0. The interesting feature of this study is that fission mass distribution remains asymmetric independent of static and dynamic deformations effects studied up to quadrupole β_2 or for higher order hexadecapole deformations although a slight appearance of symmetric peak is observed for β_4 case. This appearance of symmetric peak in fission mass distributions provides the possibility of fine-or sub-structure in the fusion-fission of compound nucleus $^{241}Pu^{*}$. In order to see the possible contribution of nCN in decay of $^{241}Pu^{*}$, the calculations have also been made for the fission fragment anisotropies using SSPM approach. The anisotropy data for ^{9}Be + ^{232}Th reaction is under estimated by DCM at below barrier energies and the difference goes on decreasing with increase in excitation energy and is consistent with SSPM or PEQ at above barrier energies. The possibility of qf is ruled out and ER data is required for verification of ICF component. Thus the present study clearly points out the importance of static and dynamical deformations and related orientations in the heavy ion reaction dynamics.

Bibliography

[1] P. Möller, J. R. Nix, W. D. Myers, and W. J. Swiatecki, *At. Nucl. Data Tables* **59**, 185 (1995).

[2] M. Muenchow and W. Scheid, Phys. Lett. B **162**, 265 (1985); Nucl. Phys. A **468**, 59 (1987).

[3] M. Rashdan, A. Faessler, and W. Waida, J. Phys. G: Nucl. Part. Phys. **17**, 1401 (1991).

[4] S. Kailas, Phys. Rep. **284**, 381 (1997).

[5] S. Kailas, K. Mahata, R.G. Thomas, and S. S. Kapoor, Nucl. Phys. A **787**, 259c (2007).

[6] V. S. Ramamurthy and S. S. Kapoor, Phys. Rev. Lett **54**, 178 (1985).

[7] V. S. Ramamurthy, S. S. Kapoor, R. K. Choudhury, A. Saxena, D. M. Nadkarni, A. K. Mohanty, B. K. Nayak, S. V. Sastry, S. Kailas, A. Chatterjee, P. Singh, and A. Navin, Phys. Rev. Lett **65**, 25 (1990).

[8] D. Vorkapic and B. Ivanisevic, Phys. Rev. C **52**, 1980 (1995).

[9] M. Dasgupta, P. R. S. Gomes, D. J. Hinde, S. B. Moraes, R. M. Anjos, A. C. Berriman, R. D. Butt, N. Carlin, J. Lubian, C. R. Morton, J. O. Newton, and A. Szanto de Toledo, Phys. Rev. C **70**, 024606 (2004); *ibid* **66**, 041602(R) (2002); Phys. Rev. Lett. **82**, 1395 (1999).

[10] S. Appannababu, R. G. Thomas, L. S. Danu, P. K. Rath, Y. K. Gupta, B. V. John, B. K. Nayak, D. C. Biswas, A. Saxena, S. Mukherjee, and R. K. Choudhury, Phys. Rev. C **83**, 067601 (2011).

[11] A. Shrivastava, S. Kailas, A. Chatterjee, A. M. Samant, A. Navin, P. Singh, and B. S. Tomar Phys. Rev. Lett. **82**, 699 (1999).

[12] B. B. Singh, M. K. Sharma, R. K. Gupta, and W. Greiner, Int. J. Mod. Phys E **15**, 699 (2006).

[13] M. K. Sharma, G. Sawhney, R. K. Gupta, and W. Greiner, J. Phys. G: Nucl. Part. Phys. **38**, 105101 (2011); M. K. Sharma, G. Sawhney, S. Kanwar, and R. K. Gupta, Mod. Phys. Lett. A **25**, 2022 (2010).

[14] M. Kaur and M. K. Sharma, Phys. Rev. C **85**, 054605 (2012).

[15] M. K. Sharma, S. Kanwar, G. Sawhney, and R. K. Gupta, Phys. Rev. C **85**, 064602 (2012)

[16] R. Kumar and R. K Gupta, Phys. Rev. C **79**, 034602 (2009).

[17] R. K. Gupta, M. Balasubramaniam, R. Kumar, N. Singh, M. Manhas, and W. Greiner, J. Phys. G : Nucl. Part. Phys. **31**, 631 (2005).

[18] R. K. Gupta, M. Manhas, and W. Greiner, Phys. Rev. C **73**, 054307 (2006).

[19] A. S. Jensen and J. Damgaard, Nucl. Phys. A **203**, 578 (1973).

[20] R. Vandenbosch and J. R. Huizenga, *Nuclear Fission* (Academic: New York) (1973).

Chapter 6

Role of higher-multipole deformations in the exotic ^{14}C cluster radioactivity

6.1 Introduction

The role of higher-multipole deformations (up to hexadecapole) and orientations of nuclei is investigated, for the ground-state decays of parent nuclei, using the Preformed Cluster-decay Model (PCM). It is relevant to mention here that excited-state decay of compound systems formed in heavy ion reactions, is studied within the framework of Dynamical Cluster-decay Model (DCM) in chapters 3, 4 and 5. The work presented in this chapter is confined particularly to the spontaneous emission of ^{14}C cluster, emitted from various parent nuclei from the trans-lead region, specifically from ^{221}Fr to ^{226}Th.

With a brief general introduction on cluster radioactivity in the following, the

calculations for the ground-state decays of ^{14}C cluster from different parent nuclei using PCM, is presented in Sec. 6.2 and finally the results are summarized in Sec. 6.3.

The radioactive nuclear decay studies have contributed immensely to our understanding of nuclear phenomena and properties, in general, and nuclear structure, in particular. A charged particle, heavier than ^{4}He but lighter than a fission fragment, is spontaneously emitted in a cluster decay mode of an atomic nucleus. There is a whole family of such disintegration modes, namely, ^{12,14}C, ^{15}N, ^{18,20}O, ^{23}F, $^{22,24-26}$Ne, ^{28,30}Mg, ^{32,34}Si, ^{46}Ar, and ^{48,50}Ca from various parent nuclei, that are either observed or indicated as possible decay modes with upper limits given for their decay half-lives [1]- [3].

Cluster radioactivity is a well-established phenomenon, first on theoretical [4] and then on experimental [5] basis. Experimentally, Rose and Jones [5] first observed such a decay in 1984 for an emission of ^{14}C cluster from ^{223}Ra nucleus. This observation substantiated the theoretical predictions of cluster decays from heavier nuclei by Săndulescu *et al.* [4]. Later, many theoretical models have been advanced to describe the cluster decay modes, which can broadly be classified into two main approaches. In one such method, the cluster preformation is calculated by solving the Schrödinger equation for the dynamic flow of charges and masses; this model is called the preformed cluster model (PCM) [6]- [11]. In the second approach, known as the unified fission model (UFM) [12]- [18], cluster formation probability is calculated as an internal barrier penetration. In both the models, i.e., UFM and PCM, the cluster is supposed to penetrate the potential barrier with available Q value, which also plays a vital role in calculating the half-lives of the emitted clusters.

Thus in both types of model the preformation probability varies from cluster to cluster.

Then there are other models [19]- [21], using simple phenomenological formulas for the preformation factor, in terms of either the cluster mass A_c, the cluster-daughter charges (Z_c, Z_d), or the mass and charge asymmetries η and η_Z. Interestingly, both the PCM and UFM based models are found equally successful in reproducing the data on observed exotic cluster decays. A study [22] of near-barrier fusion excitation functions for ^{14}C and ^{18}O+^{208}Pb reactions as an inverse decay process within the UFM [23], however, indicates that the PCM type models are more suitable for lighter clusters of mass $A_c < 24$ and fission-like models seem more suitable for heavier clusters with $A_c \geq 24$. As we restrict ourselves here to the ^{14}C cluster radioactivity, the use of PCM seems further justified.

The authors of [24, 25] investigated the role of deformations and orientations in cluster radioactivity and observed that the behavior of ^{14}C radioactivity is relatively different from that of other observed cluster decays. This study indicated that the role of higher multipole deformations (β_{3i}, β_{4i}, i=1, 2) is essential for the decay of ^{14}C clusters whereas other measured cluster decays could be explained nicely with the inclusion of quadrupole deformations β_{2i} alone. It is relevant to mention here that although these studies [24, 25] were based on higher-multipole deformations up to β_{4i}, they used the so-called "optimum" orientations θ_i^{opt} of nuclei which were given only for quadrupole deformations β_{2i} [26]. For deformations higher than β_{2i}, particularly for, say, large, positive β_{4i}, i.e., $\beta_{4i} >> 0$ for prolate deformed nuclei, "compact" orientations θ_i^c must be used [27]. This is what we do in this chapter [28] for the spontaneous emission of ^{14}C clusters, observed in decays of certain parent

nuclei in the trans-lead region, specifically, from ^{221}Fr, $^{221-224,226}$Ra, ^{223,225}Ac, and ^{226}Th.

Note that ^{14}C as well as most of the daughters (^{207}Tl, ^{207,209}Pb and ^{209,211}Bi) are oblate deformed nuclei having zero or small, positive β_4 ($\sim$0.008), whose compact configurations are not yet studied. Such a study, being carried out here for the first time, shows that the contribution of compact orientations θ_i^c, with deformations up to β_{4i}, leads to an enormous improvement in fits to data on decay half-lives and α-decay branching ratios of ^{14}C cluster decays, which was not possible in calculations with θ_i^{opt} [24, 25]. We use compact "cold elongated" configurations, since cluster decay is a spontaneous decay.

A compact configuration is one occurring with the minimum interaction radius, and is "cold" or "hot" depending on if the barrier is the lowest or highest [26, 27]. In other words, "cold compact" configurations are obtained if the barrier is lowest, which occurs at a larger interaction radius, i.e., an elongated configuration, and take place for collisions in the direction of the minor axes of oblate deformed nuclei, i.e., $\theta_i^c = 90^0$, or $\sim 90^0$ if $\beta_{4i} > 0$ and $\beta_{3i} = 0$. In contrast, for a "hot compact" configuration, the barrier is highest at a smallest interaction radius.

6.2 Calculations and discussions

As per Eqs. (2.65) and (2.66), the calculated decay constant λ, or decay half-life time $T_{1/2}$, in PCM depends on both the preformation probability P_0 and barrier penetration probability P, and hence on deformations and orientations of nuclei. Since P_0 is the solution of Schrödinger equation (2.8), which requires the fragmentation poten-

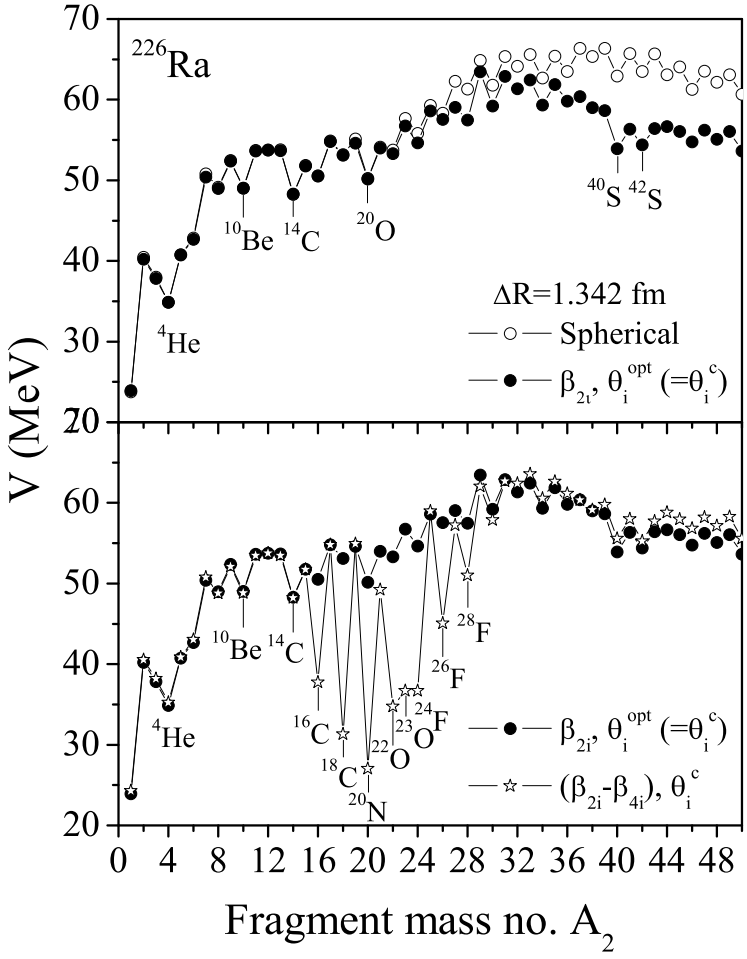

Figure 6.1 The fragmentation potentials for parent nucleus ^{226}Ra for cases of (upper) spherical and β_{2i} alone, and (lower) β_{2i} alone and (β_{2i}-β_{4i}), with appropriate cold compact orientations for all possible fragments.

tial $V(\eta)$ as an input, the role of deformations and orientations of nuclei on $V(\eta)$ is studied for the parent nucleus ^{226}Ra in Fig. 6.1, calculated for the fragments taken as spheres, with quadrupole deformations β_{2i} alone and optimum orientations θ_i^{opt} of Ref. [26] (where $\theta_i^{opt} = \theta_i^c$, the compact orientations), and with quadrupole, octupole, and hexadecapole deformations (β_{2i}, β_{3i}, β_{4i}) and θ_i^c orientations calculated by using the method of Ref. [27].

There are two important results in Fig. 6.1: (i) deep minima are observed for many clusters in the case of deformations included up to β_{4i}, in the otherwise

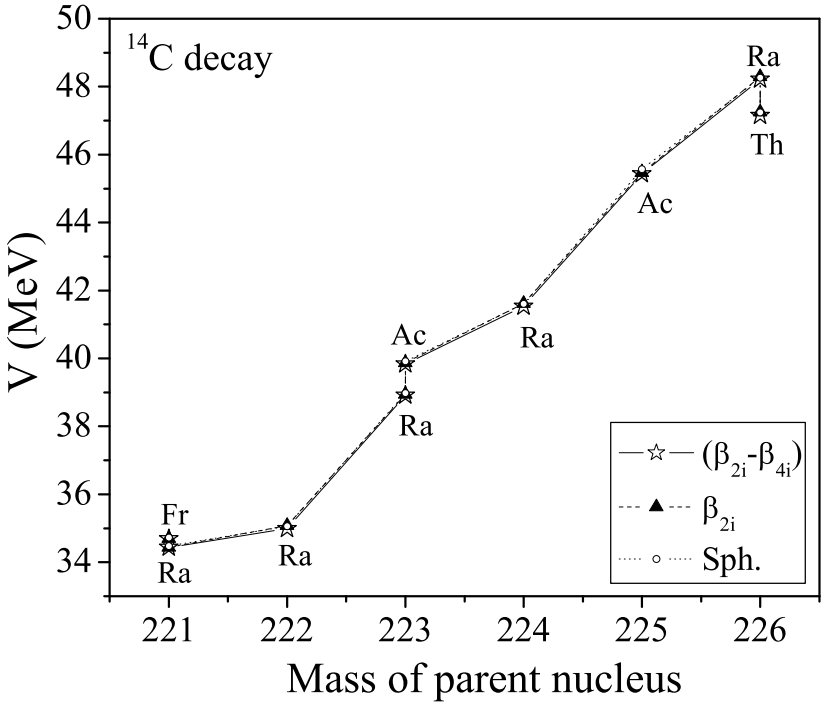

Figure 6.2 Fragmentation potential for the ^{14}C cluster emitted from various parent nuclei, calculated at the best fitted ΔR values in Table 6.1, taking the two fragments as spheres, with β_{2i} alone and (β_{2i}, β_{3i}, β_{4i}) deformations and appropriate cold compact orientations θ_i^c.

relatively smooth potential surface for the case of spherical nuclei, and minima at some selective clusters for β_{2i}-deformed nuclei; (ii) for cluster masses $A_2 \leq 15$, almost no change in the potential energy surfaces occur with deformations and orientations included. This second result is of great significance for the present study since we are concerned here with A_2=14 (^{14}C) clusters only, and it holds good for all the relevant parents, as shown in Fig. 6.2 where the fragmentation potential between ^{14}C cluster and the daughter nucleus is plotted as a function of parent nucleus mass for all the three choices of deformations (spherical, β_{2i} alone, and β_{2i}, β_{3i}, β_{4i}).

Fig. 6.2 shows that deformations and orientations of nuclei in the fragmentation potential of the ^{14}C cluster emitted from various parents play a silent role, i.e., they

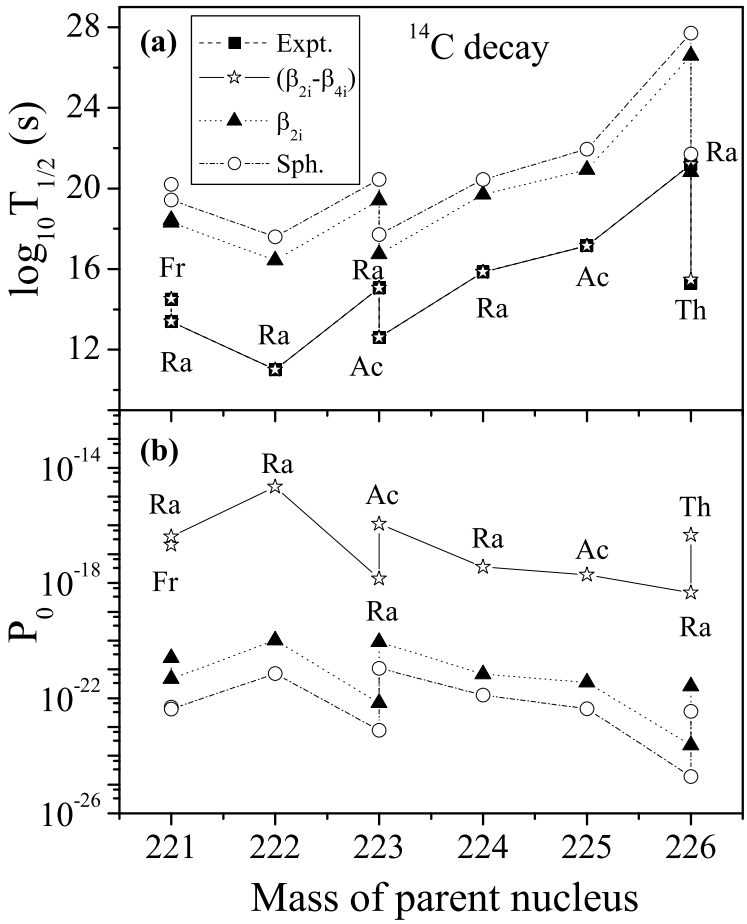

Figure 6.3 (a) PCM calculated decay half-life times for the ^{14}C cluster emitted from various parent nuclei, compared with experimental data. Calculations are for spherical nuclei, and with deformation and orientation effects included. (b) Preformation probability P_0 corresponding to the calculations in (a).

do not influence the ^{14}C minimum in $V(A_2)$. However, P_0 for the ^{14}C cluster, being the relative preformation probability, gets strongly influenced due to stronger minima in $V(A_2)$ at A_2 >15 clusters, as illustrated in Fig. 6.3 (b). One may notice that P_0 for ^{14}C clusters follows the systematic of $log_{10}T_{1/2}(s)$ for all the decaying parent nuclei. On the other hand, Fig. 6.4 shows that the PCM calculated penetrability P for the ^{14}C cluster emitted from various parents also depends very weakly (almost no dependence) on deformation and orientation effects in the scattering potential

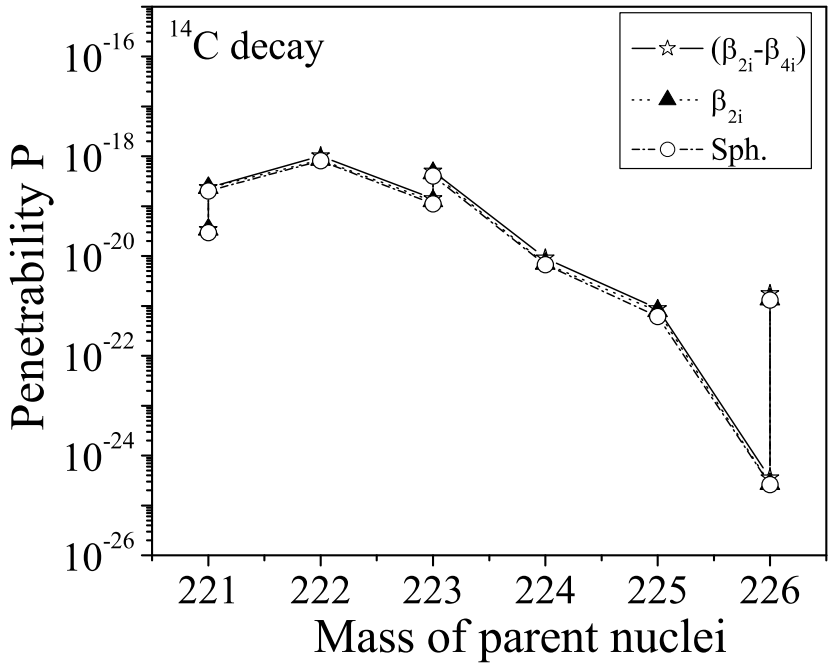

Figure 6.4 PCM calculated penetrability for the ^{14}C cluster emitted spontaneously from various parent nuclei, taking the nuclei as spherical, with deformations β_{2i} alone, and β_{2i}-β_{4i} and cold compact orientations.

V(R). In other words, the only quantity of interest for the study of cluster decay half-life times $T_{1/2}$ or decay constant λ is the relative preformation factor P_0, which gives a direct credence to the concept of preformed cluster models.

Fig. 6.3 (a) and Table 6.1 show the comparison between the calculated and experimental data for logarithm of half-life times $log_{10}T_{1/2}$ for ^{14}C cluster decay of various parent nuclei ^{221}Fr, $^{221-224,226}$Ra, ^{223,225}Ac, and ^{226}Th. Calculations are made by using the PCM of Gupta and collaborators, taking for the Q value the binding energies from Möller *et al.* [29], and for (a) spherical (b) with β_{2i} alone and (c) with (β_{2i}-β_{4i}) deformations, having appropriate cold compact orientations θ_i^c. The experimental data are from Refs [1–3, 30]. It is clearly evident that the data is best fitted for (β_{2i}, β_{3i}, β_{4i}) case, i.e., when higher-multipole deformations are included.

Table 6.1 Calculated half-life times, compared with experimental data, and other characteristic quantities for ^{14}C cluster decay of various parent nuclei to the ground states of their respective daughter nuclei. Calculations are made by using the PCM of Gupta and collaborators, for cases of spherical, β_{2i} alone and (β_{2i}-β_{4i}) deformed nuclei, with appropriate cold compact orientations θ_i^c. $Q_{M.N.}$ refers to the Q value calculated by using the binding energies of Möller *et al.* [29].

Decay	R_a	$Q_{M.N.}$	Half-lives $log_{10}T_{1/2}(s)$			
	$(=R_t+\Delta R)$	(MeV)	PCM			Expt.
	(fm)		*Sph.* (*a*)	β_{2i} (*b*)	$(\beta_{2i},\beta_{3i},\beta_{4i})$ (*c*)	
^{221}Fr$\rightarrow^{14}$C+^{207}Tl	$R_t+1.371$	31.09	20.21	18.44	14.51	14.52
^{221}Ra$\rightarrow^{14}$C+^{207}Pb	$R_t+1.410$	32.13	19.43	18.32	13.39	13.39
^{222}Ra$\rightarrow^{14}$C+^{208}Pb	$R_t+1.383$	32.47	17.60	16.43	11.01	11.01
^{223}Ra$\rightarrow^{14}$C+^{209}Pb	$R_t+1.381$	31.89	20.44	19.42	15.07	15.06
^{224}Ra$\rightarrow^{14}$C+^{210}Pb	$R_t+1.414$	31.16	20.44	19.70	15.86	15.86
^{226}Ra$\rightarrow^{14}$C+^{212}Pb	$R_t+1.342$	28.61	27.70	26.59	21.19	21.19
^{223}Ac$\rightarrow^{14}$C+^{209}Bi	$R_t+1.511$	32.89	17.71	16.75	12.61	12.60
^{225}Ac$\rightarrow^{14}$C+^{211}Bi	$R_t+1.484$	31.08	21.95	20.93	17.15	17.16
^{226}Th$\rightarrow^{14}$C+^{212}Po	$R_t+1.470$	31.70	21.71	20.82	15.46	>15.3

This happens because P_0 changes strongly with the inclusion of deformations and orientations, as is apparent from Table 6.2 where the corresponding preformation probabilities P_0 and penetrability P, are given for ^{14}C decays of the considered parents. We notice that whereas P and ν_0 are almost independent of the choice of deformation and orientation effects, P_0 is much larger for the case of deformations and orientations included. For the case of higher-multipole deformations included [the (β_{2i}, β_{3i}, β_{4i}) case, showing the best fit to $T_{1/2}$ data], P_0 for ^{14}C lies in the range of 2.21×10^{-15} to 4.55×10^{-19}, which is smaller, though, than the predicted values of many other models [11,16,19–21], including the first estimate of Rose and Jones [5] for the calculated $P_0(\alpha)$ values of, say, Refs. [31,32].

Table 6.2 PCM calculated preformation probability P_0 and penetrability P for ^{14}C cluster emitted from various parents, for cases of spherical, β_{2i} alone and (β_{2i}-β_{4i}) deformations with cold compact orientations of nuclei. The assault frequency ν_0 is nearly constant $\sim 2.9\times10^{21}$ s^{-1} for each case.

Parent	Preformation probability P_0			Penetration probability P		
	Sph.	β_{2i}	(β_{2i}-β_{4i})	*Sph.*	β_{2i}	(β_{2i}-β_{4i})
^{221}Fr	4.95×10^{-23}	2.51×10^{-21}	2.14×10^{-17}	2.95×10^{-20}	3.39×10^{-20}	3.41×10^{-20}
^{221}Ra	4.21×10^{-23}	4.72×10^{-22}	4.04×10^{-17}	2.02×10^{-19}	2.33×10^{-19}	2.34×10^{-19}
^{222}Ra	7.08×10^{-22}	1.01×10^{-20}	2.21×10^{-15}	8.21×10^{-19}	8.46×10^{-19}	1.02×10^{-18}
^{223}Ra	7.61×10^{-24}	6.92×10^{-23}	1.40×10^{-18}	1.11×10^{-19}	1.27×10^{-19}	1.40×10^{-19}
^{224}Ra	1.28×10^{-22}	6.78×10^{-22}	3.61×10^{-18}	6.75×10^{-21}	6.98×10^{-21}	9.05×10^{-21}
^{226}Ra	1.89×10^{-25}	2.33×10^{-24}	4.55×10^{-19}	2.62×10^{-25}	2.69×10^{-25}	3.53×10^{-25}
^{223}Ac	1.10×10^{-21}	8.97×10^{-21}	1.12×10^{-16}	4.02×10^{-19}	4.59×10^{-19}	5.03×10^{-19}
^{225}Ac	4.29×10^{-23}	3.54×10^{-22}	1.91×10^{-18}	6.16×10^{-22}	7.91×10^{-22}	8.78×10^{-22}
^{226}Th	3.46×10^{-23}	2.61×10^{-22}	4.58×10^{-17}	1.31×10^{-21}	1.35×10^{-21}	1.76×10^{-21}

However, P_0 in the PCM is a relative quantity, and its value depends on the choice of nuclear part of the potential in the fragmentation potential $V(\eta)$, just as the P value would depend on the chosen nuclear potential in scattering potential $V(R)$. Finally, the already observed one to one correspondence between $log_{10}T_{1/2}$ and P_0 in Fig. 6.3 justifies the fact that preformation factor P_0 imparts important nuclear structure information in cluster decay studies. Note that the only parameter of the model is the neck-length parameter ΔR, given in Table 6.1, which decides the entry point of barrier penetration as well as of cluster's preformation. The choice of a (nearly constant) positive ΔR means that the entry point is shifted toward the barrier position, in reference to the touching configuration R_t.

We have also computed the branching ratios with respect to α decay for all ^{14}C clusters, given by

$$B = \frac{\lambda_{cluster}}{\lambda_\alpha} = \frac{T^\alpha_{1/2}}{T^{cluster}_{1/2}}.$$

Table 6.3 Branching ratio for ^{14}C decay, with respect to the α particle, of various parent nuclei, calculated by the PCM of Gupta and collaborators by using the $Q_{M.N.}$ values based on binding energies from Möller *et al.* [29]. The experimental data are taken from Refs. [1–3, 30].

Decay	$\lambda_{^{14}C}$	λ_α	Branching ratio $B = \frac{\lambda_{^{14}C}}{\lambda_\alpha}$	
	(β_{2i}-β_{4i})	Expt.	PCM	Expt.
^{221}Fr$\rightarrow^{14}$C+^{207}Tl	0.212×10^{-14}	2.406×10^{-3}	8.811×10^{-13}	$(8.14\pm1.14)\times10^{-13}$
^{221}Ra$\rightarrow^{14}$C+^{207}Pb	0.280×10^{-13}	2.310×10^{-2}	1.212×10^{-12}	$(1.15\pm0.91)\times10^{-12}$
^{222}Ra$\rightarrow^{14}$C+^{208}Pb	0.672×10^{-11}	1.824×10^{-2}	3.684×10^{-10}	$(3.7\pm0.6)\times10^{-10}$
^{223}Ra$\rightarrow^{14}$C+^{209}Pb	0.577×10^{-15}	7.016×10^{-7}	8.224×10^{-10}	$(8.5\pm2.5)\times10^{-10}$
^{224}Ra$\rightarrow^{14}$C+^{210}Pb	0.950×10^{-16}	2.189×10^{-6}	4.339×10^{-11}	$(4.3\pm1.2)\times10^{-11}$
^{226}Ra$\rightarrow^{14}$C+^{212}Pb	0.446×10^{-21}	1.378×10^{-11}	3.236×10^{-11}	$(3.2\pm1.6)\times10^{-11}$
^{223}Ac$\rightarrow^{14}$C+^{209}Bi	0.168×10^{-12}	5.194×10^{-3}	3.234×10^{-11}	3.234×10^{-11}
^{225}Ac$\rightarrow^{14}$C+^{211}Bi	0.487×10^{-17}	8.022×10^{-7}	6.070×10^{-12}	$(6.0\pm1.3)\times10^{-12}$
^{226}Th$\rightarrow^{14}$C+^{212}Po	0.235×10^{-15}	3.739×10^{-4}	6.285×10^{-13}	$<9.3\times10^{-13}$

Table 6.3 shows the comparison between the experimentally observed branching ratios, taken from Refs. [1–3, 30] and the PCM calculated ones using the Q values ($Q_{M.N.}$) based on binding energies from Möller *et al.* [29]. The experimental λ_α are taken from Ref. [30], except for ^{223}Ac decay for which λ_α is taken in reference to the experimental branching ratio [2]. It is clear from Table 6.3 that PCM calculated branching ratios, using higher-multipole deformations (β_{2i}-β_{4i}), find nice comparisons with the experimentally observed branching ratio for the ^{14}C cluster radioactivity. This is further illustrated in Fig. 6.5, comparing the experimentally measured [2] and our calculated branching ratios for the ^{14}C cluster emitted from ^{223}Ac, for the three cases of nuclei taken as spheres, with β_{2i} alone, and (β_{2i}-β_{4i}) deformations. Once again, the branching ratios calculated for taking (β_{2i}-β_{4i}) deformations are in excellent agreement with the experimental branching ratios, whereas

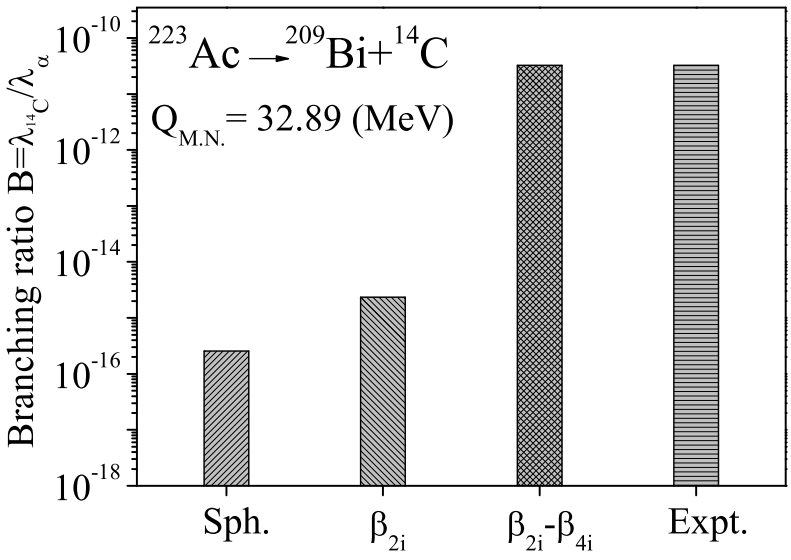

Figure 6.5 Comparison between the experimentally measured and PCM calculated branching ratios for the three different cases of deformations with appropriate cold compact orientations included, for ^{14}C cluster emitted from ^{223}Ac parent.

the same predicted for spherical or β_{2i} alone lie far below the experimental value. Thus, ^{14}C decays of both in Table 6.3 and Fig. 6.5 illustrate a clear preference for the higher-multipole deformed nuclei (up to β_{4i}) having cold compact orientations. It may be mentioned that with the presently available experimental methods, it is possible to measure the half-life time up to $\sim 10^{30}$ s and branching ratios as low as $\sim 10^{-19}$.

Finally, it is also of interest to see the role of the Q value, and angular momentum, on ^{14}C cluster radioactivity. Fig. 6.6 shows a comparative behavior of Q value vs $log_{10}T_{1/2}$ for the Pb daughter (Z_1=82) isotopes, plus the emitted ^{14}C cluster. The strong dependence of the half-life time on the Q value is evident, i.e., the Q value is a very sensitive input for the calculation of decay half-life time or decay constant. We notice that when the Q value is large, the $log_{10}T_{1/2}$ is small, and vice versa, for

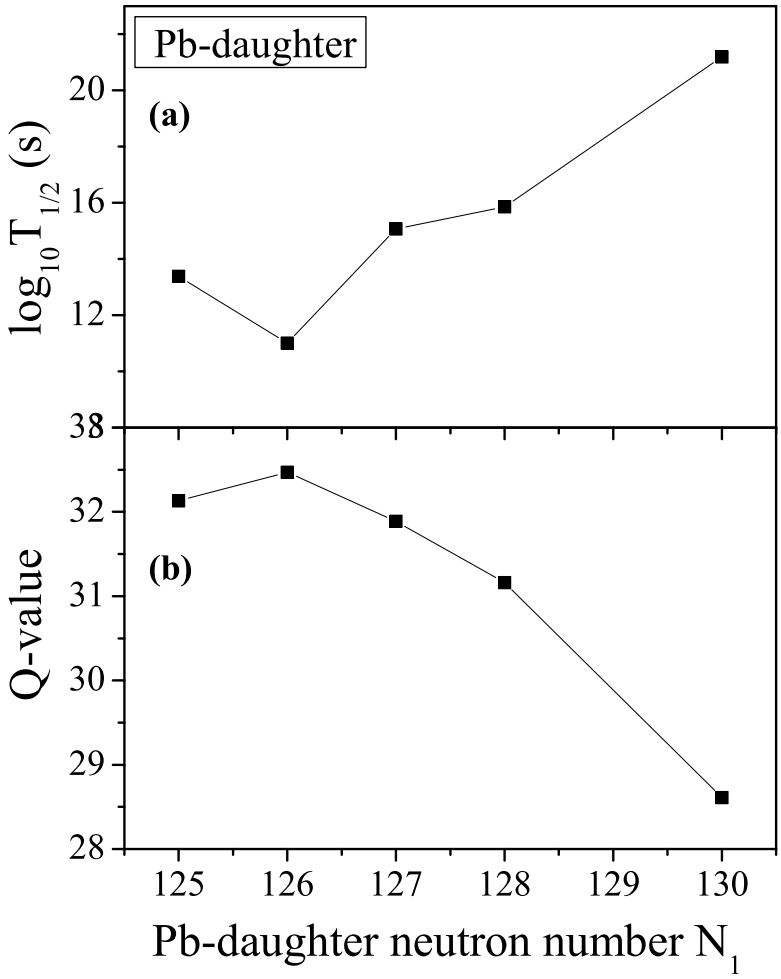

Figure 6.6 Calculated half-life times and Q values for ^{14}C cluster decay mode of Pb-daughter (Z_1=82) isotopes vs neutron number of the daughter nucleus.

all measured ^{14}C clusters emitting various isotopes of the Pb daughter.

This is further illustrated in Fig. 6.7, which shows the variation of calculated decay half-life time with Q value for the ^{14}C decay of ^{222}Ra, for cases of β_{2i} alone and with (β_{2i}-β_{4i}) deformations. The Q value ($Q_{A.W.}$) calculated from Audi and Wapstra [33] table of binding energies is also shown, which is different from that of $Q_{M.N.}$ value of Möller *et al.* [29]. Apparently, the experimental $log_{10}T_{1/2}$ values match the $Q_{M.N.}$ values for the case of (β_{2i}-β_{4i}) deformations, or at some arbitrary Q value ($Q_{arbitrary}$) for the case of β_{2i} alone. Thus, the Q value of decay plays a

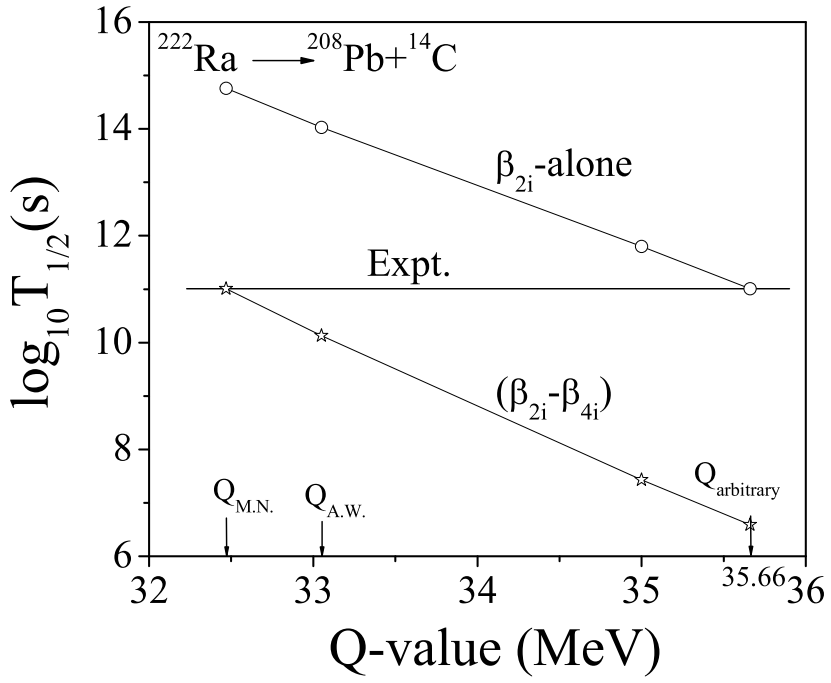

Figure 6.7 Comparison between the experimentally measured and calculated half-life times for the ^{14}C cluster emitted from ^{222}Ra as a function of the Q value. The Q values $Q_{M.N.}$, $Q_{A.W.}$, and $Q_{arbitrary}$ refer, respectively to Möller *et al.* [29], Audi and Wapstra [33], and an arbitrary value.

crucial role in deciding the clusterization process in this rare nuclear phenomena of cluster radioactivity, and should preferably be measured in the same experiment.

For angular-momentum effects, although the effect of angular momentum is expected to be insignificant for spontaneous emission of ^{14}C cluster from various radioactive parent nuclei, we study its effect in view of the fact that the (deformed) cluster and daughter are taken to be preborn in the PCM model. Fig. 6.8 gives the fragmentation potential, as a function of light fragment mass, for the decay of ^{226}Ra with angular-momentum effects added to the case of (β_{2i}-β_{4i}) deformations and cold compact orientations. One may notice that ℓ effects up to 20 $\hbar$ do not seem to influence the fragmentation potential $V(A_2)$, despite the inclusion of deformation effects in ^{14}C cluster radioactivity.

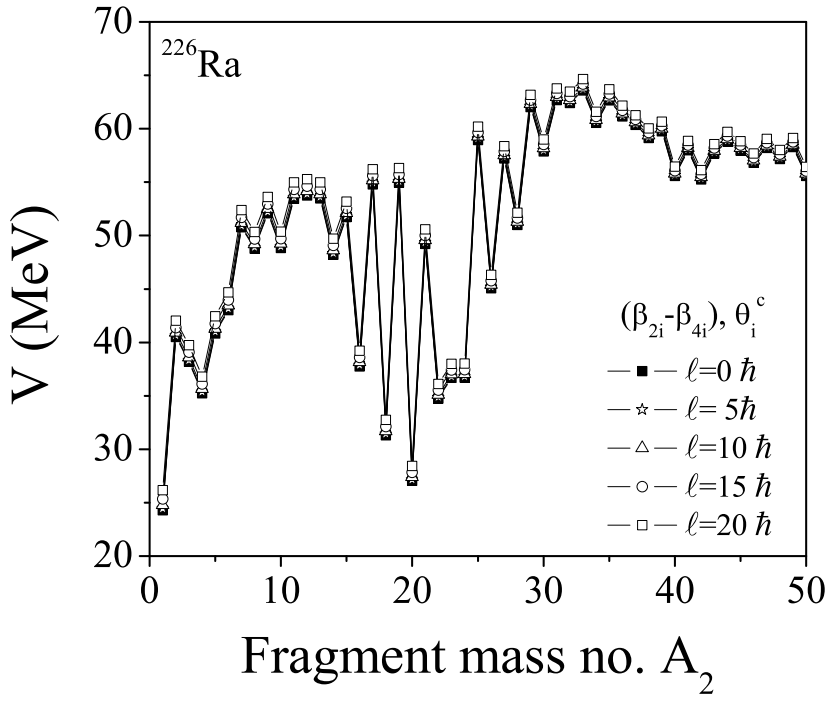

Figure 6.8 Fragmentation potential as a function of light fragment mass for the parent nucleus ^{226}Ra, calculated for different ℓ-values taking into account the (β_{2i}-β_{4i}) deformations and cold compact orientations.

6.3 Summary

The role of higher-multipole deformations (up to hexadecapole) with cold compact orientations of nuclei are included in cluster radioactivity for the first time, and it is found that both the deformations and orientations have significant effect on the calculated decay half-life times of a ^{14}C cluster emitted from various parent nuclei from the trans-lead region. This study emphasizes that whereas the assault frequency and penetrability are almost independent of the choice of deformation and orientation effects, the preformation probability is significantly influenced by the inclusion of deformations and orientations of nuclei which in turn is the only quantity that controls the decay constant and/ or half-life time. The important point to note is that: since preformation probability is a relative quantity, the shapes

(deformations and orientations) of all possible fragments of the decaying parent nucleus play their role in its determination via the relevant fragmentation potential. The experimentally measured half-life times, and branching ratios of ^{14}C clusters with respect to α decay could be obtained within the framework of the preformed cluster model of Gupta and collaborators only with the inclusion of higher-multipole deformations up to hexadecapole and cold elongated configurations of nuclei. It is also relevant to mention here that the $T_{1/2}$ values of all the measured clusters except ^{14}C could be fitted with β_2-deformation effects alone. The calculations are shown to be extremely sensitive to the Q value of decay and insensitive to the inclusion of angular-momentum effects.

Bibliography

[1] R. Bonetti and A. Guglielmetti, Rom. Rep. Phys. **59**, 301 (2007).

[2] A. Guglielmetti, D. Faccio, R. Bonetti, S. V. Shishkin, S. P. Tretyakova, S. V. Dmitriev, A. A. Ogloblin, G. A. Pik-Pichak, N. P. van der Meulen, G. F. Steyn, T. N. van der Walt, C. Vermeulen, and D. McGee, J. Phys. Conf. Ser. **111**, 012050 (2008).

[3] R. Bonetti, A. Guglielmetti, V. L. Mikheev, and S. P. Tretyakova, (private communication).

[4] A. Săndulescu, D. N. Poenaru, and W. Greiner, Sov. J. Part. Nucl. **11**, 528 (1980).

[5] H. J. Rose and G. A. Jones, Nature (London) **307**, 245 (1984).

[6] R. K. Gupta, in *Proceedings of the 5th International Conference on Nuclear Reaction Mechanisms*, Varenna, edited by E. Gadioli (Ricerca Scientifica ed Educazione Permanente, Milano, 1988), p. 416.

[7] S. S. Malik and R. K. Gupta, Phys. Rev. C **39**, 1992 (1989).

[8] S. Kumar and R. K. Gupta, Phys. Rev. C **55**, 218 (1997).

[9] R. K. Gupta, in *Heavy elements and related new phenomena*, edited by W. Greiner and R. K. Gupta (World Scientific, Singapore, 1999), Vol. II, Ch. 18, p.730.

[10] R. Blendowske, T. Fliessbach, and H. Walliser, Nucl. Phys. **A 464**, 75 (1987).

[11] S. N. Kuklin, G. G. Adamian, and N. V. Antonenko, Phys. Rev. C **71**, 014301 (2005).

[12] D. N. Poenaru, W. Greiner, K. Depta, M. Ivascu, D. Mazilu, and A. Săndulescu, At. Data Nucl. Data Tables **34**, 423 (1986); D. N. Poenaru, M. Ivascu, A. Săndulescu, and W. Greiner, Phys. Rev. C **32**, 572 (1985).

[13] Y. J. Shi and W. J. Swiatecki, Phys. Rev. Lett. **54**, 300 (1985).

[14] G. A. Pik-Pichak, Fiz. Elem. Chastits At. Yadra **44**, 1421 (1986) [Sov. J. Part. Nucl. **44**, 923 (1986)].

[15] G. Shanmugam and B. Kamalaharan, Phys. Rev. C **38**, 1377 (1988).

[16] B. Buck and A. C Merchant, J. Phys. G: Nucl. Part. Phys. **15**, 615 (1989).

[17] A. Săndulescu, R. K. Gupta, W. Greiner, F. Carstoiu, and M. Horoi, Int. J. Mod. Phys. E **1** 374 (1992).

[18] G. Royer, R. K. Gupta, and V. Yu. Denisov, Nucl. Phys. A **632**, 275 (1988).

[19] R. Blendowske and H. Walliser, Phys. Rev. Lett. **61**, 1930 (1988).

[20] Z. Ren, C. Xu, and Z. Wang, Phys. Rev. C **70**, 034304 (2004); D. Ni and Z. Ren, *ibid.* **82**, 024311 (2010).

[21] B. B. Singh, S. K. Patra, and R. K. Gupta Phys. Rev. C **82**, 014607 (2010); Int. J. Mod. Phys. E **20**, 1003 (2011).

[22] R. N. Sagaidak, S. P. Tretyakova, S. V. Khlebnikov, A. A. Ogloblin, N. Rowley, and W. H. Trzaska, Phys. Rev. C **76**, 034605 (2007).

[23] D. N. Poenaru and W. Greiner, in *Nuclear decay Modes,* edited by D. N. Poenaru (IOP Publishing, Bristol, 1996), Chap. 6, p.275.

[24] S. K. Arun, R. K. Gupta, B. B. Singh, S. Kanwar, and M. K. Sharma, Phys. Rev. C **79**, 064616 (2009).

[25] S. K. Arun, R. K. Gupta, S. Kanwar, B. B. Singh, and M. K. Sharma, Phys. Rev. C **80**, 034317 (2009).

[26] R. K. Gupta, M. Balasubramaniam, R. Kumar, N. Singh, M. Manhas, and W. Greiner, J. Phys. G: Nucl. Part. Phys. **31**, 631 (2005).

[27] R. K. Gupta, M. Manhas, and W. Greiner, Phys. Rev. C **73**, 054307 (2006).

[28] G. Sawhney, M. K. Sharma, and R. K. Gupta, Phys. Rev. C **83**, 064610 (2011).

[29] P. Möller, J. R. Nix, W. D. Myers, and W. J. Swiatecki, At. Data Nucl. Data Tables **59**, 185 (1995).

[30] R. K. Gupta and W. Greiner, Int. J. Mod. Phys. E **3**, 335 (1994).

[31] D. S. Delion, A. Săndulescu, and W. Greiner, Phys. Rev. C **69**, 044318 (2004).

[32] K. Varga, R. G. Lovas, and R. J. Liotta, Phys. Rev. Lett. **69**, 37 (1992).

[33] G. Audi and A. H. Wapstra, Nucl. Phys. A **595**, 409 (1995).

Chapter 7

Summary and outlook

In this thesis the possible decay modes of a variety of nuclear systems are investigated using the collective clusterization method. The preformed cluster-decay model (PCM) is used for ground-state decay of a nuclei to explore the phenomena of exotic cluster radioactivity and the dynamical cluster-decay model (DCM), which is an extension of PCM, have been used to understand the decay paths of excited compound systems formed in heavy-ion reactions. Various nuclear phenomenon such as static and dynamic deformations and orientations, barrier modification, structure/substructure of fission fragments, shell effects, angular momentum, entrance channel, and fission anisotropies etc are investigated in the present work.

Both PCM and DCM are based on Quantum Mechanical Fragmentation Theory (QMFT) and consider all decay products as dynamical mass motion of preformed fragments or clusters through the interaction barrier, thereby including the structure effects of nuclei and/or compound nuclei explicitly. The DCM calls for the introduction of temperature-dependent binding energies, and the deformations and orientations degrees of freedom, together with the use of "optimum" or "compact"

orientations, for incoming nuclei as well as outgoing nuclei/fragments. The deformation and orientation effects of both the parent nucleus and decay products (daughter and cluster nuclei) are found important in the PCM for ground-state, spontaneous decays.

An overview of current status of research, pertaining to the process of cluster radioactivity and heavy ion reaction dynamics, have been discussed in Chapter 1. The details of PCM and DCM are discussed in Chapter 2. The formation and decay of an equilibrated compound nucleus has been a topic of great interest and is supposed to impart important information in context of reaction mechanism at low energies. The CN can decay in number of ways by emitting multiple light particles (n, p, α) and γ-rays (constituting the evaporation residue, ER), fusion-fission (ff, consisting of intermediate and heavy mass fragments, and the asymmetric or near-symmetric, and symmetric fission fragments), and many a times a noncompound, quasi-fission (qf), or ICF process. In general, a heavy nuclear system ($A_{CN} \sim 200$) formed in low energy heavy ion reactions, decays by fission with small contribution from neutrons and γ-rays emissions, in contrast to the decay process of light compound systems. However ER contribution for some heavy nuclear systems is found to be quite significant. This interplay between ER and fission cross-sections impart interesting information in context of formation and decay properties of heavy nuclear system. In present work, the reaction dynamics of heavy compound systems formed in a variety of heavy ion reactions is investigated in the framework of DCM. Beside this, the role of higher multipole deformations is explored in context of cluster radioactivity using PCM.

As a first application, the DCM is used to study the odd-mass nuclear systems

^{213,215,217}Fr* over a wide center-of-mass energy range of 47 to 94 MeV in Chapter 3. The decay of ^{215}Fr* nucleus, is studied using DCM, formed via two different asymmetric reaction channels ^{11}B+^{204}Pb and ^{18}O+^{197}Au, having mass-asymmetry α's placed on either side of the α_{BG}. In order to investigate the entrance channel effects, we compare the results of calculations for the two reaction channels, made at about the same compound nucleus excitation energy E^{*}_{CN} ∼43.5 MeV. Interestingly, the ℓ_{max} value is found to be the same for the two reaction channels, chosen across the α_{BG} limit. In addition to ℓ-independence, the decay barrier-heights also show entrance channel independence.

For both the channels, the DCM-calculated fission-fragment anisotropies and fusion excitation functions are compared nicely with the experimental data, supporting the entrance channel independence in the decay of ^{215}Fr* in agreement with experimental observations and statistical model (PACE2) calculations. The role of sticking versus non-sticking moment-of-inertia is discussed which allows us to conclude that non-sticking limit is more appropriate for anisotropy calculations, whereas sticking limit is best suited for obtaining fusion (consisting mainly of fusion-fission) excitation functions which involves a larger limiting value ℓ_{max} and hence a smaller neck-length parameter ΔR required for the proximity potential ($\leq$ 2fm.)

For the decay paths of compound systems ^{213,217}Fr*, formed in ^{19}F+^{194,198}Pt reactions, the anomalous fission anisotropies measured for ^{213}Fr* (with neutron number $N = 126$) system which are normal for ^{217}Fr* ($N = 130$), is believed to be associated with either the neutron magic shell of the compound nucleus or a presence of a non-compound nucleus (nCN) component, like the quasi-fission, in fission cross-section. The DCM calculated σ_{fiss} (as well as the σ_{ER}) match the data nearly exactly, with

qf contribution of atmost 4-10% of σ_{fiss} (for the lowest to highest energy) for ^{213}Fr* and 8-10% for ^{217}Fr*. For both the quadrupole deformation (β_2) alone and higher multipole (β_2-β_4) deformed choices of fragmentation, a small hump (a shoulder) is seen for the two systems in their respective preformation yields due to the deformed magic shell around $Z_2 = 36$ and spherical magic shell around $Z_1 = 50$, which is somewhat stronger for ^{213}Fr* ($N = 126$) decay than in the case of ^{217}Fr* ($N = 130$). The same magic shell closure effects are prevalent in ^{215}Fr* compound system which, for this system, need further investigations. Another important result for all the three ^{213,215,217}Fr* systems is that, with the inclusion of deformation and orientation effects of nuclei, the mass fragmentation changes from symmetric to asymmetric, with the above noted humped structure suggesting the presence of structure effects in the fission products of the three ^{213,215,217}Fr* nuclei.

Though DCM has been applied to investigate decay path via CN channel, its application in reference to incomplete fusion (ICF) and subsequent decay processes along with complete fusion (CF) process is studied in reference to the dynamics of ^{10,11}B + ^{209}Bi reaction forming compound systems ^{219,220}Ra* in Chapter 4. Within DCM, the excitation functions for both the evaporation residue and fission are found to be in good agreement with the reported experimental data within one parameter fit of the model. The choice of different neck-length parameter (ΔR) values for ER and fission indicate that the two decay processes occur in different time scales and evolve subject to the nature of dynamics of compound nucleus formed. It is observed that ER is a prompt process since ΔR for this process is large than that for fission, for both the systems, more so for the heavier isotope ^{220}Ra. However the fission takes place almost at same time scale for ^{219}Ra and ^{220}Ra.

Also, the complete fusion (CF) excitation function for ^{219}Ra system, at various incident energies, are obtained by summing the fission, neutron evaporation ($1n$-$4n$) and charged-particle evaporation residue cross-sections produced through the through the αxn and pxn ($x = 2, 3, 4$) emission channels. Interestingly the main contribution to complete fusion cross-section comes from the fission cross-section at higher incident energies, which in DCM is found to consist of an asymmetric fission window, shown to arise due to deformation and orientation effects of formation and decay fragments. For the LPs emission, $1n$ emission is shown to contribute the largest, which does not seem to be operating in the (statistical model) analysis of experimental data. Experimentally the CF suppression is suggested in these reactions which is attributed to the low binding energy of ^{10,11}B, causing its breakup into charged fragments (e.g. ^{10}B may break up into ^{6}Li and an α-particle, ^{8}Be and ^{2}H, ^{9}Be and proton). This is supported by the significant incomplete fusion cross-sections observed for both the reactions. So an attempt has been made to study incomplete fusion (ICF) processes using DCM . Interestingly, the DCM calculated CF and ICF cross-sections for ^{219}Ra system compare nicely with experimental data at all the reported energies, which allow us to conclude that DCM can also be applied for ICF process along with its well established application in CF process.

It is important to note that so far only the static deformations of Möller and Nix are used in the framework of DCM to understand the heavy ion reactions. In order to investigate the role of dynamic deformations, the decay of hot and rotating compound system ^{241}Pu*, at both below-and above-barrier energies, is studied in Chapter 5 using DCM which is extended to include the temperature dependent (dynamic) deformations effects of nuclei. The projectile, target, and the compound

nucleus formed are all strongly deformed so the role of deformation and orientation effects is expected to be important in the context of present study. These calculations have been done using quadrupole (β_2) deformations having "optimum" orientations and the higher multipole deformations (β_2-β_4) having "compact" orientations of hot configurations for decaying products.

The compound nucleus, ^{241}Pu*, formed in the reaction ^{9}Be + ^{232}Th is highly fissile and decays totally via fission, therefore σ_{fiss} is the major contributer to the total decay cross-section. It is observed that with the inclusion of temperature dependent (dynamic) deformations of the decaying fragments, potential energy surface (PES) change quite significantly and as a result the relative preformation probabilities P_0 for all the fragments gets modified accordingly. Also the scattering potential (corresponding barrier position, height and frequency) is modified with the inclusion of temperature dependent deformations of outgoing fragments, thereby affecting the tunneling probability P through barrier. For β_2-deformed choice of nuclei, fission mass distribution remains asymmetric for both the cases of static and dynamic deformations, over a range of energies under consideration. However with the the inclusion of higher multipole deformations (β_2-β_4) of the decaying fragments, some symmetric fragments start appearing along with the asymmetric fragmentation, whose contribution seems more prominent for static deformed case and at higher incident energies. This emergence of symmetric mass distribution provides the possibility of fine structure in fission of ^{241}Pu* nucleus. Also, for the best fit to data on fission cross-sections, an in-built "barrier lowering" seems operative at sub-barrier energies, irrespective of static or dynamic deformation effects. The present study points out the importance of static and dynamical deformations (and orientations) in DCM and

more systematic studies regarding the dependence of deformation on temperature in different regions of fissility could be useful for overall understanding of nuclear reaction dynamics.

Besides heavy ion reactions, the role of higher-multipole deformations and orientations of nuclei is investigated in reference to ground state decays of heavier nuclei in Chapter 6. These effects are duly incorporated in PCM for investigating spontaneous emission of ^{14}C clusters, observed in decays of certain parent nuclei in the trans-lead region, specifically, from ^{221}Fr to ^{226}Th. We notice that whereas penetrability and assault frequency are almost independent of the choice of deformation and orientation effects, the preformation probability changes strongly and become much larger for the case of deformations and orientations included, as compared to spherical nuclei. It is important to note that preformation probability in the PCM, is a relative quantity and its value depends on the type of interaction potential used in the fragmentation potential. The calculated decay half-lives and branching ratios of ^{14}C clusters with respect to α-decay, are in good agreement with measured values for the calculation performed with higher-multipole deformations (β_2, β_3, β_4), with "compact" orientations of cold elongated configurations. It is relevant to mention here that the $T_{1/2}$ values of all the measured clusters except ^{14}C could be fitted with β_2-deformations effects alone. Also, the Q value is shown to be very sensitive input for predicting the half-lives of the clusters.

The above mentioned work has the potential of getting extended to other mass regions for having a good understanding of nuclear structure in general and nuclear dynamics in particular. It may be noticed that all the calculations done in the present work are for use of the nuclear proximity potential, with deformation effects

included up to hexadecapole, and orientations θ_i (i =1, 2) of two nuclei taken in the same plane (co-planar nuclei, with azimuthal angle ϕ =0^0). However it would be interesting to further extend this study to non-coplanar ($\phi \neq 0^0$) configurations. The use of different versions of proximity interactions in context of heavy ion reaction dynamics could also impart useful information. Beside this various compound and noncompound nuclear mechanisms, particularly the ones associated with radioactive beams can be explored further.